

Measuring and managing phenotypic heterogeneity and plasticity in breast cancer to  
improve therapeutic control

By

Tyler Risom

A DISSERTATION

Presented to the Cancer Biology graduate program  
and the Oregon Health & Science University  
School of Medicine

in partial fulfillment of  
the requirements for the degree of

Doctor of Philosophy

July 2017

School of Medicine  
Oregon Health & Science University

---

CERTIFICATE OF APPROVAL

---

This is to certify that the PhD dissertation of

Tyler Thomas Risom

has been approved

---

Rosalie Sears (Mentor/Advisor)

---

Soren Impey (Committee Chair)

---

Joe Gray (Committee Member)

---

Owen McCarty (Committee Member)

---

David Qian (Oral Exam Member)

# Table of Contents

1	Introduction.....	15
1.1	Intertumoral heterogeneity in breast cancer .....	19
1.1.1	Breast cancer subtypes .....	19
1.1.2	Subtype targeted therapy .....	22
1.1.3	Targeted therapies on the horizon for triple negative breast cancer .....	25
1.2	Intratumoral heterogeneity in breast cancer .....	26
1.2.1	Clonal heterogeneity .....	26
1.2.2	Cell state heterogeneity .....	27
1.2.3	Darwinian selection.....	30
1.3	Cell state plasticity in breast cancer .....	32
1.3.1	Cell state plasticity in normal breast development and tissue maintenance .....	32
1.3.2	The regulation of chromatin, transcription factors, and cell state .....	34
1.3.3	The influence of therapy on tumor cell state .....	36
1.3.4	Therapeutic strategies to combat plasticity .....	39
1.4	Summary .....	41
2	Measuring cell state heterogeneity in breast cancer .....	43
2.1	Abstract .....	44

2.2	Introduction .....	45
2.3	Results.....	47
2.3.1	Differentiation-state heterogeneity in primary breast cancers and patient derived cell lines.....	47
2.3.2	Differentiation-state heterogeneity in breast cancer cell lines.....	51
2.3.3	Assessing differentiation-state heterogeneity through gene expression.....	53
2.4	Discussion.....	56
3	Managing drug-induced differentiation-state plasticity in basal-like breast cancer to improve therapeutic control .....	59
3.1	Abstract .....	60
3.2	Introduction .....	61
3.3	Results.....	63
3.3.1	Targeted therapies generate distinct drug-tolerant persister states.....	63
3.3.2	Cell state dynamics during therapy .....	71
3.3.3	Drug combinations reduce therapeutic escape.....	78
3.3.4	Inhibiting differentiation-state transitions with BET inhibition .....	84
3.3.5	JQ1 prevents chromatin accessibility changes associate with DTP generation ..	88
3.4	Discussion.....	96

3.5	Miscellaneous .....	100
4	Targeting Heterogeneous and Plastic Triple Negative Breast Cancers with Small Molecule Activators of PP2A .....	102
4.1	Abstract .....	103
4.2	Introduction .....	104
4.3	Results.....	109
4.3.1	Activators of PP2A effectively inhibit proliferation and induce cytotoxicity in triple negative cell lines .....	109
4.3.2	SMAPs effectively kill all differentiation states in heterogeneous TN cell lines and tumor models.....	111
4.3.3	PP2A activators and kinase inhibitors act synergistically to inhibit TN cell proliferation .....	115
4.4	Discussion.....	117
5	Materials and Methods .....	120
5.1	Cell Lines .....	120
5.2	Reagents.....	120
5.3	Image cytometry and heterogeneity metrics.....	121
5.3.1	Image cytometry of primary patient tumors .....	121

5.3.2	Image cytometry of patient derived xenograft tumors .....	123
5.3.3	Image cytometry of cancer cell lines.....	125
5.3.4	Calculating heterogeneity .....	126
5.4	Gene expression analyses.....	127
5.4.1	Cell line expression analysis.....	127
5.4.2	RNA-sequencing .....	127
5.4.3	Geneset enrichment analysis .....	129
5.5	Measuring drug efficacy .....	130
5.5.1	Therapeutic screening and synergy analysis .....	130
5.5.2	Cell death assays.....	131
5.5.3	Cell cycle analysis .....	132
5.6	Computational modeling.....	132
5.7	VIPER analysis .....	134
5.8	Single cell ATAC-seq library construction and analysis.....	136
5.9	Animal studies.....	137
5.9.1	Assessing JQ1 + BEZ235.....	137
5.9.2	SMAP studies in Lsl-Myc:PTEN <sup>fl/fl</sup> :Blg-Cre mice .....	138
5.9.3	Tumor-derived cell line establishment .....	139

5.10	Statistical analysis .....	140
6	Conclusions and Future Directions .....	141
6.1	Improving clinical assessment of intratumoral heterogeneity .....	141
6.2	Rethinking current treatment paradigms for heterogeneous tumors: moving towards “management”, not cures.....	143
6.3	New approaches to treat heterogeneous and plastic breast tumors .....	145
6.3.1	Advancing Kinase Inhibitor and BET inhibitor combination therapy.....	147
6.3.2	Advancing Small molecule activators of PP2A .....	151
7	References.....	153
8	Appendix - Extended description of computational modeling .....	181

## List of Figures

Figure 1-1 Breast cancer subtypes.....	21
Figure 1-2 Axes of differentiation in breast cancer.....	29
Figure 1-3: Branched evolution and clonal selection in TN tumors. ....	31
Figure 1-4: PP2A targets and activating agents. ....	41
Figure 2-1: Differentiation-state heterogeneity is enriched in triple negative and basal-like subtype tumors. ....	50
Figure 2-2: Breast cancer cell lines model the differentiation state heterogeneity observed in their tumor subtype of origin. ....	52
Figure 2-3: Heterogeneity in luminal, basal, and mesenchymal geneset expression correlates with image based cell-state heterogeneity metrics. ....	55
Figure 3-1: Targeted therapies enrich distinct drug-persisting differentiation states.....	65
Figure 3-2: MEK and PI3K/mTOR inhibitors have opposing influence on basal differentiation in drug-persisting cells.....	68
Figure 3-3: MEK and PI3K/mTOR enrich distinct DTP differentiation-states in basal-like cell lines .....	71
Figure 3-4: Cell state transitions underlie DTP-state enrichment.....	74
Figure 3-5: Further examination of DTP cell kinetics following Trametinib and BEZ235...	77
Figure 3-6: Targeting DTP states using VIPER informed pathway analysis.....	80

Figure 3-7: Drug combinations targeting DTP-enriched pathways still leave persisting cells of distinct identity.....	82
Figure 3-8: Combination therapy leaves distinct drug-persisting cells that are broadly drug-tolerant and can proliferate and recapitulate heterogeneity upon drug removal. ....	84
Figure 3-9: BET inhibitor combinations improve cell kill and suppress DTP transition. ....	86
Figure 3-10: JQ1 shows synergy with Trametinib and Trametinib + BEZ235 combinations. ....	88
Figure 3-11: Changes in open chromatin architecture underlie DTP transition and are inhibited by JQ1.....	90
Figure 3-12: JQ1 prevents BEZ235-driven changes in open chromatin architecture and TF accessibility.....	93
Figure 3-13: JQ1 prevents open chromatin architecture changes that support DTP state formation. ....	94
Figure 3-14: JQ1 combines with BEZ235 in vivo to reduce tumor volume and suppress cell-state transitions. ....	95
Figure 4-1: Activators of PP2A induce complete cytotoxicity in triple negative cell lines .	110
Figure 4-2: SMAPs effectively kill all differentiation states in heterogeneous TN cell lines and tumor models. ....	114
Figure 4-3: PP2A activators and kinase inhibitors act synergistically to inhibit TN cell proliferation. ....	116

Figure 6-1: Schematic of PI3K/mTOR inhibitor-induced changes in heterogeneous basal-like cell lines. .... 150

Figure 6-2: PP2A targets and pharmacological activators. .... 152

## Abbreviations

ATP	Adenosine triphosphate
AURK	Aurora kinase
BCCL	Breast cancer cell line
BCL2	B-Cell/CLL lymphoma 2
BET	Bromodomain extraterminal
BL1	Basal-like 1 subtype
BL2	Basal-like 2 subtype
BLG	Beta-lactoglobulin
Cre	Causes recombination
CI	Combination index
CI75	Combination index at 75% inhibitory dose
CI90	Combination index at 90% inhibitory dose
CIP2A	Cancerous inhibitor of PP2A
CSC	Cancer stem cell
DAPI	4,6-Diamidino-2-phenylindole
DAVID	Database for annotation, visualization and integrated discovery
DCIS	Ductal Carcinoma in Situ
DMEM	Dulbecco's modified eagle medium
DMSO	Dimethyl sulfoxide
DNA	Deoxyribonucleic acid
DTP	Drug tolerant persister
EdU	5-Ethynyl-2'-deoxyuridine
EGFR	Epidermal growth factor receptor
Einf	Projected effect at infinity - projected maximal inhibition
EMT	Epithelial-to-mesenchymal transition
ER	Estrogen receptor
ERK	Extracellular signal-regulated kinase

ERBB2	Erb-B2 receptor tyrosine kinase 2
EZH2	Enhancer of zeste 2 polycomb repressive complex 2 subunit
FFPE	Formalin-fixed, paraffin-embedded
FDA	Food and Drug Administration
FLOX	Flanked by LoxP
GEMM	Genetically engineered mouse model
GSEA	Geneset enrichment analysis
HER2	ErbB2 receptor
HER2E	HER2 Enriched subtype
IC50	Concentration where 50% inhibitory effect is observed
IdU	5- iodo-2-deoxyuridine
IF	Immunofluorescence
IM	Immunomodulatory subtype
JAK	Janus kinase
JNK	Jun amino-terminal kinase
K14	Cytokeratin 14
K17	Cytokeratin 17
K18	Cytokeratin 18
K19	Cytokeratin 19
K5	Cytokeratin 5
K8	Cytokeratin 8
KDM5B	Lysine demethylase 5B
KI	Kinase inhibitor
KRAS	Kristen Rat Sarcoma Oncogene Homolog
L-HER2	Luminal HER2 molecular subtype
LAR	Luminal androgen receptor subtype
M	Mesenchymal subtype
MAPK	Mitogen-activated protein kinase
MEK	Mitogen-activated-protein-kinase kinase

MFI	Mean Fluorescent Intensity
MSL	Mesenchymal stem like subtype
MTD	Maximum tolerated dose
mTOR	Mammalian target of rapamycin
Myc	V-Myc Avian Myelocytomatosis Viral Oncogene
PCA	Principle component analysis
PDX	Patient derived xenograft
PI3K	Phosphatidylinositol 3-kinase
PKC	Protein kinase C
PP2A	Protein phosphatase 2A
PR	Progesterone receptor
PTEN	Phosphatase and Tensin homolog
RAC	Ras-related C3 botulinum toxin substrate 1
RFS	ROSA-flox-stop
RNA	Ribonucleic acid
RPMI	Roswell Park Memorial Institute medium
SET	inhibitor 2 of PP2A
SMAP	Small molecule activator of PP2A
SRC	SRC Proto-Oncogene
t-SNE	t-stochastic neighborhood embedding
TCGA	The Cancer Genome Atlas
TF	Transcription factor
TN	Triple negative
UNS	Unstable subtype
VIM	Vimentin
WT	Wildtype

## Acknowledgements

I want to foremost thank Dr. Rosalie Sears for mentoring me over this long journey. I was quite a different scientist and person six years ago. Rosie's continued support, leadership, and unwavering curiosity for all things science have made her a strong role model for my development as a scientist, and proper west coast citizen. Rosie is never afraid to ask a question, seemingly never says no to collaboration, and often has candid "wow" moments of pure scientific joy from new discovery. This passion for science and great character has gotten her far, and through her vast network of collaborators I have been exposed to so many research topics, model systems, technologies, and colleagues that I could not envision a better training environment for a PhD candidate.

I would also like to thank Dr. Joe Gray for his mentorship. I would be on a very different research trajectory and writing a very different dissertation if it had not been for Joe's willingness to allow me to initiate a collaborative project in his lab and to mentor my progress throughout this program. Joe introduced me to so many new imaging platforms and imaging experts that I became a true convert to the church of quantitative imaging, and have not looked back since. Joe epitomizes many qualities of a great scientist that I hope to someday achieve. He is a true skeptic at heart in all the best ways, and has a knack for generating impactful questions from data that most of us would so often overlook. It was of course in Joe's lab four years ago that we observed that fluorescently-stained cells in a dish showed a beautiful array of different identities. While some would ignore this diversity, and others would chalk it up to transcriptional chaos, Joe's inquisition into the impact and origin of this heterogeneity lead me down a road of inquiry that has since revealed impactful discoveries that may improve patient therapy and produced the work in front of you.

I want to thank my dissertation committee for helping guide my research over the years. The suggestions put forth by Joe Gray, Soren Impey, Owen McCarty, Joshi Alumkal and Rosalie Sears helped keep my project on course and have greatly improved my ability to better guide my own research. I am grateful for all the Sears lab members without whom I could not have completed this work, we were the loudest lab, asked the most questions and definitely had the most fun on the block. I would also like to thank my graduate class, they have taught me powerful lessons in relativity, such as life seeming less difficult when everyone else around you is going through similar misery.

## Abstract

Our ability to therapeutically manage breast tumors has been revolutionized by the use of drugs targeting the activity of the estrogen and HER2 receptors. However, the efficacy of these treatments is restricted to tumors expressing/overexpressing these receptors, leaving the 18% of patients that lack ER and HER2 receptor expression minimal options for therapy. In particular, triple negative (TN) breast cancer patients are limited to a small set of chemotherapeutics for treatment options. Many small molecule kinase inhibitors are currently under clinical investigation for treatment of TN tumors, but despite targeting pathways shown to be commonly upregulated in this subtype, clinical success with these single agent targeted therapies has been poor. In this work we attempt to better understand the resistance mechanisms underlying the innate resistance of TN tumors to targeted kinase inhibitors. It is now widely appreciated that most tumors show intratumoral genomic heterogeneity due to a process of branched evolution. In this work we also demonstrate that triple negative tumors have high phenotypic heterogeneity, harboring multiple distinct cell states within a single tumor. Furthermore, we show that these tumor cell phenotypes are plastic, and cells can transition to drug-tolerant states upon therapeutic challenge with a wide range of targeted agents. This intratumoral heterogeneity and phenotypic plasticity likely supports the poor clinical successes of small molecule kinase inhibitor trials in TN patients. In order to improve future management of these tumors, we present two distinct therapeutic strategies that circumvent these resistance mechanisms and effectively kill heterogeneous

triple negative breast cancers. This includes combination therapy using targeted therapeutics in combination with epigenetic reader protein inhibitors, or the use of pharmacological activators of Protein Phosphatase 2a (PP2A), both of which showed promising efficacy in heterogeneous breast cancers. These studies provide new tools to detect heterogeneous breast tumors and provide new therapeutic strategies to treat these aggressive cancers.

# 1 Introduction

Breast cancer is the most diagnosed cancer in women in the United States, with a predicted 250,000 new cases to be diagnosed in 2017 and 40,000 new breast cancer deaths<sup>1</sup>. While these numbers are dramatic, significant advances in our ability to manage invasive female breast cancer with surgery and systemic therapy have resulted in a continual reduction of annual breast cancer deaths for the last two decades<sup>2</sup>. A major contributor to our improved ability to manage this disease was the development of targeted therapeutics against the estrogen (ER) and ErbB2 (HER2) receptors. However, due to the intertumoral heterogeneity of breast cancer<sup>\*</sup>, improvements in therapy have not been equally shared across the disease. Many tumors lack expression of ER and HER2, making them ineligible for use of ER and HER2-targeted agents. This leaves minimal treatment options for the approximately

---

<sup>\*</sup> Intertumoral heterogeneity refers to the diversity in tumor phenotype between different patients' tumors, or between multiple tumors of one patient. Differences have been described on many levels, genomics, histology, molecular expression, and more.

one sixth of invasive female breast cancer patients with triple negative (TN) breast cancers, which lack hormone receptor (ER, PR) expression and HER2 overexpression<sup>3-6</sup>. These TN patients are limited to a small set of chemotherapeutic agents for treatment, and many of these patients will fail on first line and second line chemotherapy. As a result of the lack of alternative therapies, we find that triple negative tumors have higher rates of residual risk than other breast cancers and have higher rates of early relapse<sup>3,7,8</sup>.

In order to improve this situation there is a large effort to identify and characterize targeted therapeutics for the treatment of triple negative tumors, and many such agents are currently under clinical trial investigation for use in triple negative breast cancer. TN tumors commonly show aberrant activation of the PI3K and MAPK pathways through various mechanisms, making them great candidates for the use of MEK and PI3K inhibitor therapy<sup>9-12</sup>. These agents have show strong antiproliferative efficacy in TN models *in vitro* and *in vivo*<sup>5,11,13</sup>, however, the success of these agents in the clinical setting has been limited, with no pathological complete responses and very few partial responses recorded in the numerous recently-concluded or ongoing MEK and PI3K pathway inhibitor trials<sup>14-17</sup>. Despite evidence that TN tumors utilize MAPK/MEK/ERK and PI3K pathway signaling for survival and proliferation, these tumors are often innately resistant to inhibitors of these pathways, or show a short window of benefit followed by rapid acquisition of drug resistance<sup>18</sup>.

It is evident that TN tumors possess intrinsic mechanisms of resistance that allow them to tolerate targeted therapy. A major contributor to this drug resistance is intratumoral heterogeneity, or the cell-to-cell diversity within a single tumor. Tumor cells with distinct

genomic aberrations and existing in distinct “cell states” or “phenotypes” \* can coexist within a single tumor. Because genomic and phenotypic differences can impart distinct sensitivity to therapy, cellular subpopulations with distinct genomic or phenotypic features can survive therapy through a process of Darwinian selection<sup>19–22</sup>. Further, tumor cell states are plastic, and tumor cells can transition between states through epigenomic change, allowing them to adapt to therapy by converting to a drug tolerant state<sup>23–25</sup>. These mechanisms represent major hurdles to the success of cytotoxic and targeted therapies in triple negative breast cancer, and will require the identification of novel therapeutic strategies that overcome these resistance mechanisms in order to improve our therapeutic management of subset of breast cancer patients.

Improving our therapeutic management of TN tumors will first require methods to measure cell state heterogeneity in order to identify heterogeneous tumors, which relatedly, have a high propensity for cell state transitions. Next, we must identify inhibitor combinations that target tumor cell survival and proliferation while simultaneously preventing adaptive cell-state plasticity; or alternatively, we must discover and develop agents that can simultaneously target all present tumor cell phenotypes without eliciting cell-state transition.

The research described herein details our efforts to develop systems to measure cell state heterogeneity within primary breast tumors and various models of breast cancer. We

---

\* These terms are used interchangeably throughout the literature and this work

show that cells-state heterogeneity is indeed pronounced in triple negative tumors, and in particular in the basal-like subtype. Basal-like cancers also show pronounced cell state plasticity, particularly when exposed to targeted therapeutic stress, supporting a link between cell-state heterogeneity and plasticity. In addition to our heterogeneity quantitation efforts, we present a comprehensive study that identifies therapeutic strategies to manage heterogeneous and plastic basal-like breast cancer using combinations of kinase inhibitors with inhibitors of epigenetic reader proteins. These drug combinations apply antiproliferative stress while preventing adaptive cell-state transitions, resulting in complete cell kill *in vitro* as well as basal-like tumor regression *in vivo*. Finally, we present an alternative strategy for effective treatment of heterogeneous TN tumors using activators of Protein Phosphatase 2A (PP2A). Pharmacologic reactivation of PP2A leads to the inhibition of multiple oncogenic pathways and kills heterogeneous TN cell lines and mouse models without eliciting phenotypic selection or adaptive cell-state transitions. These studies outline new methods to identify phenotypically heterogeneous tumors and provide two successful strategies to manage this aggressive form of breast cancer.

## 1.1 Intertumoral heterogeneity in breast cancer

### 1.1.1 Breast cancer subtypes

Breast cancer is a heterogeneous disease. This sentence has led so many publications and presentations that it has achieved colloquial status in this field, yet it continues to be used as a nod to the profound diversity of tumors found in this disease. Many classification systems have been developed historically to make sense of the intertumoral heterogeneity and to categorize tumors into subtypes that share phenotypic features and tumor behavior. Breast cancer patients are first classified by gender, age, tumor size, lymph node involvement, and tumor histology. Histological assessment involves interrogation for tumor grade, invasiveness, and histological type. There are many distinct breast cancer lesions based on histology, including precursor lesions\*, mesenchymal tumors, intraductal proliferative lesions, and benign proliferative lesions, which together encompass over 60 distinct histological classifications by World Health Organization standards<sup>26</sup>. The majority of breast cancers are invasive ductal carcinomas, occurring in female patients. These tumors are the most commonly lethal form of the disease, and the focus of most breast cancer research including this work. Immunohistochemical assays to identify molecular marker expression have also become standard practice in order to improve the stratification of tumors into subtypes that express the estrogen receptor (ER), progesterone receptor (PR), and ErbB2

---

\* Ductal Carcinoma in Situ (DCIS) or Lobular Carcinoma in Situ (LCIS)

(HER2) receptor<sup>27-29</sup>. This clinical assay divides tumors into a hormone receptor positive subtype (ER+, PR+/-, ~65-80% of breast cancer), HER2-receptor positive (15-30%)\*, and Triple Negative (~10-25%)<sup>3-5,30</sup>. These IHC-based subtypes have strong prognostic power, with distinct patterns of overall survival<sup>31</sup>, proliferative rates, sites of metastasis<sup>32</sup>, and rates of relapse<sup>31,33,34</sup>. Examination of additional IHC markers including Ki67, p53, and EGFR can enhance subtype resolution and has become standard practice in many clinics<sup>35,36</sup>.

With the advent of DNA microarray technology and next generation sequencing, tumors can now be profiled using thousands of expressed genes. Analysis of large tumor cohorts has revealed that tumors often fall into reoccurring patterns of molecular expression<sup>37</sup>, which have been termed the intrinsic subtypes of breast cancer. These subtypes include Luminal A, Luminal B, HER2-enriched (HER2E), Normal-like, Basal-like, and Claudin-low<sup>38,39</sup>. These molecular subtypes often show high overlap with the IHC-defined subtypes, as each intrinsic subtype has characteristic ER, PR and HER2 expression status, however, these overlaps are imperfect. For example, 80% of basal-like tumors are triple negative, whereas 70% of triple negative tumors are basal-like. These inconsistencies can be extremely important for treatment decisions, and its recommended to profile a patient tumor both by IHC receptor staining and by gene expression analysis and molecular subtyping<sup>40</sup>, which can be done through DNA microarray analysis or RNA-sequencing, using

---

\* Strong HER2 IHC positivity is used as a surrogate for existence of the Ch17q12 amplicon containing the HER2 gene, which can alternately be identified by gene amplification with Fluorescent In Situ Hybridization. IHC "Positive" = strong membrane staining (3+) in >10% of tumor cells. HER2 is often expressed in tumor cells but not at a level to be considered "+" in this assay

fresh-frozen or formalin-fixed paraffin-embedded (FFPE) tissue. from for. Further refinement of these intrinsic subtypes is continually ongoing to optimally separate tumors into groups with similar tumor behavior and therapeutic vulnerabilities, such as efforts to split luminal and basal HER2-enriched tumors<sup>41</sup>, or to split TN tumors to seven distinct subtypes<sup>5</sup>, as these further-segregated subtypes show distinct drug sensitivity and clinical behavior.

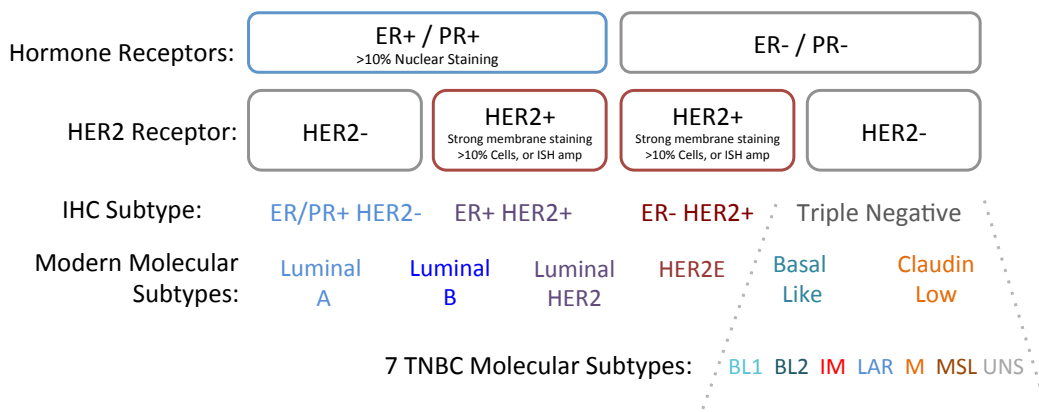


**Figure 1-1 Breast cancer subtypes**

A schematic portraying the intertumoral heterogeneity of female invasive breast tumors, first appreciated hormone receptor status, HER2 receptor status, IHC subtype based on these molecular markers, the currently appreciated molecular subtypes of breast cancer, and a recently developed TN subtype classification system. Subtypes vertically situated underneath each other have relatedness across the different classification systems, such as ER+/PR+/HER2- tumors being predominantly Luminal A, however complete overlap in these classification systems is never observed. ER, estrogen receptor; PR, progesterone receptor; BL1, basal-like 1; BL2, basal-like 2; IM, immunomodulatory; LAR, luminal androgen receptor; M, mesenchymal; MSL, mesenchymal stem-like; UNS, unstable.

### 1.1.2 Subtype targeted therapy

The use of chemotherapeutic agents is approved in all invasive breast cancers and involves a mix of anthracyclines (“A”, Doxorubicin, Epirubicin), Taxols or taxoteres (“T”, Paclitaxel, Docetaxel), and cytophosphamide (“C”, cytoxan)\*. Most chemotherapeutics are dosed as a combination or schedule of agents such as A+T, or A+C → T. While effective in some patients, tumors often become resistant to these treatments and eventually progress on therapy. To improve our therapeutic management of breast cancers, newer “targeted” therapies have been developed in the last few decades that selectively bind and modulate a particular molecular target. The initial developments of breast cancer targeted therapy focused on highly expressed oncogenic receptors that promote breast cancer proliferation, which coincidentally were the same receptors originally used to stratify patients. Estrogen receptor targeting agents include inhibitors of the estrogen production enzyme aromatase<sup>42</sup>, or drugs that bind and modify or downregulate the function of the estrogen receptor<sup>43</sup>. Similarly, agents have been developed that antagonize HER2 receptor activity through blocking receptor dimerization, or through competing for kinase substrate. The discovery and clinical implementation of these ER and HER2-targeted therapeutics has greatly improved overall survival in ER+ and HER2+/HER2E breast cancers, respectively<sup>44,45</sup>.

---

\* Platinum agents (Cisplatinum), 5-fluorouracil, and methotrexate are additional options for patients, which are similarly used in “cocktails” or sequences.

Additionally, other targeted agents including CD4/6 and mTOR inhibitors have been approved for use in ER+ breast cancer in combination with aromatase inhibitors<sup>46,47</sup>.

Triple negative breast cancers are a heterogeneous mixture of different tumor types. The two major molecular subtypes are basal-like (80% of TN tumors) and claudin-low (15% of TN tumors)<sup>38</sup>. TN tumors have distinct epidemiology, occurring in younger women and having higher rates of incidence in women of African American descent<sup>4</sup>. Further, TN tumors show distinct clinical behavior, having worse overall survival<sup>48</sup> and distinct high rates of relapse within the first few years of treatment<sup>7,34</sup>. Interestingly, triple negative tumors show increased sensitivity to chemotherapeutic agents compared to ER+ tumors<sup>49</sup>, however, patients that do not achieve pathologic complete response (pCR) show significantly worse overall survival compared to other subtypes<sup>7</sup>. This suggests that ineffective chemotherapy regimens leaves TN tumors in a more aggressive phenotype, and due to a lack of alternative treatment options to continue therapy, we observe a poor overall survival in these patients that fail first line therapy. These results highlight the need for new effective therapies for TN tumors, and understanding how to optimally use the currently approved therapeutics as to avoid treatment failure.

Many academic labs and pharmaceutical companies are working hard to alleviate the issue of limited treatment options for this patient population. Recurrent genomic aberrations in the disease, including mutations in *TP53*, *PI3K*, *RBI*, *PTEN*, and *BRCA1*, as well as common copy number alterations leading to gains in *AKT3* and *EGFR*, and loss in *INPP4B*<sup>6,50-53</sup>, all

converge to deregulate proliferation and survival pathway activity in TN tumors. This includes hyperactive PI3K and MAPK pathways due to recurrent PI3K, PTEN, and INPP4B mutations and EGFR amplification in this subtype<sup>9,10,54</sup>. These recurrent genomic aberrations and high MAPK/PI3K pathway activity make TN tumors a prime candidate for the use of targeted therapies against key kinases of the PI3K and MAPK pathways. Accordingly, numerous Phase I clinical trials are underway to establish the therapeutic dose to assess MAPK and PI3K pathway inhibitors in advanced TN breast cancers, including MEK1/2, PI3K, AKT, and mTOR targeted agents<sup>14–16,55–57</sup>.

Unfortunately, no beneficial TN tumor responses in these studies have been observed. There were no reports of complete response (CR), pathological complete response (pCR), partial response (PR), or stable disease (SD) in any TN patients. While tumor response was not the primary endpoint of these Phase I trials, and these advanced TN patients had already failed one or more lines of therapy, the lack of efficacy of these small-molecule kinase inhibitor is nonetheless discouraging. Kinase inhibitor combination therapies may provide a better opportunity for success in triple negative patients by simultaneously targeting multiple oncogenic pathways and/or preventing compensatory signaling. However, the success of MEK + PI3K inhibitor trials have still been limited for TN patients. In two different studies examining MEK inhibitors in combination with PI3K inhibitors in advanced solid tumors there were no reported positive outcomes for the TN patients in the studies<sup>58,59</sup>. Further, a more directed Phase II study examining the MEK inhibitor Trametinib in

combination with the AKT inhibitor GSK2141795 did report 2/31 patients achieving PR on Trametinib alone, and 1/16 achieving a PR on the combination treatment<sup>17</sup>, a lack of improvement over kinase inhibitor monotherapy.

### **1.1.3 Targeted therapies on the horizon for triple negative breast cancer**

Thankfully, better TN tumor responses have been observed in studies examining small molecule kinase inhibitors in combination with chemotherapeutic agents. An institution-wide examination of the ongoing Phase I clinical trials in TN patients at MD Anderson demonstrated that significantly better clinical responses are achieved with targeted therapeutics + chemotherapy\*, compared to either therapy alone, and compared to combinations of targeted agents<sup>57</sup>. 12 of 106 total treated patients had either PR, CR, or stable disease > 6 months, and 11/12 of these responders were in the chemotherapy + targeted therapy group. Further, a recent trial of the mTOR inhibitor Everolimus + Paclitaxel† showed promising antitumor efficacy, with all but one (22/23) TN patient experiencing stable disease or partial response to the combination treatment, and 2 patients having a complete responses and 7 patients having pathological complete responses, defined by the disappearance of the tumor by imaging (CT scan, CT/MRI, chest X-Ray), versus disappearance of invasive cancer cells in the breast and lymph nodes by pathological FFPE

---

\* Targeted agents included mTOR inhibitors, a PI3K inhibitor, or an AKT inhibitor + FGFR inhibitor

† Paclitaxel is a chemotherapeutic of the taxane family, which suppress microtubule dynamics and inhibit cell division

examination, respectively. These results emphasize the potential of combination therapy using kinase inhibitors with chemotherapy to treat TN tumors, while also highlighting the ineffectiveness of kinase inhibitors used as single agents of or as combinations to treat this disease.

It is apparent that although TN tumors have attractive biomarkers predicting sensitivity to pathway-targeted therapeutics, they additionally possess mechanisms to resist these agents. While kinase inhibitors show promise at enhancing the effects of chemotherapy in TN tumors, this strategy is not effective in all patients and alternative treatments are needed to better manage TN patient tumors. It is therefore critical that we determine the mechanisms leading to kinase inhibitor resistance in triple negative tumors and develop therapeutic strategies that circumvent these resistance mechanisms, unlocking the antitumor efficacy of our diverse arsenal targeted agents.

## **1.2 Intratumoral heterogeneity in breast cancer**

### **1.2.1 Clonal heterogeneity**

Heterogeneity in breast cancer extends beyond differences between patient tumors. Heterogeneity is also observed on the cellular level within single tumors. Tumor cell-to-cell differences exist across many measurable cellular control systems including the genome, methylome, chromatin architecture, transcriptional state, and microRNA expression state.

Genomic, or “clonal”, heterogeneity arises as transformed cells proliferate and genomic instability imparts *de novo* mutations or other genetic aberrations within tumor cell progeny. If these genomically-distinct progeny are sufficiently fit to exist within the tumor environment, clonal expansion occurs, leading to a process of branched evolution in the tumor. Indeed, multiregional sampling of breast tumors has demonstrated that branched genomic evolution occurs in breast tumorigenesis and most tumors are multiclonal at the time of resection<sup>21,60</sup>. Heritable changes in DNA methylation can also lead to subpopulations of cells with distinct gene enhancement or suppression<sup>61</sup> and tumors can similarly show branched evolution of this epigenomic identity.

### 1.2.2 Cell state heterogeneity

Intratumoral heterogeneity is also observed in cellular phenotype, where tumor cells within a single tumor can occupy distinct cell states. While there is no one shared definition of a tumor cell “state” or “phenotype”, it is widely considered to describe a repeatedly observed phenotype in a cell population that has a distinct molecular marker expression pattern (cell surface antigens, cytokeratins, hormone receptors etc.)<sup>62,63</sup>, a distinct gene expression pattern (cells within a state will cluster based on gene expression)<sup>64,65</sup>, and a distinct open chromatin architecture (accessible and repressed gene landscape)<sup>66,67</sup>. Due to these different systems of relatedness, tumor cell state heterogeneity can be assessed on many analysis platforms as long as they support single cell quantitation, these include:

immunohistochemistry (IHC) with single cell segmentation (marker expression), flow cytometry and mass cytometry\* (marker expression), single-cell RNA sequencing (gene expression), and single cell Assay-for-Transposase-Accessible Chromatin (ATAC) sequencing<sup>†68</sup> (open chromatin architecture). These assays allow for the interrogation of phenotypic marker expression (IHC, flow and mass cytometry), gene expression (single-cell RNA sequencing) and chromatin architecture (ATAC sequencing), respectively. Importantly, these heterogeneities can arise within a single genomic clone<sup>69,70</sup>, and each clone can show variations in their cell state heterogeneity.

Intratumoral heterogeneity does not evolve to be a chaotic mixture of different cell identities, rather, tumors repeatedly have discrete patterns of cell state diversity. Tumor cells commonly occupy aberrant versions of the normal cell states found in that organ system<sup>71</sup>, including stem-like states, lineage committed progenitors, differentiated cells of the tissue, and often expressing mixed phenotypic markers of these cell states<sup>22,63,72</sup>. The majority of past studies describing non-uniformity in tumor cell states have focused on describing subpopulations of cells with enhanced tumor initiating capacity<sup>51,73</sup>, self-renewal<sup>74-77</sup>, and drug resistance<sup>20,23,78</sup>, termed “cancer stem cells” (CSCs)<sup>79</sup>. Many groups have also described non-uniformity in mesenchymal cell identity in solid tumors, indicative of epithelial-to-mesenchymal transition<sup>22,73,80</sup>. Basal-luminal cell state heterogeneity is also observed in

---

\* Mass cytometry is like flow cytometry, but uses metal-tagged-antibodies and time-of flight spectrometry to read protein levels in single cells, allowing for simultaneous measurement of 30+ markers per cell.

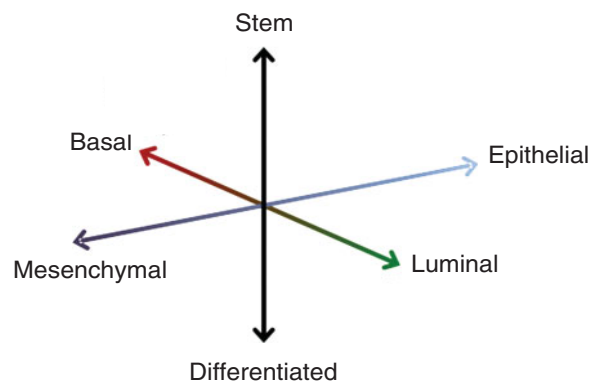
† ATAC sequencing uses a custom transposase to insert PCR primers into open chromatin, allowing for PCR amplification and sequencing of the open chromatin regions in a cell, showing what DNA is accessible to be expressed.

breast, lung, and bladder cancers<sup>72,81-83</sup>, and neuroendocrine-ductal heterogeneity in observed prostate and pancreatic cancers<sup>84,85</sup>.

Descriptions of intratumoral cell-state heterogeneity in breast cancer have included cells with relatedness to mammary stem cells, luminal progenitors, differentiated basal (myoepithelial) cells, differentiated luminal cells, and mesenchymally-transitioned cells<sup>22,38,51,67,72,86</sup>. Tumor cell states are often appreciated according to well-studied “axes of differentiation”, where a given cell can be within the spectrum of being more stem-like or more differentiated, more epithelial or more mesenchymal, or more basal or more luminal (Fig 1-2). Cell-to-cell differences are also appreciated regarding expression of therapy-relevant targets, including the estrogen receptor<sup>87</sup> and HER2 receptor<sup>88</sup>.

**Figure 1-2 Axes of differentiation in breast cancer**

A schematic showing the different axes of differentiation where breast tumor cells show phenotypic differences. A given breast tumor cell can exist in this three dimensional space with distinct identity on all three axes.



Adapted by permission from Wiley Periodicals Inc: WIREs Systems Biology and Medicine (Granit et al., WIREs, 2014), copyright (2014)

### 1.2.3 Darwinian selection

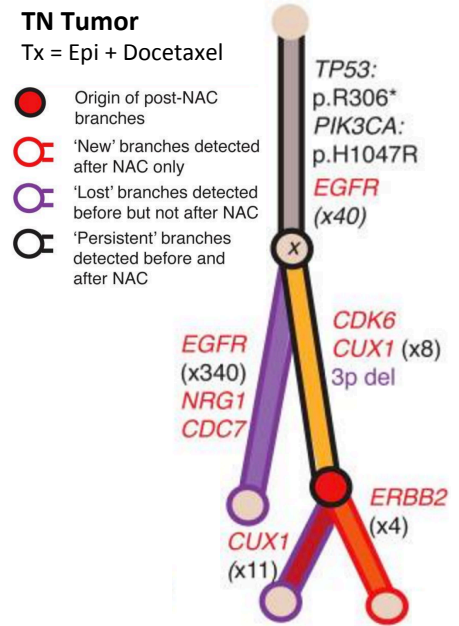
Due to the cell-to-cell differences in genomics, cellular differentiation state, and target molecule expression, intratumoral heterogeneity can produce differences in sensitivity to cytotoxic and targeted therapeutic agents. This allows a process of Darwinian selection to occur during therapy, whereby drug resistant cell populations with distinct genomic or phenotypic features are selected by therapy as other sensitive subpopulations die off, eventually leading acquired resistance and eventually, progression on therapy<sup>19,89</sup>.

Therapeutically-relevant genomic differences amongst tumor cells can include mutations in drug target genes themselves, rendering the drug ineffective in clones harboring this aberration<sup>90</sup>. Clonal genetic differences can also involve mutational activation of oncogenes or inactivation of tumor suppressors, which can similarly lead to drug resistance by altering the signaling network and bypassing the effect of therapy<sup>19</sup>. A recent longitudinal sequencing study by Yates et al.<sup>21</sup> examining breast tumor genomics before and after neoadjuvant chemotherapy revealed that breast tumors evolve in a process of branched evolution, generating distinct genomic clones throughout tumor lifespan, becoming multiclonal at the time of analysis by multiregional sequencing. Further, certain clonal “branches” are selected by therapy, whereas others die off during treatment.

**Figure 1-3: Branched evolution and clonal selection in TN tumors.**

Adapted from Yates et al, Nature Medicine, 2015<sup>21</sup>, a phylogenetic tree showing the clonal diversity in a triple negative patient tumor. The patient was treated with neoadjuvant chemotherapy combination of epirubicin and docetaxel, clones that were lost in post-treatment samples are outlined in purple, clones that were unique to post-treatment samples are outlined in red, and clones that persisted through treatment are outlined in black.

Adapted by permission from Macmillan Publishers Ltd: Nature Medicine (Yates et al., Nat Med., 2015), copyright (2015)



Similarly, tumor cell states can provide distinct drug sensitivities due to their differences in expression of target molecule expression (HER2, ER)<sup>87,88</sup> or drug efflux pumps<sup>91,92</sup>, as well differences in pathway activity. Consistent with this we observe differences in drug sensitivity between breast cancer subtypes that occupy distinct differentiation states<sup>5,13</sup>. In a recent study by Gomez-Miragaya et al.<sup>78</sup> they demonstrate that patient-derived triple negative breast tumors contain distinct subpopulations of cells with high CD49f expression that have increased innate resistance to taxane therapies, and are quickly selected for by repeated docetaxel dosing as tumors become resistant to treatment. This is consistent with other reports of cell-state selection following therapy, including mesenchymal cells and CSC-like cells<sup>20,22</sup>.

## 1.3 Cell state plasticity in breast cancer

### 1.3.1 Cell state plasticity in normal breast development and tissue maintenance

Unlike the genomic differences distinguishing tumor cell clones, the underlying signaling network structure and open chromatin architecture that support distinct cell states in tumors are dynamic and plastic; cells can switch states through a reversible transition process. These transitions are not a novel property gained through carcinogenesis, though arguably enhanced<sup>71,93</sup>, but instead are conserved differentiation, dedifferentiation, and transition processes that exist in embryogenesis, development, and in the adult to support wound healing and tissue maintenance<sup>94</sup>.

In the developing mouse fetus, the mammary gland starts as an offshoot of the ventral ectoderm which forms ductal sprouts around embryonic day 16<sup>95</sup>. At day 16.5, this previously dormant rudiment becomes highly active, where cells enter an active mammary stem state and begin to proliferate and invade the mammary fatpad, elongating the ductal network. Following this rapid morphogenesis, the mammary gland slowly matures until puberty, where another rapid elongation phase occurs. A mammary stem cell (MASC) population with bipotent potential persists throughout life, however, the MASC phenotype is variable at different stages in life; fetal mammary stem cells (fMASC) and adult mammary stem cells (aMASC) have many divergent features<sup>51,95-97</sup>. While fMASC in humans have yet to

be described, mammary gland development in the human is thought to follow a similar path as mouse mammary gland development, and aMASCs from adult mice and adult humans show strong similarities in gene expression<sup>98</sup>. During development in the human, mammary stem cells differentiate into luminal and myoepithelial-lineage restricted progenitors, which are populated throughout the branched ductal network, and asymmetrically divide to produce differentiated luminal\* or myoepithelial cell progeny, respectively. Additionally, epithelial cells are often called upon to undergo EMT to generate mesenchymal states, which is necessary to carry out mammary gland restructuring during various stages in development including puberty, pregnancy, and wound healing<sup>99</sup>. EMT is a reversible process, as mesenchymal cells can undergo mesenchymal-to-epithelial transition back to epithelial identity. Unlike the well-described bidirectionality of EMT, differentiation from a more stem-like state to a mature cell state is generally regarded as a unidirectional process. However, studies have demonstrated that particular cellular stresses can elicit a reverse transit of differentiated cells back to more multipotent states in many tissue systems<sup>94</sup> and it is likely that breast progenitors and even differentiated cell types may possess this dedifferentiation capacity given the right cellular signals. Following tissue injury, where wound healing requires the regeneration of the MASC population in the newly formed tissue, it is hypothesized that dedifferentiation of non-stem breast cells facilitates this process<sup>94</sup>.

---

\* Differentiated luminal cells of the breast include both ductal cells and alveolar cells. Alveolar cells are primarily located at terminal end buds of ducts and are the specialized secretory cell of the organ.

### 1.3.2 The regulation of chromatin, transcription factors, and cell state

Control over cellular differentiation involves the epigenetic regulation of the genome through DNA methylation and histone modifications, enabling enhancement or suppression of key differentiation regulators and genes, including cell-fate determining transcription factors. Specification of tissue lineages from the germ layers during embryogenesis uses DNA methylation to restrict gene expression to tissue-specific programs<sup>100</sup>. Changes in DNA methylation continue to support cellular differentiation throughout life, but cell specialization/differentiation within specific tissue lineages, e.g. the mammary epithelium, is primarily carried out through regulating the open chromatin architecture of the genome<sup>66,101</sup>. Changes in chromatin condensation and “openness” can direct transcriptional machinery to particular promoters and enhancers. Open chromatin architecture changes can be controlled by regulating the location and activity of histone modification enzymes, which enhance or restrict chromatin accessibility through regulating enhancing acetylation of histone lysine residues, or methylation of histone lysine and arginine residues, which can be either enhancing or repressive<sup>102–104</sup>. As well, regulation of histone-modification reader proteins like the bromodomain and extraterminal (BET) family can dictate which open regions undergo chromatin looping and transcriptional initiation<sup>105,106</sup>, adding another level of gene expression control. This allows the cell to rapidly alter gene expression patterns through chromatin dynamics, allowing for cell-state transitions in response to stress like wound healing, or to support tissue maintenance and development (see 1.3.1)<sup>107</sup>. This control over gene

expression through chromatin dynamics is observed in basal mammary epithelial cells, where “bivalent” activating and repressive histone modifications are found on the ZEB1 gene locus, and allow for rapid acquisition of a ZEB1-expressing state through further addition of activating histone marks<sup>108</sup>. Many fate-determining transcription factors (TFs) are believed to exist in this bivalent state at their enhancers and promoters, allowing for quick gene expression change by tipping the prevalence of activating or repressive histone marks in either direction<sup>109</sup>. Chromatin state regulation of such cell-fate determining transcription factors gives the cell a tunable and reversible system to control cell differentiation. In this mammary gland, particular sets of transcription factors control lineage differentiation, including the luminal differentiation drivers ESR1, FOXA1, and GATA3, and the myoepithelial differentiation drivers TP63, SLUG, and EGR1<sup>103,110,111</sup>. Furthermore, epigenetic regulation of the EMT-promotional TFs ZEB1, SNAIL, and TWIST, allow for control over mesenchymal transition<sup>99,112,113</sup>. Many of these factors work in positive feedback loops, enhancing their own expression to maintain cell state<sup>114</sup>. Even the activity of singular TFs can have robust control over cell state. Dravis et al<sup>115</sup> show that SOX10 expression alone can promote transition from a more differentiated epithelial state into a stem-like, multipotent state in fetal mammary cells by increases in SOX10 expression alone. Further increases in SOX10 expression then stimulate transition from this stem-like epithelial state to a mesenchymal, motile state.

### 1.3.3 The influence of therapy on tumor cell state

Particular cancers and cancer subtypes show high rates of cell state heterogeneity, including glioblastoma, small cell lung cancer, colorectal cancer, and triple negative breast cancer<sup>22,63,64,67,83,116</sup>. Cell lines derived from patients with these cancers show an increased propensity for cell-state transition. Cell sorting experiments in TN cell lines demonstrate that distinct cell basal, luminal, and stem-like cell states co-exist in these cultures, and that following cell-state isolation, the isolated cell-state will recapitulate cell-state heterogeneity over time through cell-state transitions<sup>72,93</sup>. This process of stochastic state transition maintains a particular equilibrium of cell-states under normal growth conditions, with the ratio of states at equilibrium being specific to each cell line<sup>67,69,117,118</sup>.

The plasticity of cancer cell states is exemplified when the cell population is exposed to extrinsic stresses, including signals and stresses from the microenvironment<sup>119,120</sup>, as well as therapeutic stress. Upon exposure to cytotoxic and targeted therapies, cancer cells can transition to distinct drug tolerant persister (DTP) states and survive the therapy in a low-proliferative state<sup>24,25,67,121,122</sup>. This transition is rapid, occurring after just 72-hr of treatment in numerous studies<sup>24,25,121,122</sup> and detectable at 12hr by imaging our studies<sup>67</sup>, and detectable by gene-level epigenetic changes as early as 1hr post treatment in a study by Zawitowski et al.<sup>18</sup>, who demonstrate these gene-level epigenetic changes continue to increase over the course of a week. Despite the rapid acquisition of the DTP phenotype, cells

appear to maintain this state indefinitely\* as long as drug pressure is sustained<sup>24,67</sup>. It is important to note that this drug tolerance mechanism is independent of clonal selection due to genetic resistance, and in these long-term drug exposure experiments both mechanisms were evident, with the population at large surviving in a low-proliferative DTP state, but clones of proliferative cells also emerging and expanding that harbored resistance-conferring mutations upon sequencing analysis<sup>24</sup>.

Consistent with the epigenetic mechanisms involved in cellular control over differentiation state in normal tissue systems (see 1.3.2), we find that therapy-induced cell-state plasticity evokes similar epigenetic processes. Changes in chromatin modifier enzyme activity are observed following chemotoxic and targeted therapy including the activation of the KDM family of histone demethylases in response to temozolomide in glioblastoma and in response to EGFR-targeted therapy in lung cancer<sup>24,122</sup>, as well as histone acetyl transferase activity in response to targeted MEK inhibitors in breast cancer<sup>18</sup>. Further, therapeutic stress also stimulated the activity of the Bromodomain and Extraterminal (BET) family of histone acetyl-reader proteins in response to HER2-targeted therapy<sup>123</sup>, PI3K-targeted therapy<sup>124</sup>, and MEK-targeted therapy<sup>18</sup> in breast cancer cell lines. This included the BET family member BRD4, which has also been shown to possess both histone acetyl reader functions and histone acetyl-transferase (HAT) activity<sup>125</sup>. Transition to a new cell state requires dynamic chromatin remodeling, involving the opening of chromatin to activate new genes as well as

---

\* DTP cells remained until all long-term culture experiments were ended, this was 3 weeks in our study<sup>67</sup> and “weeks” in another study<sup>24</sup>.

the condensation of chromatin to inactivate of currently expressed genes. It is therefore likely that drug-induced state transitions involve the activity of many chromatin-modifier protein families including histone de-acetylases (HDACs) and histone methyl-transferases in addition to the histone acetyl-transferases and histone demethylases mentioned above.

A recent study by Zawistowski et al<sup>18</sup> details the gene level changes in histone modifications as targeted MEK inhibitors induce an adaptive transcriptional responses in breast cancer cells. They demonstrate that in response to MEK inhibitors, TN breast cancer cell lines up-regulate numerous kinases to maintain cell survival signaling. These gene expression changes involve the regulation of gene enhancer histone acetylation, and histone demethylation, and involve the activity of BRD4, histone acetyl-transferase p300, histone methyl-transferase JMJD6. While their study focused on changes in compensatory kinase gene activation and did not assess cellular differentiation state, they used the same therapeutic agents and cell line models as our study, and the kinetics of these epigenetic changes align with our observations of DTP state transition and open chromatin architecture remodeling<sup>67</sup>. Further, therapeutic inhibition of BRD4 similarly attenuated the state changes in their study similar to our observations. Together, these results suggest that chromatin-state changes on enhancers of both kinase genes and fate-determining transcription factor genes are co-occurring during the transition to a drug tolerant persister state.

### 1.3.4 Therapeutic strategies to combat plasticity

To improve the efficacy of targeted therapy in TN tumors it is critical that we suppress cell-state transitions. Due to the involvement of numerous epigenetic modifier and reader proteins in adaptive chromatin remodeling, many groups have found success through pharmacological targeting of the epigenetic enzymes that support enhancer activation. Sharma et al<sup>24</sup> and Banelli et al<sup>122</sup> demonstrate that KDM-family histone demethylases activity support the DTP formation in treated NSCLC cell lines and glioblastoma cell lines, respectively, and that small-molecule HDAC inhibitors function to inhibit KDM activity, suppressing DTP formation and improve cell kill.

Targeting the activity of BET proteins is also an effective strategy to prevent DTP generation. Numerous drug companies are developing small molecule BET inhibitors. These drugs compete with acetylated histone residues for BRD2/3/4 binding, inhibiting the epigenetic reader function of these enzymes. These agents show great potential at preventing adaptive enhancer remodeling and transition to DTP states<sup>18,67,123,124</sup>.

Finally, drug strategies that involve the simultaneous inhibition of multiple signaling pathways can be successful at treating heterogeneous and plastic tumors. The proper selection of kinase-targeted inhibitors, which would inhibit the full spectrum of subpopulation dependencies, will in theory be effective at heterogeneous tumor inhibition. However, in practice, each two-drug combination tested in our study<sup>67</sup> still produced drug tolerant persisting cells. Consistent with this, dual kinase inhibitor combinations have not

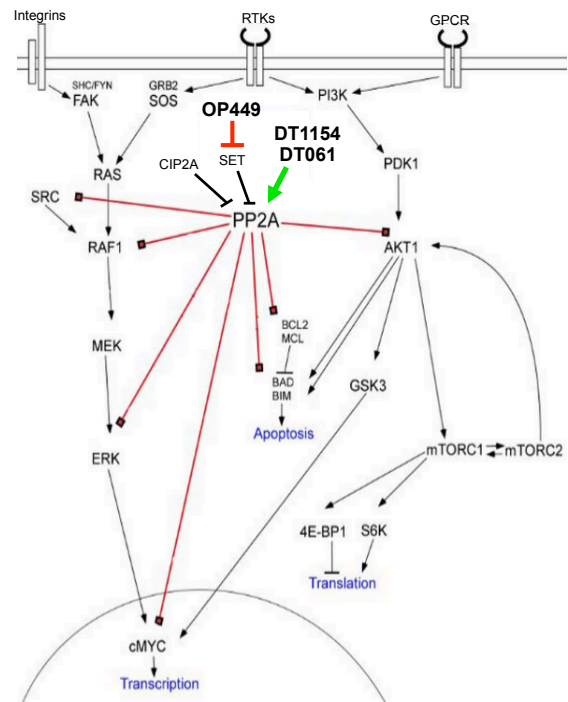
shown great success in clinical trials of TN patients<sup>57-59</sup>. This may be due to two agents being insufficient at fully covering the necessary pathways to inhibit all cancer cell subpopulations, which may be alleviated by increasing the number of administered drugs, but we are limited in the number of simultaneous drugs that can be dosed due to drug side effects and toxicity, making it impractical to research 3 or 4-drug combinations. Sequential therapies may offer more promise, where one drug is administered followed by a second agent that targets the adaptive pathway changes leading to DTP formation. Supporting this concept, administering a SRC inhibitor within the first 24 hours of applying taxane therapy can greatly improve cell kill and tumor regression<sup>25</sup>.

An orthogonal approach to achieve simultaneous inhibition of numerous signaling pathways may be through the use of pharmacologic activators Protein Phosphatase 2A (PP2A). PP2A functions to dephosphorylate a broad range of cellular signaling molecules, including kinases in the MAPK and PI3K pathways, c-Myc, Src, and the apoptosis regulators BAD and BCL2. In a normal cell, PP2A counteracts the activities of cellular kinases through dephosphorylating kinase targets or the kinases themselves, adding a second level of control to signaling pathway activity<sup>126,127</sup>. During tumorigenesis, however, most cancers lose the expression or activity of PP2A<sup>128,129</sup>, leading to unchecked oncogenic pathway signaling. Because of this, the pharmacologic activation PP2A results in rapid dephosphorylation and inactivation of proliferative and survival signaling mediators, resulting in cancer cell cytotoxicity and tumor growth inhibition in various cancers<sup>130-133</sup>. Due to the simultaneous inhibition of numerous signaling pathways, we proposed that PP2A activators may

circumvent TN tumor resistance due to Darwinian selection and cell-state plasticity. We show here that two distinct strategies of PP2A activation results in robust cytotoxicity of TN cell lines without evidence of phenotypic selection or induction of phenotypic plasticity. Furthermore, these PP2A activators effectively inhibited tumor growth in TN mouse models, demonstrating the potential of these activators to treat heterogeneous and plastic breast cancers.

**Figure 1-4: PP2A targets and activating agents.**

A schematic showing a reduced network of the proteins regulated by PP2A (red lines). Also included are the endogenous inhibitors of PP2A: SET and CIP2A. Therapeutic agents that activate PP2A are also shown, including OP449, which competes for SET binding, relieving endogenous PP2A repression, as well as the small-molecule activators of PP2A: DT061 and DT1154.



## 1.4 Summary

Breast cancers display heterogeneity from a macro to micro level, with profound tumor-to-tumor differences and cell-to-cell differences in single tumors. Additionally, we now appreciate that tumor cells are phenotypically plastic and can adapt to therapeutic stress

through adaptive cell-state transitions. This heterogeneity and plasticity has only been well-studied in the last decade, and there is still much to be discovered about the heterogeneity between, and within tumors. Further, there is much to discover about how tumor cells elicit changes to the chromatin landscape and undergo cell-state transitions. Standard of care treatment strategies were established before many of these discoveries on intratumoral heterogeneity and cell-state plasticity occurred. Resultantly, current clinical practices do not properly appreciate the mechanisms of resistance that intratumoral heterogeneity and plasticity present. In order to improve the therapeutic management of triple negative tumors, we need to adapt our clinical protocols so that they appropriately target the heterogeneity found within tumors, without selecting for- or inducing aggressive and deadly tumor subpopulations. This will first require the implementation of better strategies to measure clonal and phenotypic heterogeneity in tumors to identify those patients that are prone to these resistance mechanisms. Additionally, significant research into new drug combinations, drug sequences, or novel multi-targeted drugs will be needed to develop therapies that best manage these heterogeneous and plastic tumors.

## 2 Measuring cell state heterogeneity in breast cancer

**Tyler Risom**, Koei Chin, Juha Rantala, Nick Kendsersky, Lacey Dobrolecki, Mike Lewis,  
Joe Gray, Rosalie Sears

The data presented in this chapter is taken from a manuscript titled Measuring and Managing Cell State Plasticity in Basal-Like Breast Cancer to Improve Therapeutic Control, which is in review at Nature Communications. I designed the experiments detailed in this chapter with mentoring from the other authors. Mike Lewis and Lacey Dobrolecki prepared the patient-derived xenograft TMAs. I personally performed every experiment and analyzed the data.

## 2.1 Abstract

Tumor cells exhibit an enhanced trait of phenotypic plasticity, and are prone to differentiation state transitions both stochastically and in response to extrinsic signals. In breast cancer, this plasticity results in the coexistence of tumor cells with diverse cellular phenotypes within the same tumor, known as intratumoral phenotypic heterogeneity. As this heterogeneity may support therapeutic resistance and tumor behavior including metastasis and invasion, it is critical that we develop systems to quantify this heterogeneity in order to identify heterogeneous tumors and treat them appropriately. By utilizing markers of cellular differentiation with multi-color immunofluorescence, and novel methods of automated single cell image-analysis, we have developed a system to measure phenotypic heterogeneity in primary breast tumors, animal models of breast cancer, and breast cancer cell lines. We used this system to demonstrate that tumors of the triple negative and basal-like subtypes possess higher levels of phenotypic heterogeneity than other subtypes. Advancement of the image-based and gene expression-based metrics of phenotypic heterogeneity used in this work will provide useful tools for the identification of patients with high intratumor heterogeneity that may require alternative treatment strategies.

## 2.2 Introduction

Intratumoral cell-state heterogeneity is observed in many cancers, where within a single tumor, tumor cells can occupy different cell states marked by distinct molecular expression patterns relating to unique cell function. Historically, this has focused on identifying tumor cells with enhanced self-renewal and tumorigenic potential, or “cancer stem cells” (CSCs)<sup>51,74,78,86,51,73,77,85</sup>, but studies have also described the non-uniformity in mesenchymal cell-state identity<sup>22,83,134</sup>, and diversity in cell states resembling normal differentiated states in the cancer’s respective tissue of origin<sup>51,72,75</sup>. This heterogeneity is pronounced in certain cancers and cancer subtypes including glioblastoma<sup>64,70,135</sup>, small cell lung cancer<sup>83,119</sup>, colon cancer<sup>65</sup>, and HER2+ and triple negative breast cancers, and studies have shown cell lines derived from these tumors not only show this heterogeneity *in vitro*<sup>67,70,93,117,118</sup>, but the distinct cell states have the capacity to recapitulate cell state heterogeneity if isolated and allowed to grow over time<sup>70,93,118</sup>. These observations draw a direct link between cell state plasticity and cell state heterogeneity, suggesting that heterogeneity is a consequence of an enhanced capacity to exist in, and transition between, distinct cell states.

Cell state heterogeneity and plasticity have important implications regarding cancer therapy. Distinct cancer cell states show specificity in drug sensitivity<sup>5,80,93</sup>, suggesting that Darwinian selection of particular drug-resistant cell states can occur during treatment. Consistent with this, particular state enrichments are observed post-therapy<sup>20,22,116</sup>.

Furthermore, cell-state plasticity can allow cells to transition to “drug tolerant persister” states that survive therapeutic stress<sup>18,67,70,108,136–138</sup>, again leading to acquired resistance.

Due to the therapeutic implications of cell-state heterogeneity and its known correlations to specific subtypes of cancer, cell state heterogeneity may represent a powerful metric to better improve patient tumor diagnosis, prognosis, and treatment selection. Consistent with this, an 2006 study demonstrated significant differences in overall survival comparing tumors that show heterogeneity basal and luminal cell state identity, versus tumors that were more homogeneously basal or luminal<sup>81</sup>. These findings support efforts to develop new imaging systems that can quantify single cell phenotypes within patient tumors and calculate a metric of cell-state heterogeneity. In this study we develop an immunofluorescent (IF) imaging protocol and image analysis pipeline that allows for the measurement of single cell phenotypes within numerous primary breast cancers and breast cancer models. We focus on heterogeneity in differentiation states defined by the expression of luminal, basal, and mesenchymal cell state markers, and employ the Shannon Diversity index<sup>88,116,139</sup> as a metric of cell-state heterogeneity. Using this system, we are able to demonstrate that the triple negative and basal-like subtypes are enriched for cell-state heterogeneity, and that this heterogeneity is conserved within *in vitro* and *in vivo* in models of triple negative breast cancer. We also explore a novel method to calculate differentiation-state heterogeneity based on gene expression levels, which may be a provide an alternative

tool to assess tumor heterogeneity particularly in cases where tissue sections are unavailable for imaging analysis but tumor RNA exists.

## 2.3 Results

### 2.3.1 Differentiation-state heterogeneity in primary breast cancers and patient derived cell lines

We examined the relationship between differentiation-state heterogeneity and breast tumor subtype in primary patient samples, patient derived xenografts (PDX), and breast cancer cell lines. We measured single cell expression of Cytokeratin 19 (K19), Cytokeratin 14 (K14), and Vimentin (VIM) to define distinct differentiation states, and to serve as an operational metric of cell state heterogeneity. These intermediate filament markers are preferentially expressed in the luminal, myoepithelial (basal), and mesenchymal cell states of the normal breast, respectively<sup>51,117,118,140–142</sup>. We first profiled treatment-naïve tumors of varying hormone receptor status, including “luminal” (ER<sup>+</sup>/PR<sup>-</sup>/HER2<sup>-</sup>), HER2+ (ER<sup>+/-</sup>/PR<sup>-</sup>/HER2<sup>+</sup>) and triple-negative (TN, ER<sup>-</sup>/PR<sup>-</sup>/HER2<sup>-</sup>) tumors using immunofluorescent imaging and automated single cell image quantitation, multiple tumor regions were analyzed if possible (Fig. 2-1a, b). Nuclei were detected using a DNA counterstain (DAPI) and a cytoplasmic signal detection mask was extended from each nucleus to measure cytoplasmic

marker expression. Single cell data was then analyzed with cytometry software, where gates for single cells and marker positivity were determined based on marker-negative controls. All epithelial-marker positive cells ( $K19^+$  or  $K14^+$ ) were considered to be tumor derived, excluding histologically determined normal structures and DCIS lesions. Cell phenotype is calculated based on expression of the three markers, and the cell phenotypes are mapped in an X/Y dot plot to visualize cell-state heterogeneity in the tissue (Fig. 2-1b, bottom). We calculated the frequency of differentiation states within each tumor region and the diversity of these states using the Shannon diversity index (Fig. 2-1c). Using this method, we found that luminal tumours and the  $HER2^+/ER^+$  tumours were almost exclusively comprised of a  $K19^+/K14^-/VIM^-$  differentiation-state (Appendix A-2). In contrast, most TN tumors contained numerous K19, K14, and VIM-defined differentiation states, including robust proportions of epithelial tumor cells expressing more than one of these differentiation state markers. It is important to note that a low rates of  $K19^+/VIM^+$  false positivity was observed within all tumors due to the close proximity of  $K19^+$  tumor cells and  $VIM^+$  stroma. A subpopulation of  $K19^+/K14^+/VIM^-$  cells was observed in most  $HER2^+/ER^-$  tumors (2/3) whereas all other  $HER2^+$  tumors were K19-dominant like the luminal group. As a result, the mean Shannon diversity index was significantly higher in TN tumors than in non-TN tumors (Fig. 2-1d). We next examined 31 molecularly-profiled PDX tumors<sup>143</sup> to examine the relationship between differentiation-state heterogeneity and molecular subtype. Patients were of varying hormone receptor status and molecular subtype (Fig. 2-1e, f, Appendix A-3). The PDX models allowed us to distinguish tumor cells through the use of human-specific

antibodies against nuclear protein Ku80, expanding the measurable tumor subpopulations to also include  $K19^-/K14^-/VIM^+$  cells, and tumor cells that lacked expression of our differentiation marker set. We observed robust heterogeneity within these PDX models, likely related to the overrepresentation of TN and basal-like tumors in the set (Fig. 2-1f). Once again, the Shannon diversity index was significantly higher in TN tumors compared to non-TN tumors (Fig. 2-1g), consistent with our observations in primary patient samples. Further, tumors of the basal-like molecular subtype had significantly higher Shannon diversity indices than HER2-Enriched (HER2E) subtype tumors (Fig. 2-1h).



eight tumor cell states based on K19, K14 and VIM expression is shown for 31 patient-derived xenograft tumors in a vertical scatterplot with accompanying Shannon index, patient ER, PR and HER2-receptor status, and intrinsic molecular subtype denoted by color: HER2E (purple), basal-like (cyan). Tumors are arranged left to right by increasing Shannon index.

### **2.3.2 Differentiation-state heterogeneity in breast cancer cell lines**

We next examined differentiation-state heterogeneity in breast-cancer cell lines (BCCLs) using high-content immunofluorescent of luminal B, HER2+, basal-like, and claudin-low cell lines (Fig. 2-2a). DAPI signal was again used to identify single nuclei and the nuclei shape was expanded to measure cytoplasmic signal, here however, the nuclear region was excluded from cytoplasmic signal measurements (Fig. 2-2b). Signal intensity of K19, K14, and VIM was measured in each cell cytoplasm mask, and cellular mean fluorescent intensities (MFI) were plotted on bivariate dot plots showing the MFI distribution of each cell line (Fig. 2-2c). Marker positivity gates were established using cell lines that lacked K19, K14, or VIM expression as negative controls, and the frequency of eight differentiation states was calculated along with the Shannon diversity index for each cell line (Fig. 2-2d). IF and image cytometry profiling of these lines supported our observations in the primary cancers and PDX tumors: triple negative cell lines had significantly higher diversity indices than non-TN lines, and both TN molecular subtypes (basal-like and claudin low) showed significantly higher diversity indices compared to luminal B and HER2E subtype BCCLs (Fig. 2-2e). Cell state heterogeneity persisted in 3-dimensional culture as well as in orthotopic xenografts of these cell lines (Fig. 2-2f).

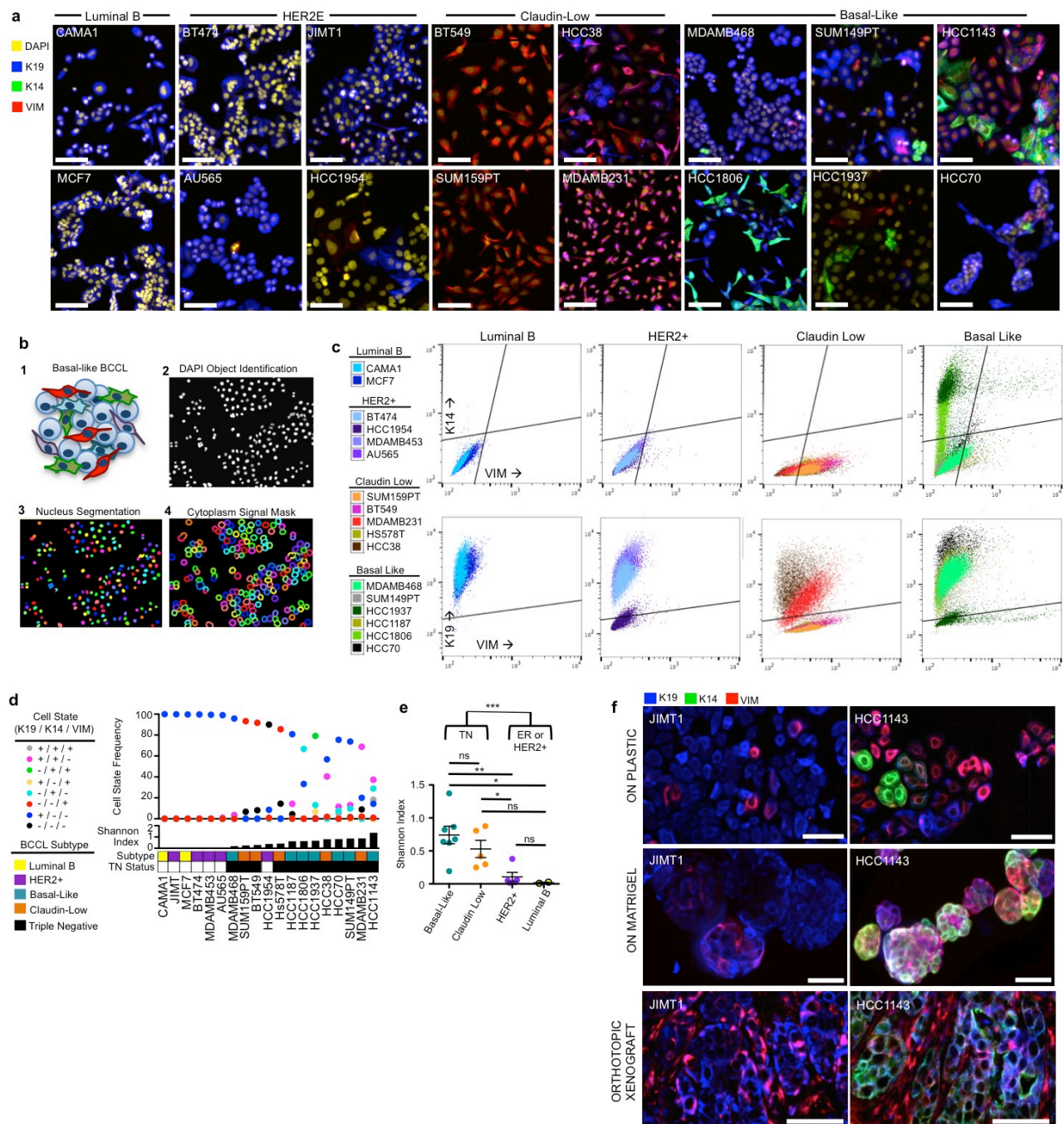


**Figure 2-2: Breast cancer cell lines model the differentiation state heterogeneity observed in their tumor subtype of origin.**

(A) IF images of BCCLs with differing molecular subtypes stained for DAPI (yellow), K19 (blue), K14 (green) and VIM (red), scale bars = 100µm. (B) A schematic showing the method of single cell segmentation and cytoplasmic signal quantitation in IF images of cell lines. (C) Bivariate dot

plots comparing K14 vs. VIM (top) and K19 vs VIM (bottom) are shown showing single cell identity of BCCLs of the Luminal B, HER2+, claudin-low, and basal-like. **(D)** The frequency of eight cell states based on K19, K14, and VIM expression is shown for each BCCL in a vertical scatterplot with accompanying Shannon index and molecular subtype denoted by color: luminal B (yellow), HER2+ (purple), basal-like (cyan), claudin-low (orange). Triple negative (TN) status is marked by black squares. Cell lines are arranged left to right by increasing Shannon index. **(E)** Graph of Shannon index, comparing TN and non-TN BCCLs, as well as different molecular subtypes. \*P < 0.05, \*\*P < 0.01, \*\*\*P < 0.001, ns = not significant, SEM shown. **(F)** Images showing the HER2+ cell line JIMT1 and basal-like line HCC1143 grown on 2D plastic, grown in 3D on matrigel, and grown in orthotopic xenografts. All stained with K19 (blue), K14 (green), and VIM (red).

### **2.3.3 Assessing differentiation-state heterogeneity through gene expression**

We next examined expanded sets of luminal-, basal-, and mesenchymal-marker gene expression in RNAseq data from BCCLs<sup>144</sup>. We focused on the expression of 20-gene gene sets for each lineage, including those demonstrated to be specific to the luminal or myoepithelial differentiations states of the normal breast, as well as 20 classic epithelial-to-mesenchymal transition markers<sup>51,103,117,118,141,142,145–148</sup> (Fig. 2-3a). We performed unsupervised clustering on 44 BCCLs originally derived from patient samples using these 60 genes. Consistent with our imaging, claudin low lines clustered with dominant mesenchymal gene expression, and luminal B lines, as well as the majority of HER2+ lines, clustered with dominant expression of luminal genes. Basal-like lines expressed myoepithelial-specific (basal) genes, but also showed high levels of luminal gene expression and mesenchymal gene expression. We calculated the cumulative Z-score mean of the luminal, myoepithelial, and

EMT geneset expression to serve as a metric of molecular differentiation-state heterogeneity (Fig. 2-3b), and the basal-like lines showed significantly higher values of this metric compared to all other groups (Fig. 2-3c). Further, basal-like lines showed significantly lower variance between geneset means compared to all other subtypes (Fig. 2-3c). The HER2+ lines showed a bimodal distribution in geneset variance. A recent gene expression analysis of hundreds of breast cancers by The Cancer Genome Atlas revealed that two very distinct molecular subtypes exist in human HER2+ tumors, one with more luminal features and commonly ER+ termed luminal-HER2 (L-HER2), and another set of tumors that show higher basal gene expression and are rarely ER+, termed HER-enriched (HER2E). We separated the HER2+ cell lines based on their L-HER2 and HER2E subtype<sup>149</sup> and observed that HER2E cell lines showed significantly lower variance between lineage genesets (Fig. 2-3e). Finally we tested the concordance between our heterogeneity calculations from imaging and gene expression analysis. We compared the Shannon diversity index from K19/K14/VIM differentiation-state heterogeneity determined in imaging studies (Fig. 2-2d), to the variance between lineage geneset averages, and observed a significant inverse relationship between the two metrics (Fig. 2-3f,  $R^2=0.356$ ,  $P = 0.011$ ). Cell lines with high Shannon diversity indices in the imaging analysis had low variance in luminal/basal/mesenchymal geneset averages, and vice versa. Further, molecular subtypes grouped in this bivariate analysis, basal-like lines showing low variance and high Shannon indices, and luminal and L-HER2 lines having high variance and low Shannon indices.

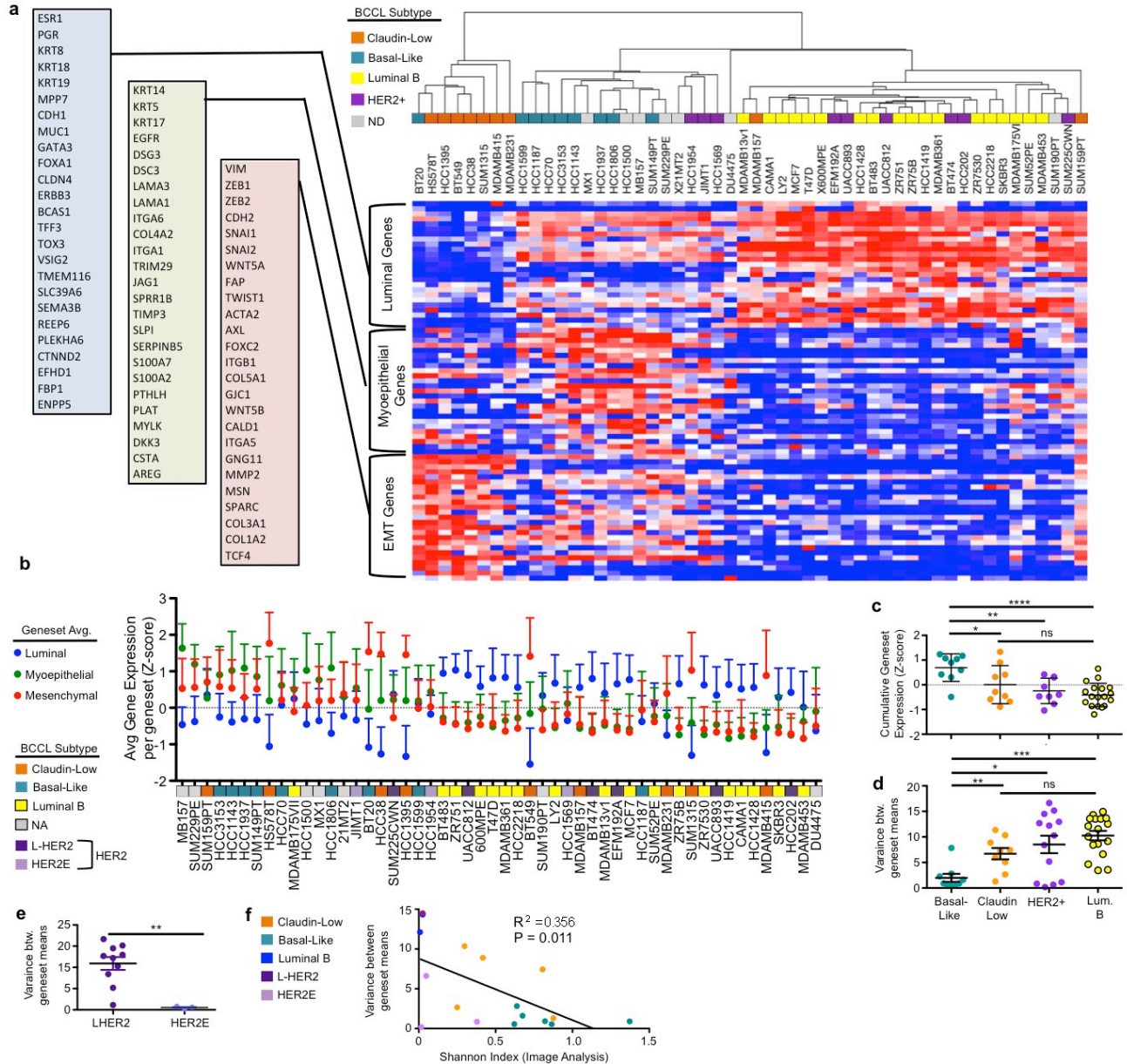


**Figure 2-3: Heterogeneity in luminal, basal, and mesenchymal geneset expression correlates with image based cell-state heterogeneity metrics.**

(A) Heatmap of BCCL gene expression of 20 luminal, 20 myoepithelial, and 20 EMT-correlated genes. BCCLs are arranged by unsupervised clustering. Cell line molecular subtype is denoted by color: orange, claudin-low; cyan, basal-like; yellow, luminal B; purple, HER2+, grey, not determined. (B) Graph of the mean normalized gene expression value (Z-score) of the luminal (L,

blue), basal (B, green), and mesenchymal (M, red) genesets are displayed in each cell line with standard deviation of expression. Cell lines are arranged in descending order (left to right) according to the mean Z-score of all genesets. Cell line subtype is denoted by color as in **B**. **(C)** Graph of the cumulative Z-score of the luminal, myoepithelial, and EMT genesets in BCCLs of different molecular subtype, \*P < 0.05, \*\*P < 0.01, \*\*\*\*P < 0.0001, ns = not significant, SEM shown. **(D)** Graph of the variance between the mean geneset expression of the luminal, myoepithelial, and EMT genesets in BCCLs of different molecular subtype, asterisks denote significant difference in geneset variance \*P < 0.05, \*\*P < 0.01, \*\*\*P < 0.001, ns = not significant, SEM shown. **(E)** Graph of the variance between HER2+ cell lines that are either of the L-HER2 or HER2E molecular subtypes. Asterisks denote significant difference in geneset variance \*\*P < 0.01. **(F)** A scatterplot comparing BCCL Shannon diversity index presented in Fig. 2d to the variance between basal, luminal and mesenchymal genesets presented in **D**. A linear regression with significantly non-zero slope P = 0.011 is shown on the graph.

## 2.4 Discussion

In this study we develop an operational metric of cell-state heterogeneity based on the expression of luminal, basal, and mesenchymal differentiation-state markers. These markers are preferentially expressed in normal differentiation states in the breast and additionally mark non-uniformities in tumor cell differentiation within breast tumors<sup>38,72,150</sup>. We used 4-color immunofluorescent imaging, single-cell segmentation, and cytometry software to calculate the frequency of distinct differentiation-states in each tumor. As a metric of heterogeneity of these states, we employed the Shannon Diversity index, which was initially developed by Claude Shannon in the 1960s in order to calculate the entropy, or diversity, of a system with multiple species<sup>139</sup>. This equation has been successfully used to measure species diversity in bacteria<sup>151</sup>, animals species<sup>152</sup>, and recently, in tumor states. Using our image analysis pipeline we are able to demonstrate that differentiation-state heterogeneity is not evenly distributed in the breast cancer patient population, with luminal (ER+/PR+/HER2-)

tumors showing low levels of differentiation-state heterogeneity, being near-homogenously composed of tumor cells in a luminal cell state expressing K19, whereas HER2+/ER- tumors had higher heterogeneity due to the common existence of a K19+/K14+ subpopulation, and triple negative tumors having the highest levels of heterogeneity, harboring tumor cells that are positive for K19, K14, VIM, and combinations of these markers.

Analysis of the breast cancer cell lines supported our conclusions from primary patient samples, showing enriched levels of differentiation-state heterogeneity in the triple negative and basal-like subtypes. Further, the cell lines gave us an opportunity to examine the relationship between transcriptional heterogeneity in differentiation marker expression, and heterogeneity in differentiation marker expression measured by immunofluorescence (IF). We found that variance between the mean-expression of the luminal, basal, and mesenchymal genesets significantly correlated with the Shannon diversity index calculated from our imaging assays. This gene expression based metric may be a useful tool to validate heterogeneity observed in imaging assays, or serve as a surrogate in cases where tumor sections are not available. Interestingly, this variance metric proved particularly useful at distinguishing the L-HER2 and HER2E molecular subtypes of HER2+ breast cancer. Where L-HER2 lines showed significantly higher variance, and HER2E lines having very low variance in gene expression between luminal, basal, and mesenchymal genesets. This geneset variance metric may prove useful to separate these subtypes clinically, or retrospectively in

gene expression studies of patients tumors where L-HER2 / HER2E separation might reveal meaningful findings.

Taken together, the analysis systems and results presented here lay a foundation to improve upon for the quantitation of intratumoral phenotypic heterogeneity. As we continue to better understand the relationships between cell state heterogeneity, cell state plasticity, tumor behavior, and therapeutic resistance, these methods will become increasingly important for the optimal diagnosis and treatment of breast cancer patients.

### **3 Managing drug-induced differentiation-state plasticity in basal-like breast cancer to improve therapeutic control**

Tyler Risom, Ellen M. Langer, Margaret P. Chapman, Juha Rantala, Mariano J. Alvarez, Andrew Fields, Nicholas D. Kendsersky, Carl R. Pelz, Katherine Johnson-Camacho, Lacy Dobrolecki, Koei Chin, Anil J Aswani, Nicholas J Wang, Paul Spellman, Andrea Califano, Mike Lewis, Claire J. Tomlin, Andrew Adey, Joe W. Gray, Rosalie C. Sears

The data presented in this chapter are taken from a manuscript titled “Measuring and Managing Cell State Plasticity in Basal-Like Breast Cancer to Improve Therapeutic Control”, which is in review at Nature Communications. I designed the experimental approach in this manuscript with Juha Rantala, Joe Gray, and Rosalie Sears. I performed the majority of experiments with the exception the following collaborative work: drug screen heterogeneity measurements were performed with Juha Rantala, cell state mathematical modeling with Margaret Chapman and Claire Tomlin, VIPER analysis of RNAseq data with Mariano Alvarez and Andrea Califano, and sciATACseq with Andrew Fields and Andrew Adey. With exception to collaborative work, I analyzed all of the data and produced all final figures for publication. I wrote the manuscript with feedback and editing from the other authors.

### 3.1 Abstract

Intratumoral heterogeneity in cancers arises from genomic instability and epigenomic plasticity and is associated with poor therapeutic control using cytotoxic and targeted therapies. We show here that cell-state heterogeneity defined by expression of differentiation-state markers is high in triple-negative and basal-like breast cancer subtypes, and that drug tolerant persister (DTP) cell populations with altered differentiation-state marker expression emerge during treatment with a wide range of pathway-targeted therapeutic compounds. Our findings indicate that the DTP states arise through cell-state transition, rather than by Darwinian selection of preexisting drug-resistant subpopulations, and these transitions involve dynamic remodeling of the open chromatin architecture. Increased activity of a number of chromatin modifier enzymes was observed in DTP cells, including upregulation of the BRD4 network. Consistent with this, we show that co-treatment with the PI3K/mTOR inhibitor BEZ235 and the BET inhibitor JQ1 prevented changes to the open chromatin architecture and inhibited the acquisition of a DTP state, resulting in ubiquitous cell death in vitro and tumour xenograft regression in vivo.

## 3.2 Introduction

The mammary gland contains a diverse repertoire of epithelial cell states that rely on chromatin dynamics for specification<sup>103,153</sup>. Throughout development these states include distinct fetal and adult stem cell states, lineage-restricted luminal and myoepithelial progenitors, mature luminal and myoepithelial states, and mesenchymal-transitioned cells<sup>51,95,118,146,148</sup>. While DNA methylation plays a predominant role in early lineage distinction in the maturing embryo<sup>100</sup>, cell differentiation from stem cell states in the adult is primarily carried out through dynamic changes in histone modifications at promoters and distal regulatory elements<sup>102-104</sup>, altering the open chromatin architecture and providing enhanced expression of new lineage and differentiation genes<sup>154,155</sup>. These chromatin dynamics are critical for the specialized cell state heterogeneity that maintains normal mammary gland function.

Tumors that arise from the complex epithelial compartment of the mammary gland are also phenotypically diverse. Breast tumors can evolve to represent numerous molecular subtypes that share similarities with normal mammary cell states<sup>41,51,118</sup>. Many breast tumors also display intratumoral phenotypic heterogeneity<sup>22,63,72,116</sup> and are populated with tumor cells in functionally distinct cell states. Different cell states can possess distinct drug sensitivities<sup>5,13,22,23,121</sup>, making cell-state heterogeneity a challenge for therapeutic management of breast tumors.

An additional challenge, which may be even harder to address, is the inherent plasticity of tumor cell states<sup>93,156,157</sup>. Cytotoxic and targeted therapies have been shown to trigger the transition to drug-tolerant persister (DTP) cell states that can survive under drug pressure at a low-proliferative state<sup>24,25,121</sup>, leading to incomplete responses to therapy and/or recurrence. Recent findings demonstrate that dynamic chromatin remodeling processes, similar to those employed in normal cell fate determination, can underlie these transitions to drug-tolerant states<sup>24,70,158</sup>. While it is well established that evasion of therapeutic control can occur through Darwinian selection of genetically diverse cellular subpopulations<sup>19,159</sup>, mounting evidence implicates dynamic chromatin remodeling as an equally important driver of therapeutic tolerance, which must be addressed to improve clinical outcomes. Understanding, therefore, which breast tumor subtypes have high cell state heterogeneity and propensity for cell-state plasticity, whether specific therapeutics trigger DTP transitions, and what targetable epigenomic processes underlie these transitions will be critical steps to improving our management of heterogeneous breast tumors.

Here we use models of phenotypically heterogeneous breast cancers to investigate how cell-state heterogeneity and plasticity contribute to the generation of drug-tolerant persister states. We identify multiple classes of targeted therapeutics that steer initially heterogeneous cell populations to more homogeneous, but drug-tolerant persister states, and use gene expression profiling to identify upregulated signaling and epigenetic pathway activity in the DTP states. This strategy identified the upregulation of BRD4 activity in the DTPs generated

from MEK and PI3K/mTOR targeted therapies. We demonstrate that inhibition of the bromodomain and extraterminal (BET) family of proteins by JQ1 can prevent the global change in open chromatin architecture that accompanies DTP state formation during PI3K/mTOR inhibitor response, and moreover, combination of PI3K/mTOR and BET inhibitors drives complete cell kill of basal-like breast cancer cell lines *in vitro*, and tumor regression of orthotopic xenografts *in vivo*. Our study demonstrates that triple negative (TN) and basal-like breast cancers show high cell-state heterogeneity and plasticity, and advances our understanding of how drug combinations targeting chromatin dynamics can improve our ability to manage these aggressive subtypes of breast cancer.

### **3.3 Results**

#### **3.3.1 Targeted therapies generate distinct drug-tolerant persister states**

Differentiation-state heterogeneity is enriched in the triple negative and basal-like subtypes of breast cancer, where cells coexists in distinct differentiation states defined by basal, luminal and mesenchymal marker expression (Chapter 2)<sup>67</sup>. We investigated the impact of high differentiation-state heterogeneity in basal-like, triple-negative breast cancers towards response to targeted therapy. We used high-content imaging to assess changes in cell number as well as K19, K14, and VIM expression in the heterogeneous basal-like cell lines HCC1143 and SUM149PT following a 72hr treatment with 119 pathway-targeted therapeutic

compounds, examining 7-doses of each compound (Fig. 3-1a). Most drugs had incomplete cytotoxicity at max doses and altered differentiation-state marker expression in the remaining cell populations. We used K-means clustering to identify compounds for which DTPs exhibited similar patterns of K19/K14/VIM expression. Figure 2a shows six general response groups in HCC1143 where compounds produced drug-tolerant populations with: (A) increased K14 expression, (B) increased K19 and VIM expression, (C) increased expression of all markers at high dose, (D) increased expression of all markers across doses, (E) minimal change in marker expression, or (F) variable, non-dose-dependent response. Importantly, compounds with the same molecular target or related pathway targets clustered together. For example, inhibitors targeting MEK and BRAF grouped together within the K14-enriched cluster (Group A), inhibitors targeting mTOR and PI3K grouped within the K19/VIM-enriched cluster (Group B), inhibitors targeting the ErbB receptors, Src family kinases, or Aurora kinases enriched all markers (Groups C and D), and inhibitors of Flt3 and other related receptor-tyrosine-kinase families had minimal influence on cell proliferation or differentiation-marker expression, likely due to the lack of reliance of breast cancer cells on these kinases (Group E). A similar array of phenotypic responses was observed in SUM149PT following screening, and drug targets clustered into similar groups as HCC1143 (Fig. 3-S1).

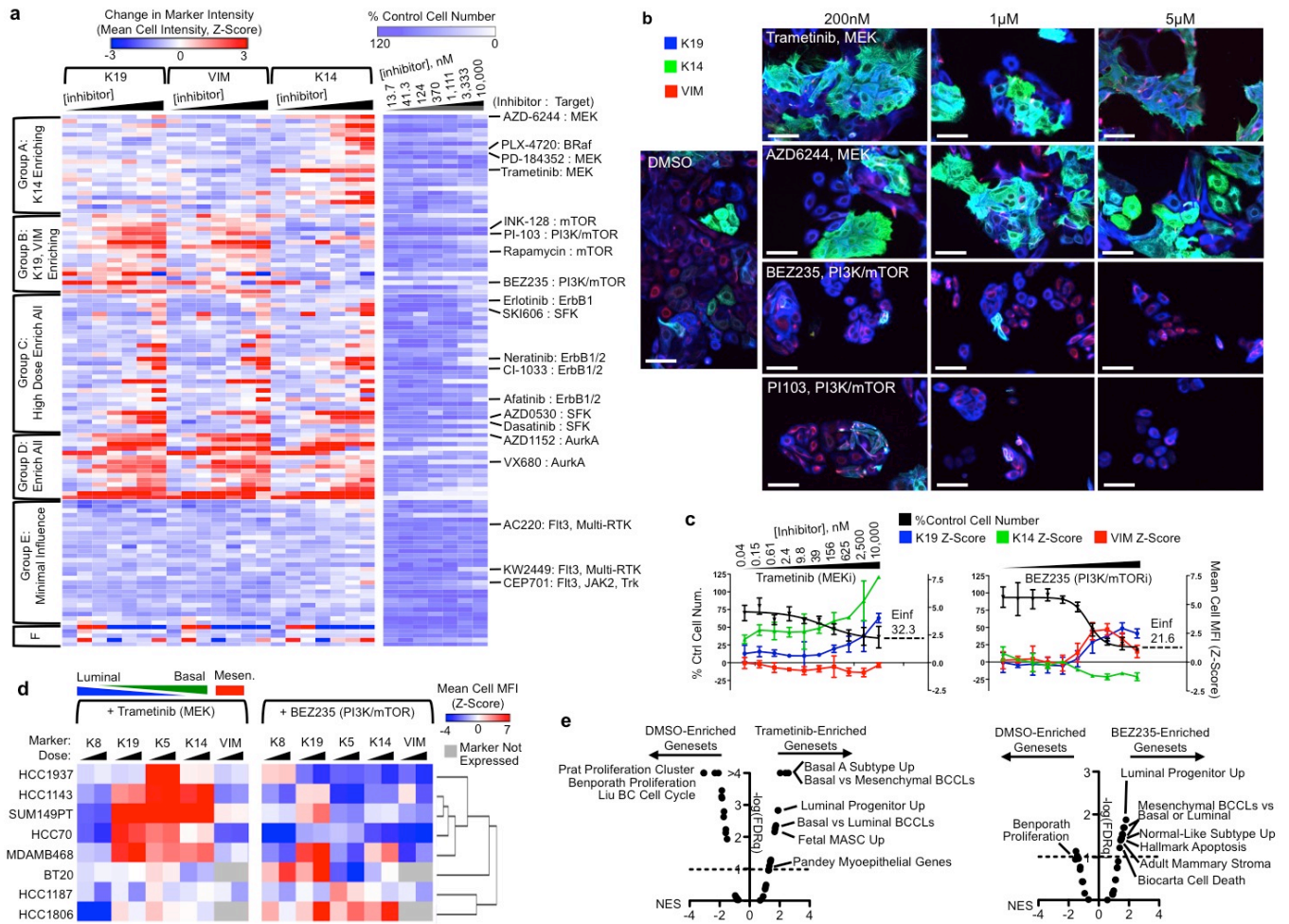


**Figure 3-1: Targeted therapies enrich distinct drug-persisting differentiation states.**

(A) Heatmaps show the change in K19, VIM, and K14 expression compared to DMSO control wells as a Z-score (left), and change in proliferation (right, percent of control) of HCC1143 cells following 72hr exposure to 7 doses of 119 targeted therapeutics. Phenotypic responses were clustered using K=6 supervised K-means clustering. Select drugs from each cluster and their primary therapeutics target(s) are labeled to the right. (B) IF images of HCC1143 cells following 72hr treatment with increasing doses of MEK inhibitors Trametinib and AZD6244 and the PI3K/mTOR inhibitors BEZ235 and PI103, or a DMSO control, showing K19 (blue), K14 (green) and VIM (red), scale bars = 100µm. (C) Graphs of therapy-induced changes in cell number and mean-cell MFI of K19 (blue, right axis, as Z-score), VIM (red), and K14 (green), in HCC1143 cells following 72hr incubation with increasing doses of the MEK inhibitor Trametinib, or PI3K/mTOR inhibitor BEZ235. The projected maximum level of inhibition, or Einf, is shown for each drug. (D) Heatmaps of the change in mean-cell MFI (Z-Score) for K8, K19, K5, K14 and VIM is shown for 8 basal-like BCCLs following 72hr incubation with 250nM or 2500nM of Trametinib (left) or BEZ235 (right).

Unsupervised clustering, using data from both agents, was used to group cell lines based on phenotypic response. **(E)** GSEA results as a volcano plot of Normalized Enrichment score (NES, x-axis) vs. FDRq (-log, y-axis) examining 32 genesets related to mammary cell states and breast cancer subtypes, enrichment compared between DMSO and 1 $\mu$ M Trametinib (left), or DMSO and 1 $\mu$ M BEZ235 (right) in HCC1143 cells treated for 6d. Select top-enriched genesets are labeled.

We analyzed compounds associated with the K14-enriched and K19/VIM-enriched groups in more detail since these left cells in substantially different aggregated states of differentiation-marker expression. We evaluated responses of HCC1143 cells after 72hr treatment with escalating doses of two MEK inhibitors, Trametinib and AZD6244 (K14-enriched cluster, A), and two dual-specificity PI3K/mTOR inhibitors, BEZ235 and PI103 (K19/VIM-enriched cluster, B). As observed in the drug screen, these agents left sizeable DTP populations that had distinct differentiation marker expression. The MEK inhibitors produced DTP cells with large cytoplasmic volume and high expression of K19 and K14, and reduced cellular VIM levels (Fig. 3-1b). Conversely, the PI3K/mTOR inhibitors reduced K14 expression, and produced distinct DTP cells with high K19 and VIM expression. These divergent effects of MEK and PI3K/mTOR inhibition on DTP differentiation-state were also observed in SUM149PT cells, and with additional basal markers including Cytokeratin 5 (K5) and Cytokeratin 17 (K17), and luminal marker Cytokeratin 8 (K8, Fig. 3-2). We measured the effects of MEK and PI3K/mTOR inhibitors on cell viability and differentiation-state identity across larger dose ranges and found that both inhibitors produced large DTP populations indicated by high projected maximal inhibition “Einf” values, and an observable

plateau in the dose response curve (Fig. 3-1c, Fig. 3-3a). These analyses also showed that MEK inhibition drove increases in cellular mean-fluorescent intensities (MFI) of K14 and K19, and reductions in VIM, while PI3K/mTOR inhibitors caused mean cell MFI reductions in K14 and increases in K19 and VIM. To determine the conservation of these phenotypic responses to therapy we assayed an expanded set of basal-like cell lines with diverse genetic backgrounds and different baseline differentiation-state heterogeneities (see Ch. 2). We measured the change in mean-cell MFI of K8, K19, K14, K5 and VIM in eight basal-like BCCLs treated with low and high dose of Trametinib and BEZ235 (Fig. 3-1d). Unsupervised clustering of phenotypic responses to these agents showed that the majority of these basal-like lines shared a similar phenotypic response: Trametinib enriched a K19/K5/K14-high basoluminal state with lower K8 and VIM levels, and BEZ235 enriched a state marked by low basal cytokeratin expression and increased levels of K19 expression in most lines, and K8 in HCC1937. Assessment of the phenotypic response to these drugs in luminal-B and claudin-low cell lines showed that Trametinib and BEZ235 affect cell proliferation, but the cells remain in their respective  $K19^+/K14^-/VIM^-$  and  $K19^-/K14^-/VIM^+$  differentiation states following treatment (Fig. 3-3b).

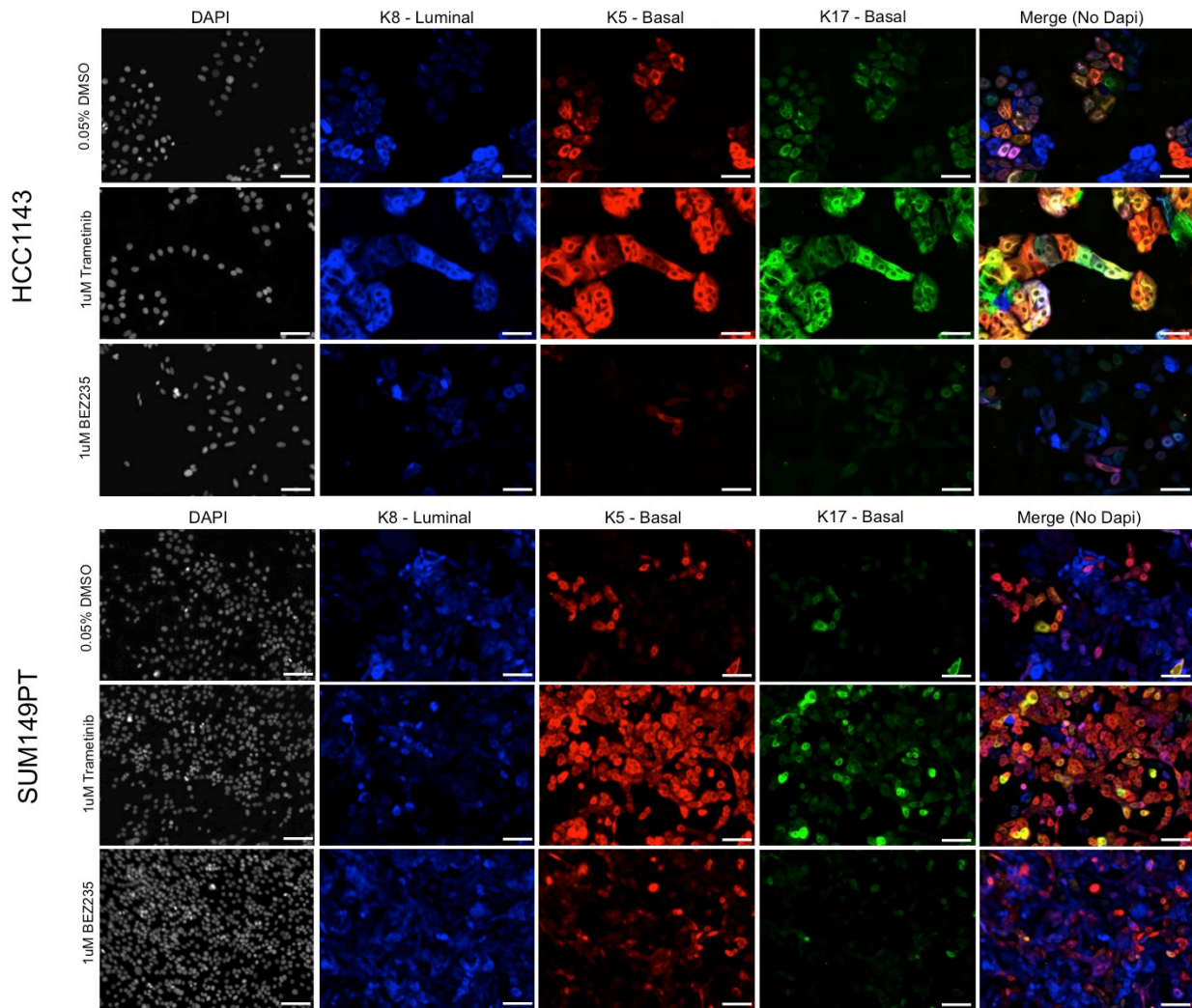


**Figure 3-2: MEK and PI3K/mTOR inhibitors have opposing influence on basal differentiation in drug-persisting cells**

Images of HCC1143 and SUM149PT under DMSO control conditions or following 72hr of 1μM Trametinib or 1μM BEZ235, showing DAPI, K8, K5, K17 and a 4-color merged image, scale bars = 100μm

To confirm that the differentiation-state enrichments following MEK or PI3K/mTOR inhibitors were altering broader gene programs, and not just the expression of our cytokeratin marker sets, we performed RNA-sequencing and subsequent Geneset Enrichment Analysis (GSEA) on treated cell populations testing for enrichment of 32 curated genesets from the molecular signature database<sup>160</sup> and additional studies relating to normal breast cell states<sup>98,103,141</sup>, breast cancer subtypes<sup>33,38,161,162</sup>, and breast cancer proliferation<sup>38,163</sup>. Consistent with the increased basal cytokeratin expression observed by IF following Trametinib treatment, we observed significant enrichment of genesets specific to the Basal A subtype of breast cancer<sup>161</sup>, basal BCCLs<sup>162</sup>, and myoepithelial cells of the normal breast<sup>141</sup> (Fig. 3-1e, Fig. 3-3c). We also observed enrichment of genesets specific to human luminal progenitor cells and murine fetal mammary stem cells, two related progenitor/stem states<sup>98</sup> that show dual expression of basal and luminal markers<sup>51,95</sup>, consistent with the enrichment of the K19<sup>hi</sup>/K14<sup>hi</sup> differentiation-state following Trametinib. Consistent with the reduction of basal cytokeratin expression, and the mixed luminal/mesenchymal markers in BEZ235 DTPs, we observed enrichment of genesets relating to luminal progenitors<sup>98</sup>, mesenchymal BCCLs<sup>162</sup>, the normal-like subtype of breast cancer<sup>33</sup>, and adult mammary stroma<sup>98</sup> (Fig. 3-1e, 3-3d). Finally, consistent with the reduced proliferation following treatment with these drugs, both treatments induced significant de-enrichment of proliferation genesets, and BEZ235 treatment resulted in enrichment of apoptosis and cell death genesets (Fig. 3-1e, 3-3c, d).

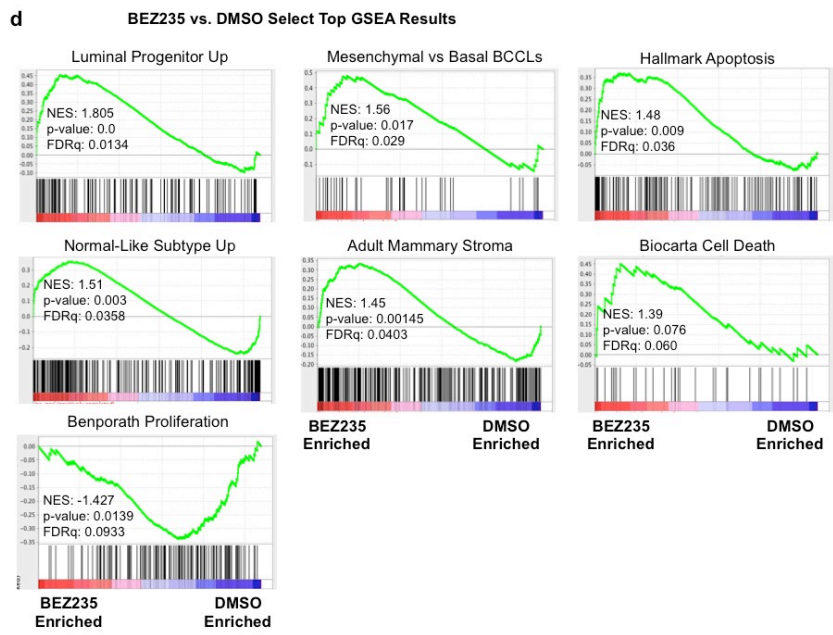
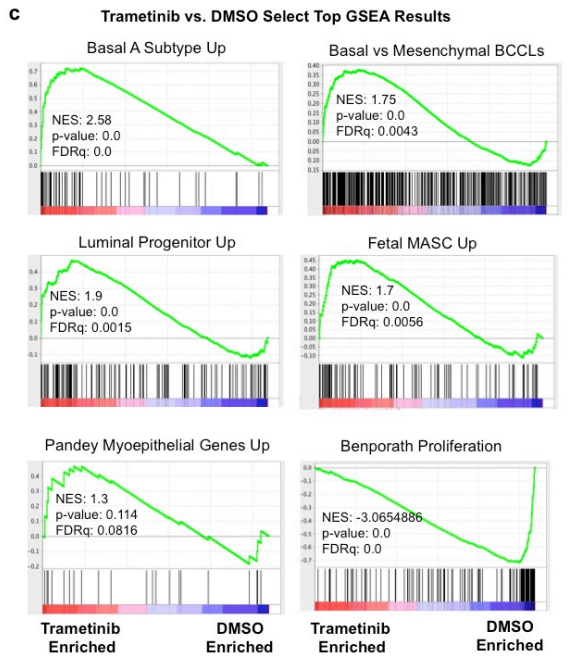
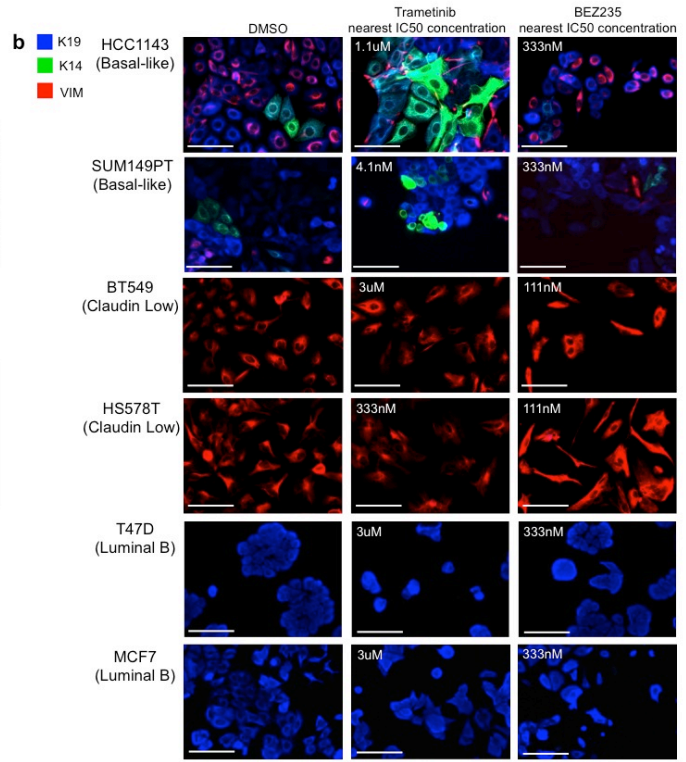
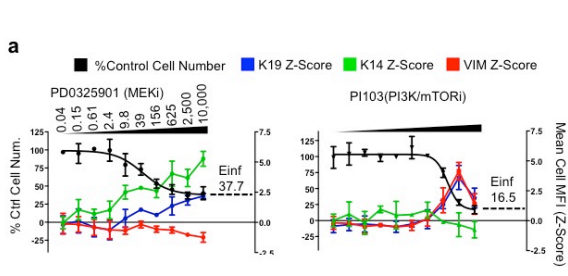


### Figure 3-3: MEK and PI3K/mTOR enrich distinct DTP differentiation-states in basal-like cell lines

**(A)** Graphs of therapy-induced changes in cell number and mean-cell MFI of K19 (blue, right axis, as Z-score), VIM (red), and K14 (green), in HCC1143 cells following 72hr incubation with increasing doses of the MEK inhibitor PD0325901, or PI3K/mTOR inhibitor PI103. The projected maximum level of inhibition, or Einf, is shown for each drug. **(B)** Images of two basal-like cell lines (HCC1143 and SUM149PT), two Claudin-low lines (BT549 and HS578T), or two Luminal B cell lines (T47D and MCF7) following 72h treatment with the nearest-to-IC50 dose of Trametinib, BEZ235, or DMSO, dose displayed on image. K19 (blue), VIM (red), and K14 (green) shown, scale bars = 100 $\mu$ m. **(C)** Select top-enriched genesets are shown for 6day Trametinib treated HCC1143 cells vs. DMSO with Normalized Enrichment Score (NES), Nominal P-value (p-value), and FDR q-value (FDRq) shown. **(D)** Select top-enriched genesets are shown for 6day BEZ235 treated HCC1143 cells vs. DMSO

#### 3.3.2 Cell state dynamics during therapy

We next explored the dynamics of therapy-induced differentiation-state changes and the roles of state-selective proliferation, state-selective cell death, and cell-state transition in the phenotypic response to targeted therapy. We defined four prominent, drug-induced differentiation-states as 1) cells that expressed high levels of K14, “K14<sup>hi</sup>”, 2) cells that express high levels of VIM and low levels of K14, “VIM<sup>hi</sup>”, 3) cells that express high levels of only K19 and low levels of K14 and VIM, “K19<sup>hi</sup>”, and 4) cells that express low levels of all markers, “K19<sup>low</sup>/VIM<sup>low</sup>/K14<sup>low</sup>” (with “high” defined as a cell with MFI exceeding the average MFI in DMSO wells and “low” being values below the DMSO average). We measured the frequency of these states over time following treatment with 1 $\mu$ M Trametinib or 1 $\mu$ M BEZ235 in HCC1143 cells. Trametinib induced a significant increase in the

frequency of the K14<sup>hi</sup> state while significantly reducing the frequency of the other three states over time (Fig. 3-4a). Conversely, BEZ235 induced a significant increase in the K19<sup>hi</sup> state and a robust reduction of the K14<sup>hi</sup> state over time. We reasoned that differential growth between K14<sup>hi</sup> and K14<sup>low</sup> states under drug pressure might explain the observed state enrichments, and tested this possibility by pulsing 5-ethynyl-2'-deoxyuridine (EdU) 12-hours prior to fixation of each 12-hr timepoint in order to mark cells that have recently transitioned through S-phase. Both drugs had a strong cytostatic influence, reducing the rate of EdU incorporation to near zero levels with Trametinib, and reduced to a third-of-control levels with BEZ235 (Fig 3-4b). Cells remained in this low proliferative state as long as drug pressure was maintained (tested to 21 days, Fig. 3-5b). Importantly, no significant differences in S-phase frequency were observed between cells expressing high or low levels of K14, K19, or VIM, except for one timepoint with Trametinib treatment where VIM<sup>hi</sup> and VIM<sup>low</sup> EdU rates differed, which we attributed to noise (Fig. 3-4b, c). Mass cytometry experiments supported these observations, showing minimal differences in IdU incorporation frequency between cells expressing high and low values of luminal and basal markers following Trametinib or BEZ235 (Fig. 3-5c-e). In light of these results suggesting that all differentiation-states share a similar cytostatic response to each therapy, we investigated whether differential cell death rates may enable the differentiation-state enrichments following Trametinib or BEZ235 treatments. We examined the rates of total cell death throughout the 72hr treatment by measuring positivity for the membrane impermeable fluorescent dye YO-PRO-1 and found that BEZ235 induced significant gains in cell death at

36hr onwards, and Trametinib only showed significant gains in cell death compared to control at 48 and 72hr (Fig. 3-4d). Notably, these significant gains in cell death occurred after significant changes in differentiation-state frequencies were found, which started at 12hr of treatment (see Fig. 3-4a). We were limited in our ability to examine state-specific cell death due to non-specific antibody staining in dying cells and the loss of adherent-cell morphology. As an alternative approach, we tested the necessity of cell death for the observed phenotypic outcomes by combining Trametinib or BEZ235 with Z-VAD-FMK, an inhibitor of caspase-mediated cell death. Z-VAD-FMK treatment significantly reduced cell death in the DMSO control condition and reduced cell death in Trametinib treated cells by 82% and BEZ235-treated cells by 71% when combined (Fig. 3-4e) Despite this, drug-induced differentiation-state composition at 72hr was nearly identical to wells treated with Trametinib or BEZ235 alone (Fig. 3-4f). These results argue against a dominant role for state-selective cytostasis or cytotoxicity and suggest cell-state transition is the likely driver of differentiation-state enrichment following Trametinib and BEZ235.

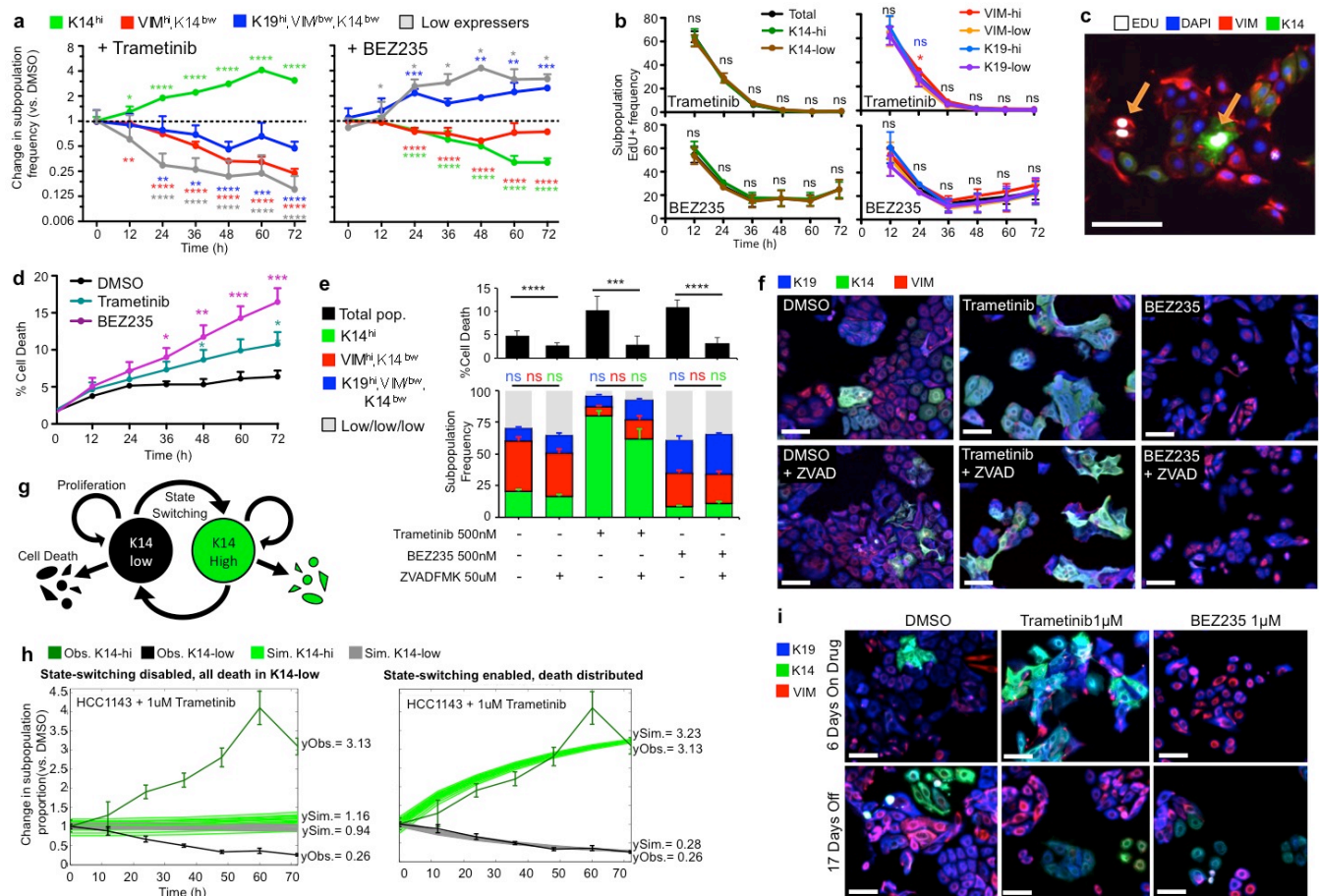


**Figure 3-4: Cell state transitions underlie DTP-state enrichment.**

**(A)** Graphs show the change in frequency (vs DMSO) of four differentiation states defined as K14<sup>hi</sup> (green), VIM<sup>hi</sup>/K14<sup>low</sup> (red), K19<sup>hi</sup>/VIM<sup>low</sup>/K14<sup>low</sup> (blue), and K19<sup>low</sup>/VIM<sup>low</sup>/K14<sup>low</sup> (grey) following exposure to 1μM Trametinib or 1μM BEZ235. Asterisks depict significant gains or losses in state frequency vs. 0hr, \*P < 0.05, \*\*P < 0.01, \*\*\*P < 0.001, \*\*\*\*P < 0.001, n=15 with SD.

**(B)** Graphs showing the percent of EdU+ cells expressing high or low levels of K14, K19, or VIM following treatment with 1μM Trametinib or BEZ235, \*P < 0.05, ns = not significant, SEM shown.

**(C)** IF image showing both K14<sup>hi</sup> and K14<sup>low</sup> cells positive for EdU-incorporation following 36hr of Trametinib treatment, with EdU (white), DAPI (blue), K14 (green), and VIM (red) shown, scale bar = 100μm.

**(D)** Graph showing the percent of dying cells (YO-PRO-1+) following treatment with 1μM Trametinib or BEZ235. Asterisks denote significant differences compared to DMSO control, \*P < 0.05, n=8 with SEM.

**(E)** Graphs show the percent of dying cells (YO-PRO1+), and the frequency of cells of four differentiation states (as in a) following 72hr exposure to 500nM Trametinib, 500nM BEZ235, or DMSO +/- the pan-caspase inhibitor Z-VAD-FMK (50μM). \*\*\*P

$\leq 0.001$ , \*\*\*\* $P \leq 0.0001$ . No significant (ns) differences in differentiation-state frequency were observed +/- Z-VAD-FMK, color denoting differentiation state (as in **a**),  $n=12$  with SD. **(F)** Corresponding IF images of remaining HCC1143 cells in **e** following 72hr exposure to Trametinib, BEZ235 or DMSO +/- Z-VAD-FMK. K19 (blue), K14 (green), and VIM (red), DAPI not shown, scale bars = 100 $\mu\text{m}$ . **(G)** A schematic describing a computational model of cell-state behavior where cells can transition between a  $K14^{\text{hi}}$  and a  $K14^{\text{low}}$  cell state, undergo death in either state, or proliferate in either state. **(H)** Simulated fold change of  $K14^{\text{hi}}$  (bright green) and  $K14^{\text{low}}$  (grey) cell-state proportions over 72 hours following treatment with 1 $\mu\text{M}$  Trametinib (vs. DMSO) with average endpoint values denoted as  $y_{\text{Sim}}$ . Simulations were generated from 15 replicate initial conditions using models of HCC1143 cell population dynamics, identified to test two potential drivers of differentiation-state enrichment.  *$K14^{\text{hi}}$  Darwinian selection* (left): Trametinib kills only  $K14^{\text{low}}$  cells, and cell-state transition is inhibited. *Transition-mediated* (right): Trametinib kills  $K14^{\text{low}}$  and  $K14^{\text{hi}}$  cells in equal proportions, and cell-state transition is allowed. Experimentally observed average fold change (vs DMSO) of  $K14^{\text{hi}}$  (dark green) and  $K14^{\text{low}}$  (black) cell-state proportions is overlaid with endpoint values denoted  $y_{\text{Obs}}$ . **(I)** IF images of HCC1143 cells following 6 days of 1 $\mu\text{M}$  Trametinib or 1 $\mu\text{M}$  BEZ235, then following 17 days of culture without drug. K19 (blue), K14 (green) and VIM (red), scale bars = 100 $\mu\text{m}$ .

To further evaluate the influence of state-selective death or cell-state transitions on drug-induced differentiation-state enrichment, we designed a computational tool that utilized our timecourse data to identify a cell-state dynamical model of proliferation, death, or transition between  $K14^{\text{hi}}$  and  $K14^{\text{low}}$  states (Fig. 3-4g). By comparing our data to model predictions under special constraints, for example with state-specific cell death, we tested if  $K14^{\text{hi}}$  Darwinian selection or cell-state transition were more influential in Trametinib-induced differentiation-state enrichment. For all trials, cell-state proliferation rates were set equal since we had measured that directly with our EdU+ analysis (Fig. 3-4b). For a baseline, cell death measured following DMSO treatment was allocated evenly between  $K14^{\text{high}}$  and  $K14^{\text{low}}$  states. To test the hypothesis of state-specific selection of  $K14^{\text{hi}}$  cells, we allocated cell

death following Trametinib entirely to the  $K14^{low}$  state, and cell-state transition was disallowed. Conversely, to test the transition-mediated hypothesis, cell death following Trametinib was allocated evenly between  $K14^{high}$  and  $K14^{low}$  states and cell-state transition was permitted. Under the Darwinian selection hypothesis, computational simulations predicted very little divergence between  $K14^{hi}$  and  $K14^{low}$  subpopulations over time, which was inconsistent with our experimental observations (Fig. 3-4h, left). However, under the alternative hypothesis in which cell-state transitions were enabled, simulated Trametinib-induced dynamics of HCC1143 cells predicted differentiation-state enrichment similar to the experimental observations (Fig. 3-4h, right). The transition-mediated hypothesis also recapitulated closer to observed  $K14^{hi}$  and  $K14^{low}$  values in simulations of BEZ235 response (Fig. 3-5f). Together, these data implicate cell state transition as the driver of DTP-state aggregation following Trametinib and BEZ235. Finally, if the enrichment of specific cell states occurred through state transitions, we would expect that these therapy-induced states would be reversible and cells would return to heterogeneity following withdrawal of the drugs. Indeed, we observed that cells moved back to control-levels of heterogeneity within 17 days of drug withdrawal, and regained their pre-treatment sensitivity to BEZ235 and Trametinib, supporting once again a transition-mediated mechanism (Fig. 3-4i, Fig. 3-5g-i).

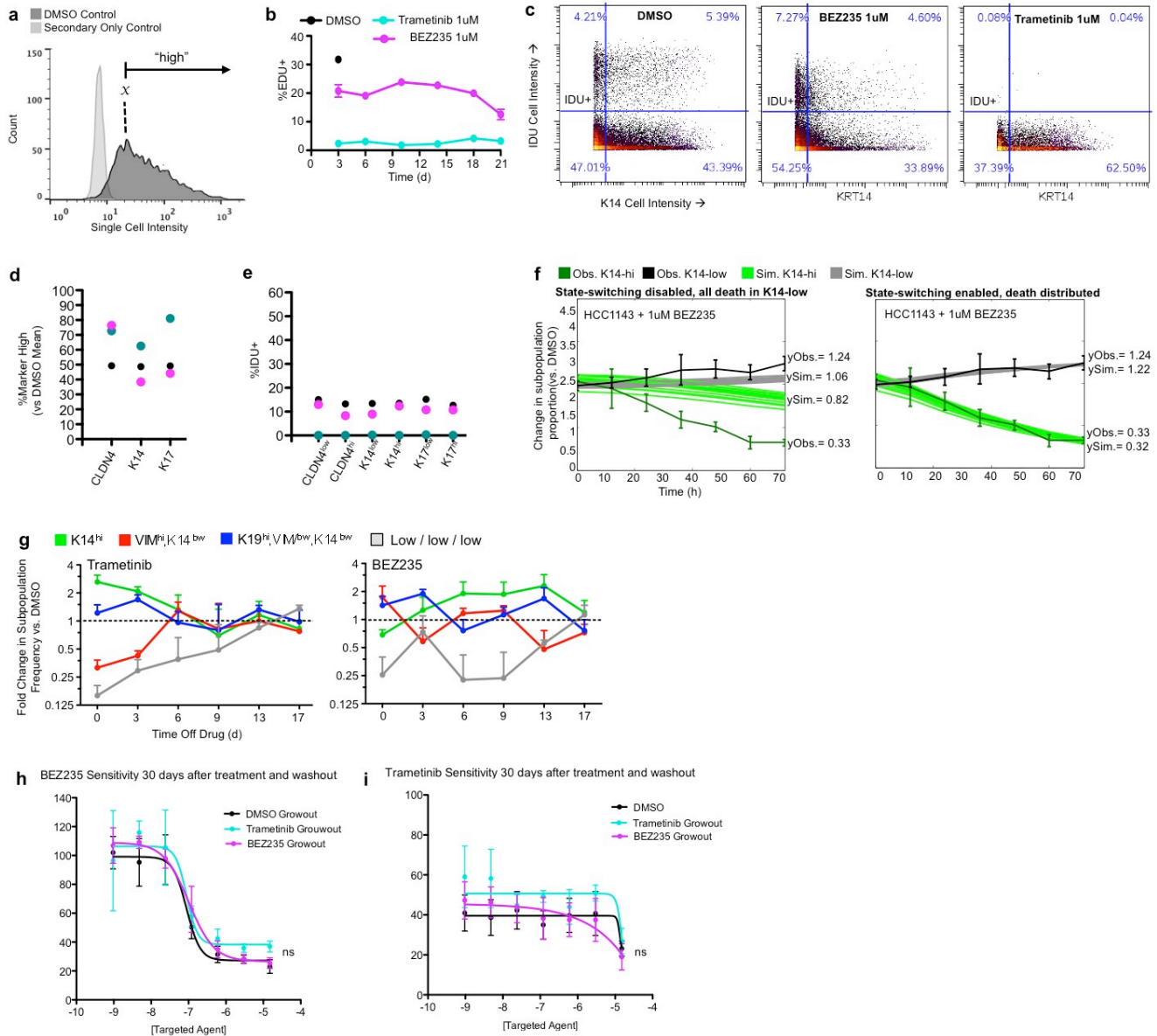


**Figure 3-5: Further examination of DTP cell kinetics following Trametinib and BEZ235.**

(A) Schematic showing how high expression of a given marker is determined from DMSO population values. (B) Graph showing EdU incorporation rates in HCC1143 cells every 3-4 days while being maintained on 1 $\mu$ M Trametinib or 1 $\mu$ M BEZ235 for 21 days, with the incorporation rate of DMSO shown for the first 3 days of growth. (C) Dot plots showing mass cytometry results comparing single cell IdU and K14 levels following 72hr of 1 $\mu$ M Trametinib, 1 $\mu$ M BEZ235, or a

DMSO control. **(D)** Graph showing the percent of cells expressing high levels of the luminal marker CLDN4, basal markers K14 and K17, or mesenchymal marker VIM following 72hr of 1 $\mu$ M Trametinib or BEZ235, measured by mass cytometry. **(E)** Graph showing the frequency of IdU+ cells in cells also expressing high and low values of CLDN4, K14, K17, and VIM from d. **(F)** Simulated fold change of 1 $\mu$ M BEZ235-treated HCC1143 cells vs. DMSO using the model presented in Fig. 3g with two separate hypotheses: K14<sup>low</sup> Darwinian selection (left) where all cell death occurs in K14<sup>hi</sup> cells and cells cannot transition between states, cell-state transition (right) where cell death is distributed evenly between states and cells can transition between states. Observed and simulated values at 72hr are shown to the right of both plots. **(G)** Graph showing the cell state composition of 4 differentiation states vs. DMSO, as in Figure 3a, following 72hr of 1 $\mu$ M Trametinib or 1 $\mu$ M BEZ235 treatment then drug washout, examining cell state composition every 3-4 days for 17 days, n=4 with SD. **(H)** Dose response curves showing sensitivity to BEZ235 in untreated cells, or cells treated with Trametinib or BEZ235 then recovered from drug washout for 30 days. ns = not significant, full dose response compared using two-way ANOVA, examining 'interaction'. **(I)** Same as in **h** examining sensitivity to Trametinib in untreated or inhibitor-recovered cells.

### 3.3.3 Drug combinations reduce therapeutic escape

We sought to take advantage of the aggregation of DTP cell identity following BEZ235 and Trametinib treatment with the hypothesis that these enriched states may more heavily rely on specific pathways for survival. We identified upregulated pathways by measuring gene expression profiles in DTP cells after 6 days of treatment with Trametinib or BEZ235 through RNA-seq and used the Virtual Inference of Protein-activity by Enriched Regulon (VIPER) algorithm<sup>164</sup>. By using the set of transcripts most associated to each regulatory protein as endogenous multiplexed reporter assays, VIPER infers the differential activity of such regulatory proteins between two conditions. We used VIPER to identify regulatory protein changes in BEZ235 or Trametinib treated HCC1143 cells compared to a DMSO control, then mapped these VIPER-inferred protein activity signatures onto multiple

pathway-ontology databases using the DAVID functional annotation tool<sup>165</sup> (Fig. 3-6a, b). These analyses suggested that cells remaining after treatment with a PI3K/mTOR inhibitor had increased pathway activities including MAPK, anti-apoptotic, and NFkB, while those remaining after treatment with a MEK inhibitor had increased pathway activities including PI3K, integrin, FGF and JNK (Fig. 3-6b). Both drug tolerant populations shared enrichment of JAK-STAT, Notch, TGF and Ras pathway regulators. We identified upregulated and targetable proteins in each of these pathways, and evaluated the anti-proliferative synergy using inhibitors against these targets. This included in BEZ235 combinations with ABT737 (BCL2 mimetic), SCH772984 (ERKi), and Trametinib. As well as being evaluated with BEZ235, Trametinib was combined with SP600125 (JNKi), EHOP-16 (RACi), and both drugs were evaluated with combined TG101384 (JAK2i) and DAPT ( $\gamma$ -secretase inhibitor). This strategy identified synergistic drug combinations, indicated by combination indices<sup>166</sup> below 1 at 75% (CI75) and 90% (CI90) inhibitory doses in HCC1143 and SUM149PT cells (Fig 3-7a, b).

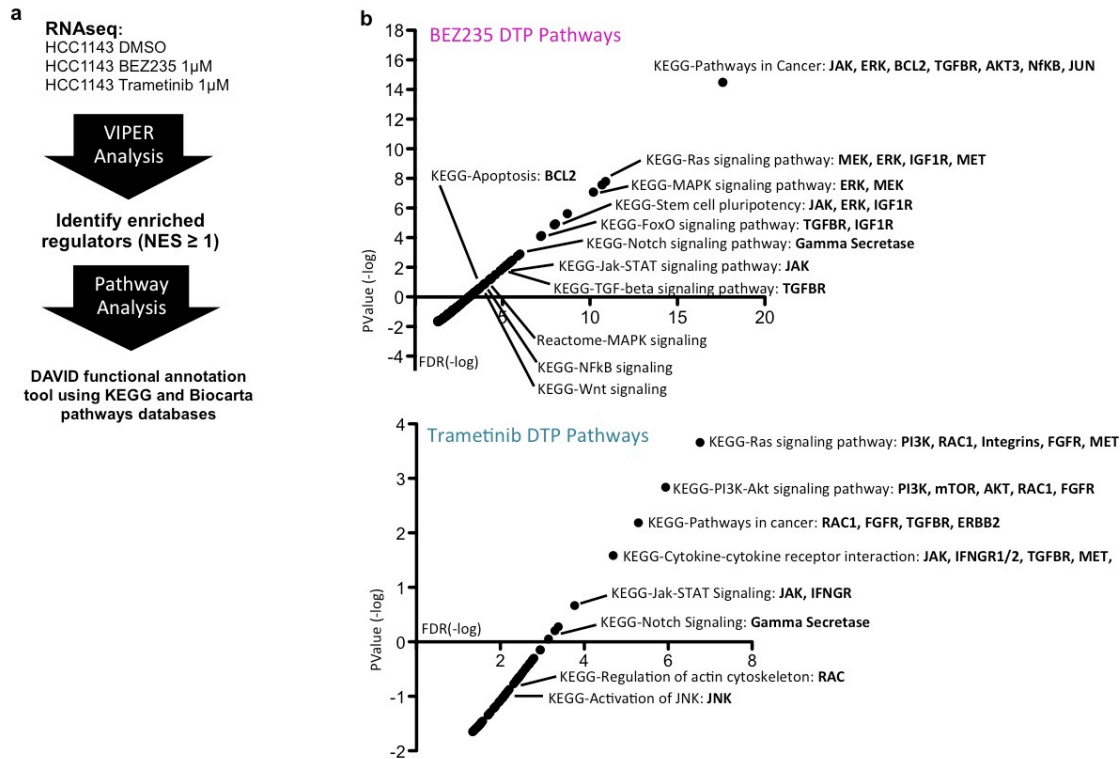


**Figure 3-6: Targeting DTP states using VIPER informed pathway analysis.**

(A) Schematic showing how RNAseq information is analyzed to identify targetable pathway regulators using VIPER and DAVID pathway ontology using the KEGG and Biocarta databases. (B) Plots show enriched pathways identified by the DAVID pathway annotation tool, using upregulated VIPER regulators in BEZ235 and Trametinib DTPs as input. P-value (-log) is plotted against FDR values (-log). Select pathways are labeled, and druggable targets within those pathways are listed.

Direct combination of BEZ235 and Trametinib resulted in the best combination indices, and this combination significantly increased apoptosis (Fig. 3-7c) and significantly reduced S-phase transition as indicated by reduced EdU-incorporation rates (Fig. 3-7d). Despite these encouraging metrics of drug synergy, 100% cell death was never obtained, except with EHOP-16, which showed high single agent toxicity. We investigated the

Trametinib and BEZ235 combo-persisting cell states by assessing K19, K14, and VIM expression by immunofluorescence in three basal-like cell lines, HCC1143, SUM149PT and HCC70, following treatment with combined Trametinib and BEZ235. Figure 3-7f shows that the combo DTP populations in all three cell lines were enriched for a K19<sup>hi</sup> state. We measured the frequency of the four differentiation-marker defined cell states (as in Fig. 3-2a) in response to Trametinib + BEZ235 in HCC1143 cells and found a significant time-dependent increase in the frequency of the K19<sup>hi</sup> state and a significant decrease in VIM<sup>hi</sup> state. There was no change in K14<sup>hi</sup> state, which included cells that maintained high expression of both K19 and K14 (Fig. 3-7g). GSEA results showed that enriched genesets following Trametinib + BEZ235 were a mixture of those observed with either single agent, with few genesets uniquely enriched by combo treatment. (Fig. 3-7h). Together, the GSEA results along with the minimal change in K14 expression suggest that the two drugs maintain divergent effects on the myoepithelial program. In this DTP state, the combo-treated cells showed decreased sensitivity to numerous FDA-approved cytotoxic therapies (Fig. 3-8b). Similar to the single agent treatments, acquisition of this DTP state did not involve state-selective cytostasis, and cells could remain in this DTP state with minimal proliferation for three weeks (Fig. 3-8c, d). However, this state was reversible, and the cell population moved back to control levels of differentiation-state heterogeneity and control levels of sensitivity to Trametinib + BEZ235 combination treatment upon drug withdrawal (Fig. 3-8e-g).

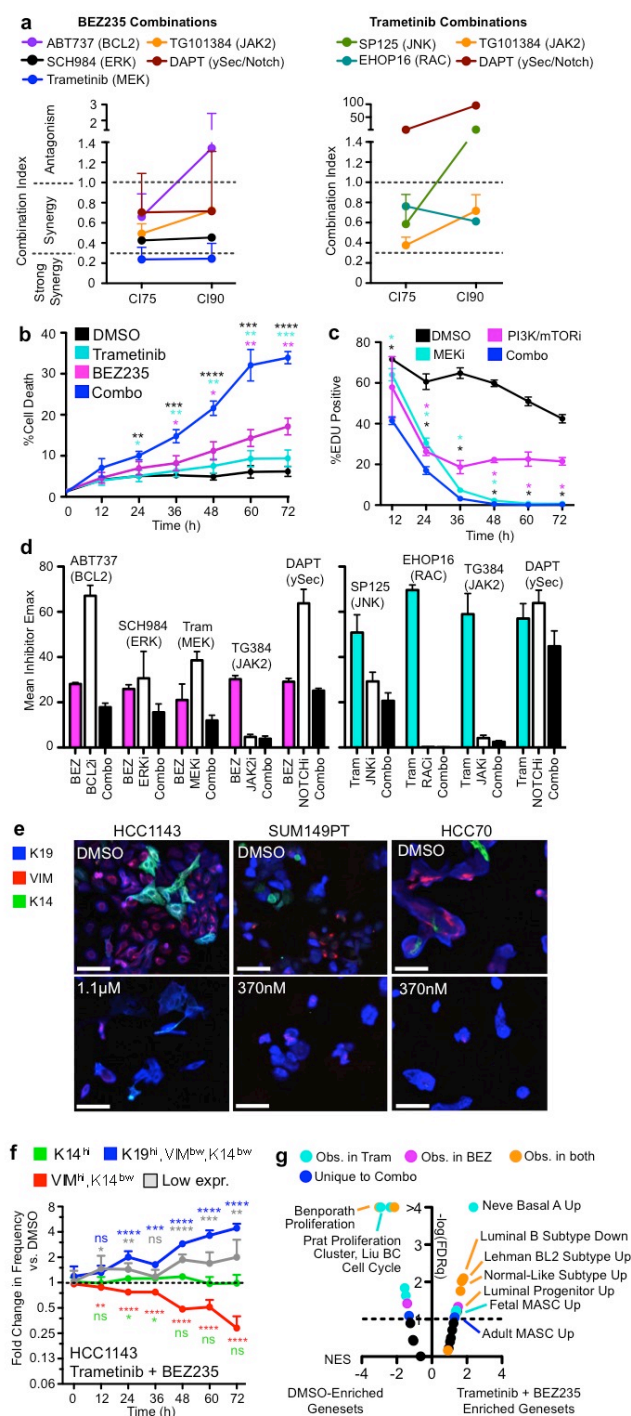


### Figure 3-7: Drug combinations targeting DTP-enriched pathways still leave persisting cells of distinct identity.

(A) Graphs of combination indices (CI) from drug combinations including BEZ235 (left) or Trametinib (right) and agents targeting upregulated pathway regulators in DTP states identified by VIPER analysis. CIs were calculated at 75% (CI75), and 90% (CI90) dose inhibitory values from replicate colorimetric proliferation assays,  $n=3$  with SEM. (B) Graph showing the percent of dying cells (YO-PRO-1+) in HCC1143 cells following the addition of  $1\mu\text{M}$  BEZ235,  $1\mu\text{M}$  Trametinib, the combination of the two drugs, or a DMSO control. Asterisks denote significant gains in percent cell death in combination-treated cells,  $*P < 0.05$ ,  $**P < 0.01$ ,  $***P < 0.001$ ,  $****P < 0.0001$ ,  $n=4$  with SEM. (C) Graphs show the percent of HCC1143 cells positive for EdU following treatment with  $1\mu\text{M}$  Trametinib,  $1\mu\text{M}$  BEZ235, a combination of agents, or DMSO control. Asterisks denote significant reduction in %EdU+ in combination treated cells,  $*P < 0.05$ ,  $n=4$  with SD. (D) Graphs compare the maximal inhibition (EMax, as %control proliferation) for single agent BEZ235, Trametinib, the agents from a, or combinations thereof.  $n=3$  with SEM. (E) IF images of three basal-like cell lines before and after exposure to 72hr of the indicated doses of BEZ235 + Trametinib showing K19 (blue), VIM (red), and K14 (green) expression, DAPI not shown, scale bars =  $100\mu\text{m}$ . (F) Graphs show the fold change in frequency (vs. DMSO) of four differentiation states in HCC1143, as in Fig. 3a,b, following addition of  $1\mu\text{M}$  BEZ235 +  $1\mu\text{M}$  Trametinib. Asterisks depict significant gains or

losses in state frequency vs. 0hr, \* $P \leq 0.05$ ,  $n=15$  with SD. **(G)** GSEA results as a volcano plot of Normalized Enrichment core (NES, x-axis) vs.  $FDRq$  (-log, y-axis) examining 32 genesets related to mammary cell states and breast cancer subtypes, enrichment compared between DMSO and  $1\mu\text{M}$  Trametinib/BEZ235 combination in HCC1143 cells treated for 6d. Select top-enriched genesets are labeled.

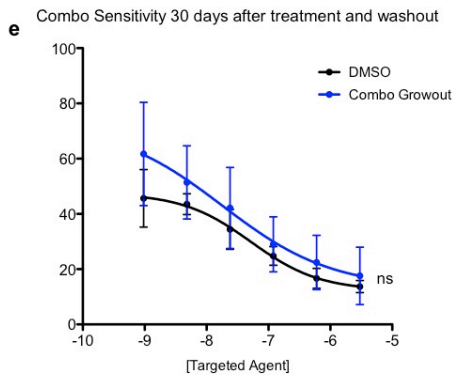
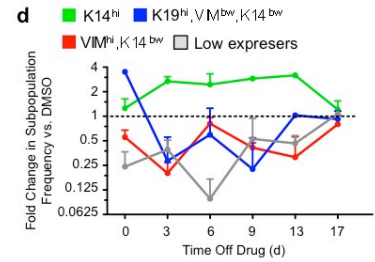
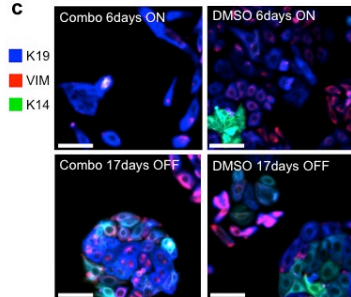
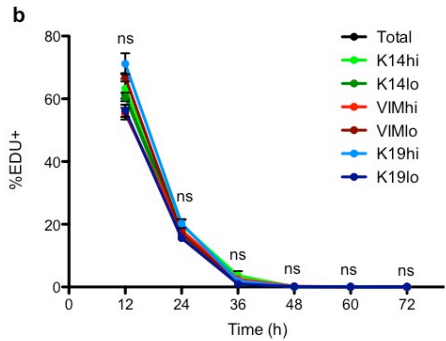
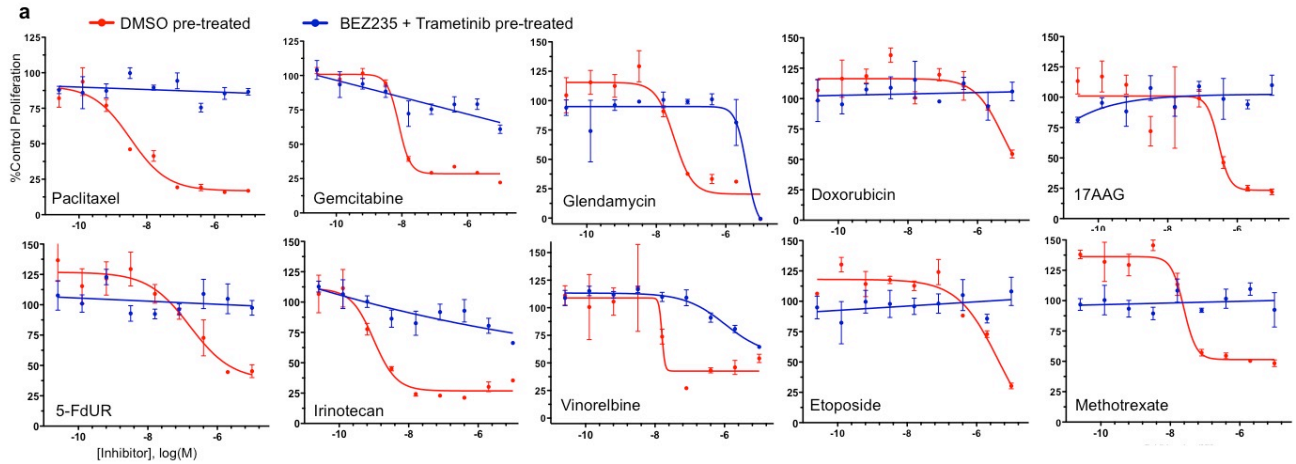


**Figure 3-8: Combination therapy leaves distinct drug-persisting cells that are broadly drug-tolerant and can proliferate and recapitulate heterogeneity upon drug removal.**

(A) Graphs showing Trametinib + BEZ235 treatment-induced changes in cell number (black line, left axis) and population mean-cell intensities (Z-scores, right axis) of K19 (blue), VIM (red), and K14 (green) in HCC1143 following 72hr incubation with increasing doses of two different PI3K/mTORi + MEKi combinations, n=3 with SD. (A) Graphs showing the sensitivity of HCC1143 cells to numerous cytotoxic agents following 72h pre-treatment of DMSO, or 72h pre-treatment with 1 $\mu$ M BEZ235 + 1 $\mu$ M Trametinib, followed by 72h incubation with the cytotoxic agent. (A) Graph showing the frequency of EdU positive cells that also express high or low levels of K14, K19, or VIM in HCC1143 cells following 72hr treatment with 1 $\mu$ M Trametinib + 1 $\mu$ M BEZ235. ns = not significant, n=2, SD on technical replicates shown. (A) Graphs showing cell number and EdU incorporation rates in HCC1143 cells every 3-4 days while being maintained on 1 $\mu$ M Trametinib + 1 $\mu$ M BEZ235 for 21 days, with the cell number and EdU incorporation rate of the DMSO control population shown for the first 3 days of growth. (A) Immunofluorescent images of HCC1143 cells treated with 1 $\mu$ M Trametinib + 1 $\mu$ M BEZ235, or DMSO, for 6 days, and then following 17 days of culture after drug washout. (f) Graph showing cell state composition of 4 differentiation as a fold change vs. DMSO, as in Figure 3a, b, following 72hr of 1 $\mu$ M Trametinib + BEZ235 treatment then drug washout, examining cell state composition every 3-4 days for 17 days, n=4 with SD. (g) Dose response curves showing sensitivity to BEZ235 + Trametinib combination treatment in untreated cells, or cells treated with combination for 72hr then recovered from drug washout for 30 days. ns = not significant, full dose response compared using two-way ANOVA, examining 'interaction'.

### 3.3.4 Inhibiting differentiation-state transitions with BET inhibition

Since we determined that DTP states arise through state transitions and having failed to find a targeted combination that achieved 100% cell kill, we sought to explore different therapeutic strategies. Reasoning that cell-state transitions leading to DTP states requires changes to the chromatin landscape to enhance and express new genes, we looked for enhanced chromatin modification enzyme activity upon the differentiation-state transitions induced by Trametinib

and BEZ235 using GSEA of RNA-seq data. Trametinib and BEZ235 DTPs both showed significant enrichment of genesets related to high BRD4<sup>167,168</sup>, KDM5B<sup>169</sup>, and EZH2<sup>72</sup> activity (Fig. 3-9a). We tested the possibility that BET protein-mediated chromatin regulation supports drug-induced transitions by combining the BET inhibitor JQ1 with Trametinib and BEZ235. While treatment with JQ1 or the kinase inhibitors as single agents could not achieve complete cell kill, the combination of JQ1 and BEZ235 resulted in complete cell kill in all four basal-like cell lines and prevented the formation of a drug tolerant persister population (Fig. 3-9b). This was evidenced by lack of a dose-response curve plateau with JQ1 + BEZ235, significant increases in maximal inhibition and negative projected maximal inhibition (Einf) values for all basal-like lines tested, indicative of the ability to kill all cells. Luminal B cell lines, however, which previously showed minimal cell-state heterogeneity and therapy-induced differentiation-state transition (see Fig. 2-2), did not show a significant increase in maximal inhibition and had positive Einf values for the JQ1 + BEZ235 combination (Fig. 3-9c). Accordingly, drug synergy analysis showed strong synergy between JQ1 and BEZ235 in all basal-like lines, resulting in CI75 and CI90 values <0.5, whereas these drugs had an antagonistic relationship in Luminal B lines with CI75 and CI90 values near or above 1 (Fig. 3-9d). Trametinib + JQ1 also produced synergistic CI values and increases in Emax in basal-like cell lines (Fig. 3-10a, b), however, the combination was not able to completely kill HCC1143 cells at maximum dosing, lacked synergy at CI90, and had positive Einf values, suggesting an inability to enact complete cell kill in this basal-like line. The triple combination of Trametinib, BEZ235, and JQ1 did, however, enact complete cell

kill and prevent DTP formation in HCC1143 (Fig. 3-10c). This synergistic relationship between JQ1 and the MEK and PI3K/mTOR inhibitors is consistent with observed significant gains in cell death (Fig. 3-9e) and significant reduction of proliferation (Fig. 3-9f).

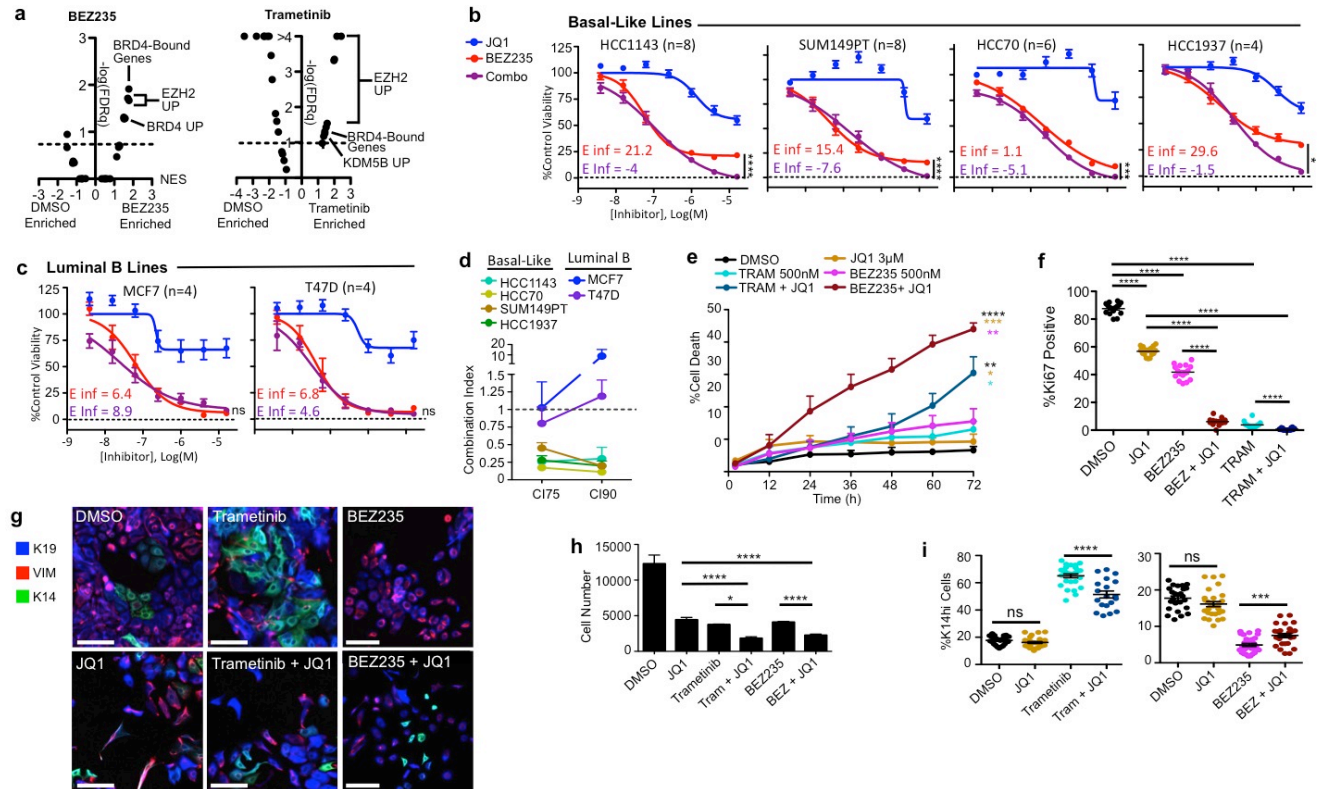


**Figure 3-9: BET inhibitor combinations improve cell kill and suppress DTP transition.**

(A) GSEA results as a volcano plot of Normalized Enrichment score (NES, x-axis) vs.  $-\log_{10}$  FDRq (y-axis) examining 25 chromatin modifier enzyme activity-related genesets, enrichment compared between DMSO and  $1\mu\text{M}$  BEZ235 (left), or DMSO and  $1\mu\text{M}$  Trametinib (right) in HCC1143 cells treated for 6d. Select top-enriched genesets are labeled. (B) Dose-response curves show the efficacy of BEZ235 alone (red), JQ1 alone (blue), or a combination of the two agents (purple, equimolar ratio) in four basal-like cell lines using a colorimetric proliferation assay. E-infinity (Einf) values of single agent BEZ235 (red) and BEZ235 + JQ1 (purple) are displayed. Asterisks depict significant gains in Emax comparing BEZ235 to BEZ235 + JQ1, \* $P < 0.05$ , \*\* $P < 0.01$ , \*\*\* $P < 0.001$ , \*\*\*\* $P < 0.0001$ , ns = not significant, n=5 with SEM. (C) Same as b showing two Luminal B cell lines. (D)

Graph showing combination indices for the BEZ235 + JQ1 drug combination at 75% (CI75), and 90% (CI90) inhibitory doses for 4 basal-like and 2 luminal B BCCLs, n=5 with SEM. **(E)** Graph showing the percent of dying cells (YO-PRO-1+) in HCC1143 following the addition of 1 $\mu$ M BEZ235, 1 $\mu$ M Trametinib, 2 $\mu$ M Jq1, the combinations of these agents, or a DMSO control. Asterisks denote significant gains in percent cell death in combination-treated cells vs. single agent BEZ235 or Trametinib, \*P < 0.05, \*\*P < 0.01, \*\*\*P < 0.001, \*\*\*\*P < 0.001, n=3 with SEM. **(F)** Graph showing the percent of Ki67 positive HCC1143 cells following 72hr of DMSO, 2 $\mu$ M JQ1, 1 $\mu$ M Trametinib, 1 $\mu$ M BEZ235, or combinations with JQ1. Asterisks denote significant difference in Ki67+ frequency, \*\*\*\*P < 0.0001, n=16 with SD. **(G)** IF images of HCC1143 cells following 72hr exposure to DMSO, 400nM BEZ235, 400nM Trametinib, 8 $\mu$ M JQ1, or the combination of these agents. K19 (blue), K14 (green), and VIM (red), DAPI not shown, scale bars = 100 $\mu$ m. **(H, I)** Graphs show total cell number and the frequency of K14hi cells following the treatments outlined in e. Asterisks denote significant change in the frequency of K14hi cells, or cell number, \*P < 0.05, \*\*\*P < 0.001, \*\*\*\*P < 0.001, n=27 with SD.

We next analyzed the influence of JQ1 on differentiation-state marker expression in HCC1143 cells treated at sub-lethal doses with Trametinib, BEZ235, JQ1, or combinations thereof (Fig. 3-9g). JQ1 again significantly reduced cell number when combined with these agents and it suppressed the magnitude of differentiation-state transitions, maintaining a significantly lower frequency of the K14<sup>hi</sup> cell state when used in combination with Trametinib, and maintaining a significantly higher frequency of the K14<sup>hi</sup> state when used in combination with BEZ235 (Fig. 3-9h, i).

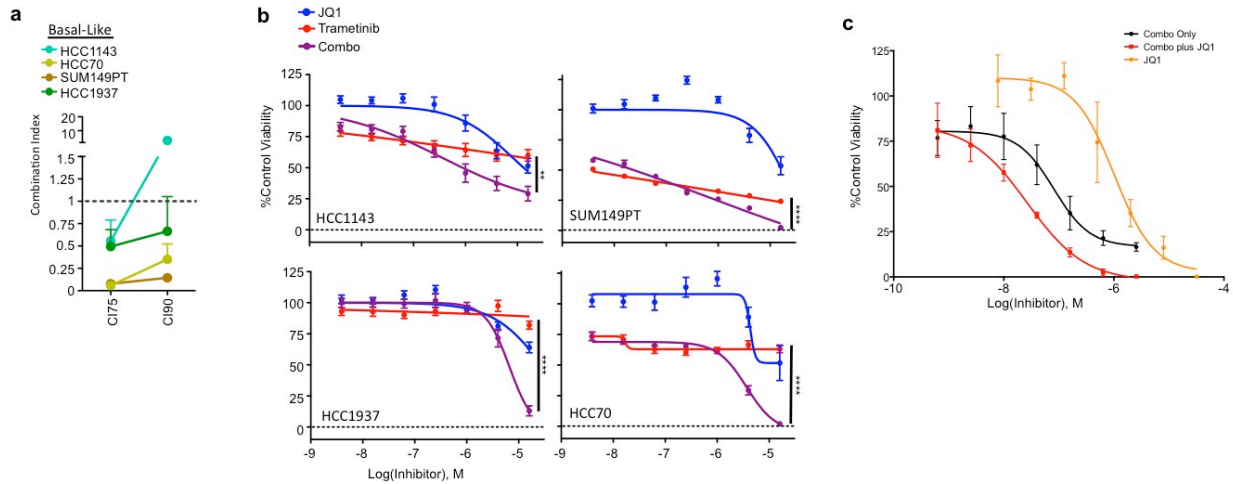


**Figure 3-10: JQ1 shows synergy with Trametinib and Trametinib + BEZ235 combinations.**

(A) Graph showing the combination indices of Trametinib + JQ1 at 75% inhibitory values (CI75) and 90% inhibitory values (CI90) for four basal-like cell lines, n=3 with SEM. (B) Dose-response curves of Trametinib, JQ1, and Trametinib + JQ1 in four basal-like cell lines. Asterisks denote significant gains in Emax between Trametinib and Trametinib + JQ1, \*\*P < 0.01, \*\*\*\*P < 0.0001, n=4 with SEM. (C) A representative dose response curve of BEZ235 + Trametinib, JQ1 alone, and the three drugs in combination in HCC1143 cells. (D) Graph showing the percent of Ki67 positive HCC1143 cells following 72hr of DMSO, 2  $\mu$  M JQ1, 1  $\mu$  M Trametinib, 1  $\mu$  M BEZ235, or combinations with JQ1. Asterisks denote significant difference in Ki67+ frequency, \*\*\*\*P < 0.0001, n=16 with SD.

### 3.3.5 JQ1 prevents chromatin accessibility changes associate with DTP generation

We used single cell combinatorial indexing Assay for Transposase Accessible Chromatin sequencing (sciATAC-seq<sup>170</sup>) to better understand how BEZ235 and Trametinib are affecting the open chromatin architecture to induce DTP states, and how BET protein inhibition might

affect this process. Latent semantic indexing followed by t-distributed Stochastic Neighbor Embedding (t-SNE) was performed to visualize global chromatin architecture differences at single cell resolution between DMSO, BEZ235, and Trametinib treated HCC1143 cells (Fig. 3-11a). This analysis revealed that BEZ235 and Trametinib greatly change the landscape of accessible chromatin regions, inducing distinct state-space enrichment in the t-SNE space. Interestingly, small subpopulations of DMSO cells occupy these BEZ235 and Trametinib regions, consistent with therapeutic-enrichment of a particular chromatin architecture that exists under normal growth conditions. To better understand the contribution of these chromatin accessibility changes to DTP state-transition, we looked for changes in transcription factor (TF) accessibility by examining TF DNA-binding-motif prominence within the open chromatin regions of BEZ235- and Trametinib-DTP cells using chromVAR<sup>171</sup>. We found that the drugs had profound effects on accessibility of specific TF motifs: BEZ235 enriched sites were high in AP1, ATF, and TCF DNA-binding motifs (Fig. 3-11b). Consistent with the mixed luminal and mesenchymal gene expression programs in BEZ235 DTPs (see Fig. 3-1e) we also found increased accessibility of the EMT-promoting TFs ZEB1, TWIST1/2, SNAI1/2, and luminal lineage TFs ESR1, PGR and GATA3. Trametinib DTPs conversely showed enrichment of the SP/KLF family of TFs, Homeobox TFs, and the myoepithelial lineage specific TF EGR1<sup>103</sup> and other EGR family members (Fig. 3-11b). NFkB and Rel motifs were enriched in both DTPs.

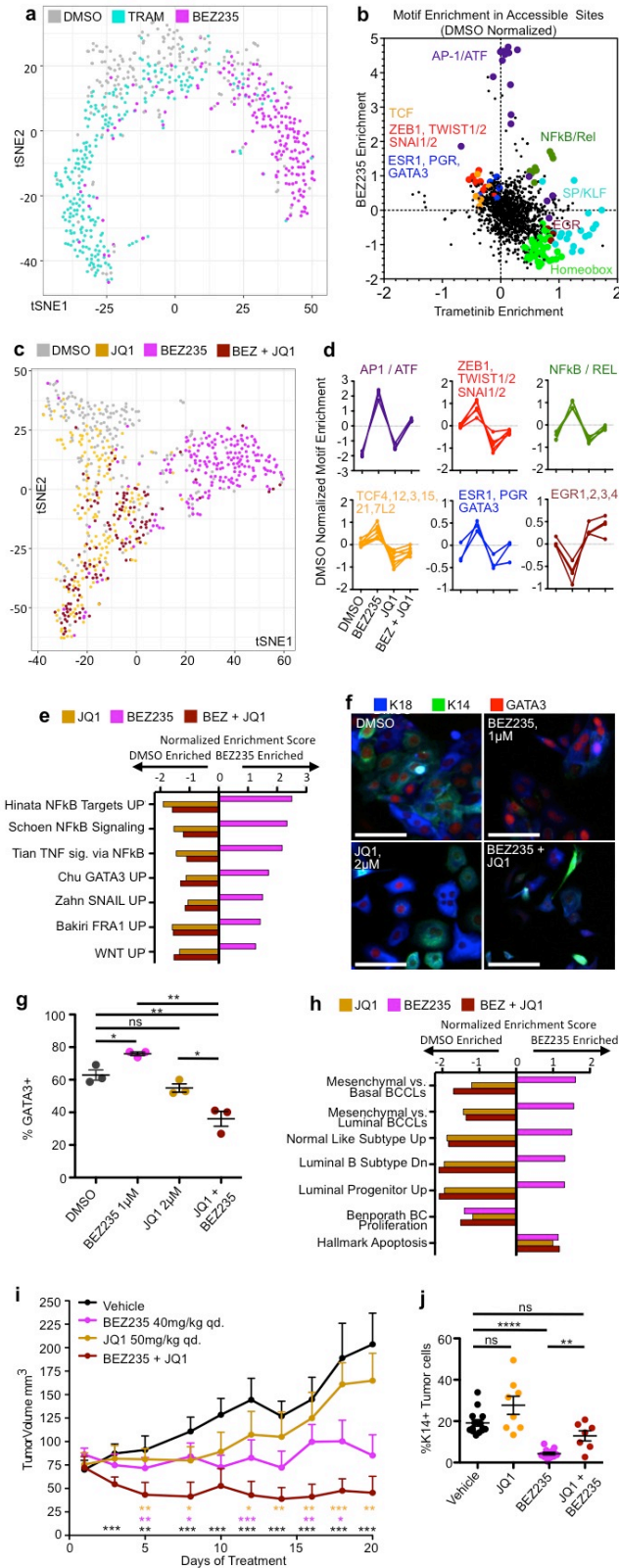


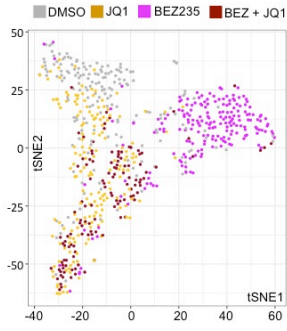
**Figure 3-11: Changes in open chromatin architecture underlie DTP transition and are inhibited by JQ1.**

(A) t-SNE plot of all cells following 72hr of 1μM BEZ235, 1μM Trametinib, or a DMSO control in HCC1143, calculated from sciATAC-seq results. Single cells are colored based on treatment, BEZ235 (magenta), Trametinib (cyan), DMSO (grey) (B) A dot plot showing enriched DNA-binding protein motifs in the open chromatin sites following BEZ235 or Trametinib treatment, normalized to DMSO values. Select related transcription factor motifs are enlarged, colored, and labeled. (C) t-SNE plot of all cells following 72hr of 1μM JQ1 (yellow), 1μM BEZ235 (magenta), JQ1 + BEZ235 (maroon), or a DMSO control (grey), calculated as in a. (D) Line graph showing the level of motif enrichment for six groups of transcription factors is shown for DMSO, BEZ235, JQ1, and JQ1 + BEZ235 treatments. (E) Graph of GSEA results showing the NES of transcription factor activity-related genesets shown to be significantly enriched (p < 0.05) following 72hr of BEZ235 treatment, with the subsequent NES of that geneset in JQ1-treated, and BEZ235 + JQ1-treated cells shown adjacently. (F) IF images showing K18 (blue), K14 (green), and GATA3 (red) expression in HCC1143 cells following 72hr treatment with DMSO, 1μM BEZ235, 2μM JQ1, or BEZ235 + JQ1, scale bars = 100μm. (G)

Graph showing the frequency of GATA3+ cells in HCC1143 following the treatments in *f*, asterisks depict significant differences in GATA3+ frequency, \*P < 0.05, \*\*P < 0.01, \*\*\*\*P < 0.001, n=3 with SEM. **(H)** Graph of GSEA results showing the NES of breast phenotype genesets shown to be significantly enriched (p < 0.05) following 72hr of BEZ235 treatment, with the subsequent NES of that geneset in JQ1-treated, and BEZ235 + JQ1-treated cells shown adjacently. **(I)** A graph shows the change in tumor volume over time of HCC70 xenografts treated with a vehicle control (black line), BEZ235 (40mg/kg QD, red line), JQ1 (50mg/kg QD, blue line), or BEZ235 + JQ1 (purple line). Asterisks denote significant difference in tumour volume between combination treated tumours and other groups, denoted by color: BEZ235, red; JQ1, blue; vehicle, black. \*P < 0.05, \*\*P < 0.01, \*\*\*P < 0.001, n=8 with SEM. **(J)** Graph showing the frequency of K14+ human (KU80+) tumour cells in each HCC70 xenograft following treatment with BEZ235, JQ1, the combination of agents, or vehicle control, n=8 with SEM.

We used sciATAC-seq to further assess how BET inhibition with JQ1 suppresses DTP-state enrichment by BEZ235. Figure 3-5c again shows that BEZ235 enriches a distinct open-chromatin state space as compared to DMSO but that combination with JQ1 inhibits this change, resulting in open chromatin architecture equivalent to single agent JQ1 and highly overlapping with the DMSO-treated population (Fig. 3-11c). In accordance with this inhibition of chromatin alterations, JQ1 combination with BEZ235 normalized the changes in TF-motif accessibility, bringing motif enrichment levels back to near-DMSO values (Fig. 3-11d, Fig. 3-12a, b). The prevention of TF accessibility with BEZ235 + JQ1 combinations was consistent with reduced expression of TF-activity-related genesets measured by GSEA: decreases in AP1, SNAIL, GATA3, NFkB, and TCF motif accessibility in BEZ235 + JQ1 treated cells relative to BEZ235 treated cells correlates with de-enrichment of genesets related to FRA1<sup>172</sup>, SNAI1<sup>173</sup> and GATA3<sup>174</sup> overexpression in mammary cancer cells, NFkB activity-related genesets, and a WNT activity signature<sup>160</sup> (Fig. 3-11e).

**a**

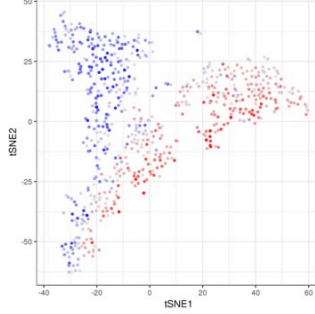


**b** Motif Deviation



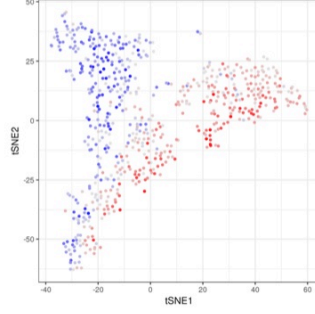
**JUNB**

ESNG00000171223 LINE487 D N3



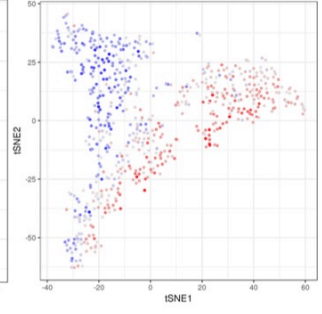
**FOSL1 (FRA1)**

ESNG00000175592 Line505 D N3



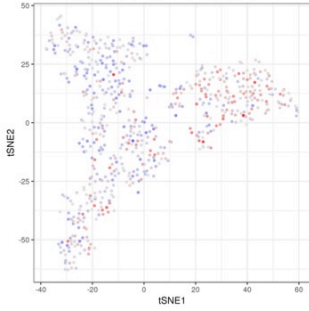
**ATF3**

ESNG00000172772 Line458 D N1



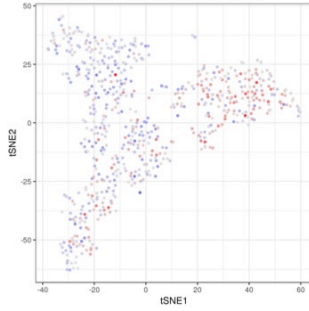
**NKFB1**

ESNG00000109320\_LINE3203\_D\_N3



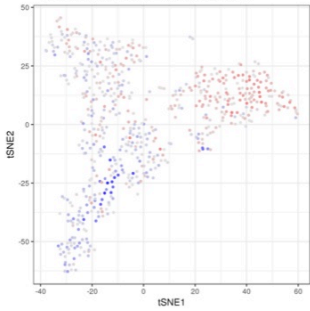
**REL**

ESNG00000162924\_LINE3217\_D\_N3



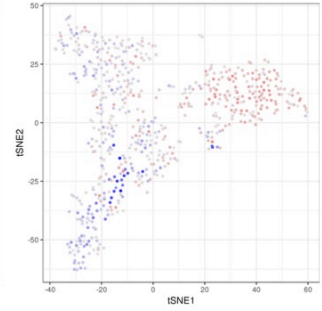
**ZEB1**

ESNG00000148516 LINE575 D N1



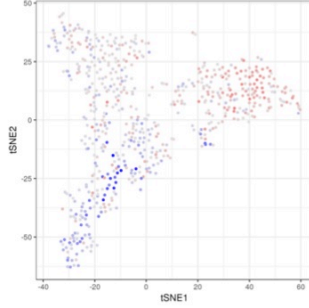
**SNAI2**

ESNG00000019549\_LINE604\_D\_N2



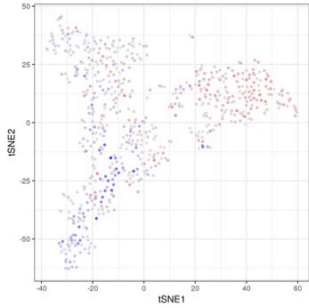
**TCF4**

ESNG00000196628\_LINE303\_D\_N3



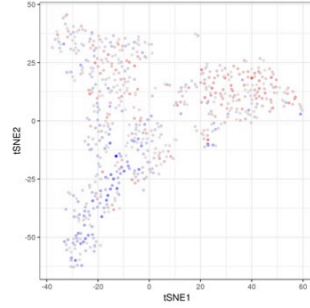
**SNAI1**

ESNG00000124216\_LINE884



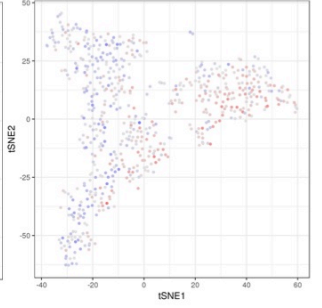
**TWIST1**

ESNG00000122691 LINE162



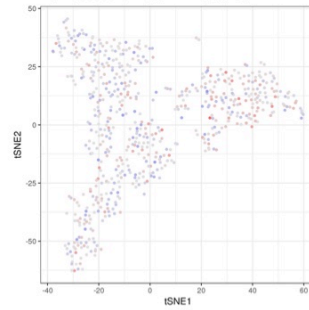
**ESR1**

ESNG00000091831\_LINE2916\_D\_N4



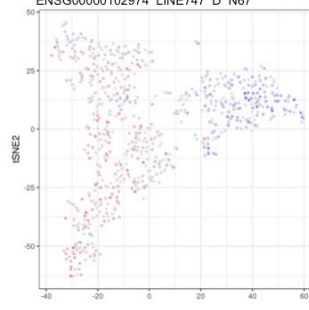
**GATA3**

ESNG00000107485\_LINE2093\_D\_N1



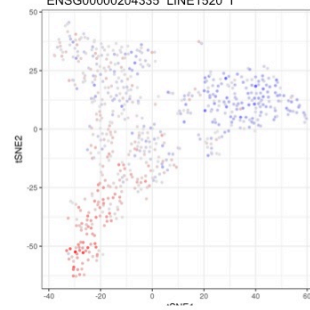
**CTCF**

ESNG00000102974 LINE747 D N67



**SP5**

ESNG00000204335 LINE1520 I



**KLF11**

ESNG00000172059 LINE3300 I N3

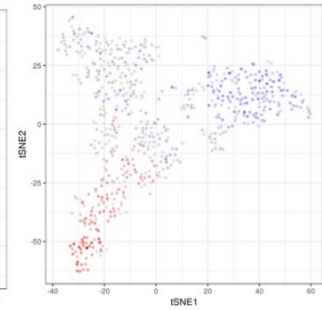


**Figure 3-12: JQ1 prevents BEZ235-driven changes in open chromatin architecture and TF accessibility.**

(A) Figure 6c is presented again for reference for the following plots. (B) t-SNE plot showing sciATACseq results of HCC1143 cells treated with BEZ235, JQ1, BEZ235 + JQ1 or a DMSO control. Each single cell point is colored based on the level of DNA-binding motif enrichment of the listed transcription factor

We further assessed GATA3 gene expression and protein level changes and found that BEZ235 drove increases in *GATA3* expression and increased nuclear GATA3 protein levels, whereas Trametinib reduced these levels (Fig. 3-11f, Fig. 3-13a-d). Consistent with the effects of JQ1 combination on GATA3 motif accessibility, JQ1 prevented the increases in GATA3 mRNA and protein expression when combined with BEZ235 (Fig. 3-11g, Fig. 3-13 e-f).

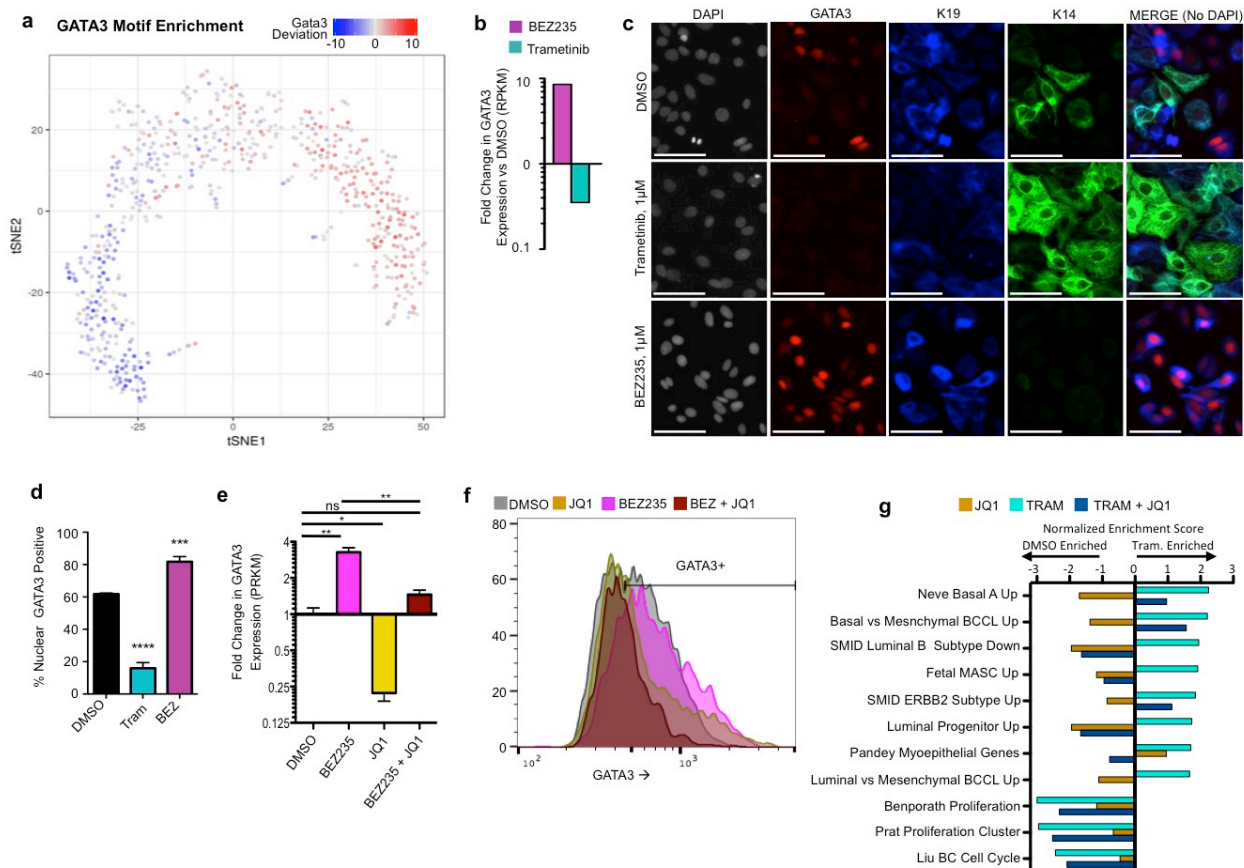


**Figure 3-13: JQ1 prevents open chromatin architecture changes that support DTP state formation.**

(A) GATA3 motif enrichment in the open chromatin regions of DMSO, Trametinib, or BEZ235 treated HCC1143 cells is shown on a t-SNE plot of single cells using sciATACseq. The treatment for each individual cell is displayed by color in Figure 6a, red indicates increased motif enrichment, and blue indicates reduced motif enrichment. (B) Graph showing changes in GATA3 gene expression as a fold change vs. DMSO following 6d of 1 $\mu$ M BEZ235 or 1 $\mu$ M Trametinib treatment. (C) IF images showing single cell expression of GATA3 (red), K19 (blue) and K14 (green) following 72 of 1 $\mu$ M BEZ235, 1 $\mu$ M Trametinib, or a DMSO control. Scale bars = 100 $\mu$ m. (D) Graph showing the quantitation of the frequency of GATA3+ cells in HCC1143 following 72 of 1  $\mu$  M BEZ235, 1 $\mu$ M Trametinib, or a DMSO control. (E) A dot plot showing DNA-binding protein motif enrichment analysis between BEZ235 and BEZ235 + JQ1, both normalized to DMSO motif enrichment levels. (F) Histograms showing mean-nuclei intensities of GATA3 in HCC1143 cells following 72hr treatment with DMSO (grey), 2 $\mu$ M JQ1 (yellow), 1 $\mu$ M BEZ235 (pink), or BEZ235 + JQ1, the gate for GATA3 positivity is shown. (G) Graph of GSEA results showing the NES of breast phenotype genesets shown to be significantly enriched ( $p < 0.05$ ) following 72hr of Trametinib treatment, with the subsequent NES of that geneset in JQ1-treated, and Trametinib + JQ1-treated cells shown adjacently

JQ1 combinations with BEZ235 also prevented the enrichment of breast phenotype genesets associated with the BEZ235 DTP state (Fig. 3-11h, for BEZ235 alone see Fig. 3-1e). Importantly, geneset enrichment related to loss of proliferation and increased apoptosis did not reverse with JQ1 combinations, and were enriched in all drug treated conditions (Fig. 3-11h). This prevention of DTP-specific geneset enrichment was also observed with Trametinib and JQ1 combinations (Fig, 3-12g).

Since we found dramatic inhibition of BEZ235-induced state changes by JQ1 along with synergistic gains in cell death and reductions in proliferation more prominently than with Trametinib + JQ1, we tested the efficacy of the BEZ235 + JQ1 combination *in vivo* in

an orthotopic xenograft model using the tumour-forming basal-like HCC70 cells. The BEZ235 + JQ1 combination significantly reduced tumour volume compared to either single agent (Fig. 3-11i, Fig. 3-14a), consistent with the synergy observed *in vitro* with this line (Fig. 3-9b, d). Furthermore, immunofluorescent staining of the control and treated tumors showed that BEZ235 treatment alone reduced the number of K14 expressing cells, while combination treatment of BEZ235 + JQ1 prevented the K14<sup>low</sup>-state aggregation (Fig. 3-11j, Fig. 3-14b). These results are similarly consistent with our observations across basal-like cell lines *in vitro* (Fig. 3-1d, 3-9g-i), supporting the utility of JQ1 to prevent BEZ235-induced DTP transitions *in vivo*.

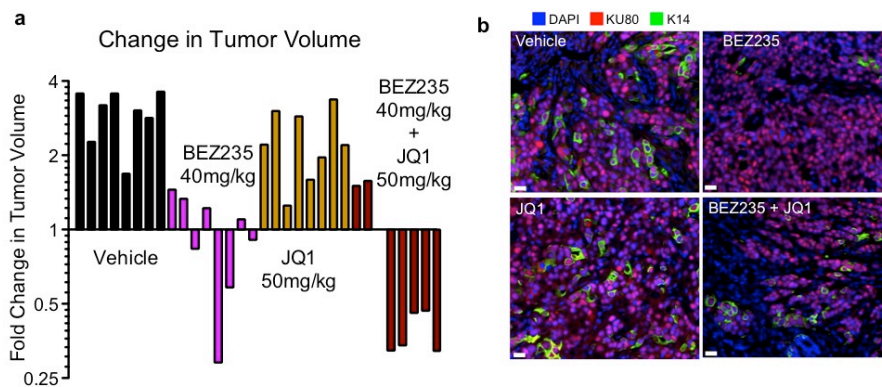


**Figure 3-14: JQ1 combines with BEZ235 *in vivo* to reduce tumor volume and suppress cell-state transitions.**

**(A)** A waterfall plot shows the change in individual tumor volume, comparing treatment initiation size to size at resection (treatment day 21). Bars are colored by treatment: Vehicle (black), BEZ235 (magenta), JQ1 (yellow), BEZ235 + JQ1 (maroon). **(B)** Representative IF images of HCC70 xenograft tumors treated with vehicle, BEZ235, JQ1, or the combination of JQ1 + BEZ235 showing DAPI (blue), human specific marker Ku80 (red) and K14 (green), scale bars = 100µm

### 3.4 Discussion

Our overall goal in this study was to develop therapeutic strategies to more effectively treat breast tumours that exhibit intratumoral phenotypic heterogeneity and plasticity. Examination of the phenotypic response of heterogeneous basal-like cell lines to 119 pathway-targeted inhibitors revealed that most drugs are ineffective at inducing complete cytotoxicity, and leave residual cells with altered expression of differentiation-state markers. These findings align with multiple studies where targeted therapeutic challenge drives cells into low-proliferative, drug-tolerant persister “DTP” states<sup>24,70,122</sup>. Indeed we found that MEK and PI3K/mTOR inhibitors, as well as the combination of these agents, drove basal-like cell lines into distinct DTP states with reduced proliferation that can persist under high-dose inhibitor for weeks. Contrary to a model of Darwinian selection, and consistent with these previous studies of reversible drug tolerance<sup>24,70,122</sup>, cells that were grown out of these DTP states regained differentiation-state heterogeneity, and when later re-challenged with inhibitor they showed no significant differences in drug sensitivity compared to treatment-naïve cells. Furthermore, no differentiation-state specific cytostasis or cell death was evident in our experiments, indicating cell-state transitions are the major driver of DTP phenotype acquisition. Computational modeling efforts (see Fig. 3-4h, 3-5f) further supported that state-transitions are necessary to generate the observed DTP state aggregation by MEK and PI3K/mTOR inhibitors.

DTP state-transition in basal-like breast cancer cell lines involved the rewiring of the signaling network, and VIPER analyses identified many upregulated kinases in Trametinib and BEZ235 DTP cells known to cancer cell survival, consistent with previous work characterizing kinome rewiring following targeted MEK and PI3K inhibition in breast cancer<sup>124,175,176</sup>. In addition to these pathway alterations, our imaging assays detail profound alterations in cancer cell differentiation status as cells acquire MEK and PI3K/mTOR DTP states. Basal-like cell lines have been shown to have a high propensity for differentiation-state transition under normal growth conditions<sup>93</sup>, and our work demonstrates that this inherent plasticity is exemplified upon therapeutic challenge. These effects on differentiation were target dependent, and MEK and PI3K/mTOR inhibitors had a divergent influence on the frequency of cells in a K19+/K14+ cell state. Trametinib aggregated cells in this bilineage state through induction of myoepithelial gene expression programs, and enriched luminal progenitor and fetal mammary stem cell genesets<sup>98</sup>, representing two distinct mammary cell states with mixed expression of basal and luminal markers<sup>51,95,115</sup>. Consistent with this, Trametinib DTPs showed high EZH2 geneset enrichment, a histone methyltransferase shown to promote bilineage content in basal-like BCCLs including basal and luminal progenitor gene expression programs<sup>72</sup>. BEZ235 DTPs, conversely, were depleted of basal marker expression and had mixed luminal/mesenchymal gene expression programs. Single cell indexed ATACseq analysis of these distinct DTP states provided mechanistic insight into these differentiation-state transitions, revealing that the acquisition of DTP states involved dramatic open chromatin architecture changes that altered the chromatin accessibility, and activity, of

known cell-fate determining transcription factors. These factors included EGR1 in Trametinib DTPs, and AP1, ZEB1, SNAI1 and GATA3 in BEZ235 DTPs, consistent with the role of these TFs in basal, mesenchymal and luminal differentiation in breast cells<sup>72,103,148,172,174</sup>. Taken with our imaging and gene expression analyses, these sciATAC-seq results suggest that targeted therapeutics may often invoke large-scale epigenomic transitions in basal-like breast cancer cells, restructuring the chromatin to allow specific TF access, and invoking gene regulatory programs that promote distinct cellular differentiation and drug tolerance.

Chromatin modifier enzymes appear to be critical in this epigenomic transition to DTP states. MEK and PI3K/mTOR DTP states both showed increases in genesets relating to epigenetic modifier enzymes known to control DNA accessibility, including the BET family epigenetic reader proteins, histone demethylase KDM5B, and histone methyltransferase EZH2. Accordingly, we found that targeted BET inhibition with JQ1 could suppress the DTP transitions promoted by Trametinib and BEZ235 on both an imaging and transcriptional level. Further, we found that combination with JQ1 suppressed the chromatin architecture changes and subsequent changes to TF accessibility and activity that supported BEZ235 DTP identity. The inhibition of DTP state-acquisition by JQ1 when combined with MEK or PI3K/mTOR inhibitors resulted in significant gains in cell death, reduction of proliferation, and tumor regression when BEZ235 and JQ1 were combined *in vivo*. This aligns with previous work demonstrating antiproliferative synergy between MEK and PI3K pathway

targeted inhibitors and BET inhibitors. These studies demonstrate that targeted BET inhibition can prevent compensatory kinase upregulation supporting drug tolerance<sup>123,124</sup> by preventing BRD4 association with compensatory kinase gene enhancers<sup>18</sup>. Taken with our findings that JQ1 prevents a more global phenotypic transition to drug-induced DTP states with distinct open chromatin architecture, TF access, and cellular differentiation, it is likely that BRD4-supported drug tolerance mechanisms involve not only compensatory kinase gene enhancement, but also enhancer formation for many regulatory proteins including the pivotal TFs profiled in this study. Further, it remains to be explored how the targeting of other ongoing chromatin modifier processes in these DTP states may prevent their formation, such as the observed increases in histone demethylase and methyltransferase activities, including EZH2, which was greatly enriched in Trametinib-persisting HCC1143 cells where JQ1 combinations were not as effective at enacting complete cell kill.

Together, the findings in this work and related studies support the idea that inhibiting mechanisms of chromatin dynamics will be necessary to improve targeted therapy efficacy in triple negative and basal-like breast cancers. We propose that combination therapies which combine a state-transitioning drug (e.g. BEZ235) with a repressor of chromatin dynamics represents a powerful option for the treatment of basal-like tumours. While targeted BET inhibition is an effective option for these combinations and can greatly increase the cytotoxicity of both MAPK and PI3K pathway-targeted agents, other epigenetic targets must be considered for optimal efficacy in specific cases. We believe that the advancement of these

combinations will be critical to improving our management of tumors with high cell-state heterogeneity and plasticity.

## 3.5 Miscellaneous

### 3.5.1.1 Authorship

TR., E.M.L, J.R., J.W.G. and R.C.S. designed the study. T.R., R.C.S., J.W.G. wrote the manuscript. M.L. and L.D. generated the patient-derived xenografts and T.R. imaged the tumors; T.R. and K.C. performed primary tumour immunofluorescence. T.R. performed cell line gene expression analysis, cell culture, therapeutic screening (with J.R.), image cytometry, cell death and S-phase quantitation assays, geneset enrichment analysis, cell line synergy testing. K.JC and P.S. performed the mass cytometry experiments and analyses. M.P.C. and C.J.T. developed the computational models with statistical help from A.J.A. T.R. and N.W. performed the RNA sequencing and C.P. performed the alignment and expression analysis and other bioinformatics support. M.A. and A.C. performed VIPER analyses. T.R. and N.K. carried out the animal studies. T.R. and A.F. performed sciATAC-seq assays, A.A and T.R. analyzed sciATAC-seq data.

### 3.5.1.2 Acknowledgements

We would like to thank Dr. Megan Troxell of the OHSU Pathology Department for her assistance in obtaining and analyzing primary breast cancer tumour samples from the OHSU Biobank, the Bradner Lab of the Dana-Farber Cancer Institute for their generous donation of JQ1 for our animal studies, Dr. Dimitri Rozanov for providing cytotoxic therapy screening plates, Dr. Dan Georgess for his assistance with statistics, Elmar Bucher for the generation of data management python code, and Dr. Jason M. Link for his generation of an image analysis pipeline. We acknowledge Bob Searles and MPSSR core at OHSU for their sequencing efforts.

### 3.5.1.3 Conflicts of interest

The authors have no conflicts of interest to disclose.

### 3.5.1.4 Funding

T.R. is supported by the Ruth L. Kirschstein PMCB T32 Training Grant, Vertex Pharmaceuticals Scholarship, and Tartar Trust Fellowship. E.L is supported by\_\_ M.C. is supported by the NSF Graduate Research Fellowship Program and the Berkeley Fellowship for Graduate Study. A.C. is supported by NIH grants U01/5U01CA168426-04(AC, MA) and R35/1 R35 CA197745-01(AC). C.J.T. is supported by the NIH Center "Systems Biology of Collective Cells Decisions" through Stanford University NIH #P50GM107615. R.C.S is supported by the National Institutes of Health, National Cancer Institute R01 CA129040 and R01 CA100855, the Department of Defense Breast Cancer Research Program BC103625, the Colson Family Foundation, and the Prospect Creek Foundation. J.G. is supported by the National Institutes of Health, National Cancer Institute grant U54 CA 112970, by the Susan G. Komen Foundation, and the Prospect Creek Foundation. Sequencing and Flow Cytometry Core work was supported by the Knight Cancer Institute Cancer Center Support Grant 5 P30 CA69533.

## 4 Targeting Heterogeneous and Plastic Triple Negative Breast Cancers with Small Molecule Activators of PP2A

**Tyler Risom**, Xioayan Wang, Mahnaz Janghorban, Stoddard Meigs, Dale Christensen,

Goutham Narla, Rosalie Sears

The data presented in this chapter are unique to this dissertation and have not been published. I designed the experimental approach in this manuscript and performed the majority of experiments. Mahnaz Janghorban tested DT061 in breast cancer cell lines, and Xiaoyan Wang developed the mouse model and performed the *in vivo* drug studies. I personally drew conclusions from the results.

## 4.1 Abstract

Single agent kinase inhibitors have shown limited success in Triple Negative breast cancer patients, in part due to enhanced cell-state plasticity in this subtype, resulting in the generation of drug tolerant cell states following challenge with kinase inhibitors. This resistance can be overcome through pairing kinase inhibitors with epigenetic reader protein inhibitors, and we detail this success of this combination therapy in Chapter 3. However, due to the diverse genetic landscape of TN tumors, these strategies may be ineffective in some patients who possess mutations in these epigenetic protein targets, or resistance may arise through yet unknown mechanisms. To best manage TN tumors we must expand our therapeutic arsenal to include diverse therapeutic strategies that are similarly efficacious in phenotypically heterogeneous and plastic TN tumors. The simultaneous targeting of multiple kinases offers an attractive approach, however, small molecule multi-kinase inhibitors have resulted in pronounced toxicity in normal cells, limiting their advancement. Pharmacological activators of PP2A offer a unique, safe, strategy to simultaneously repress many kinase targets with minimal detrimental effects on normal cells by re-activating endogenous phosphatases that have been specifically repressed in tumor cells. Here I demonstrate the efficacy of these pharmacological activators of PP2A at treating heterogeneous and plastic TN cell lines and tumor models. I show that these agents inhibit proliferation, induce cytotoxicity, and inhibit tumor growth, all while avoiding drug-induced differentiation-state plasticity, highlighting their potential as an additional strategy to manage TN tumors.

## 4.2 Introduction

Cell transformation to an oncogenic state involves the accumulation of genetic mutations, copy number alterations, translocations, and epimutations in order to establish oncogene activation and tumor suppressor inactivation<sup>177</sup>, leading to unchecked proliferation in the malignant state. These overactive proliferation and survival pathways use kinases as a major conductor pathway signaling, and the majority of efforts to develop targeted therapies against cancer cells have focused on inhibiting these kinases. These strategies included developing drugs that compete for ATP binding to the catalytic kinase domain of these proteins, or drugs that covalently bind and modify kinase function<sup>178</sup>. Accordingly, 28 kinase-targeted therapies have now been approved for use as cancer therapy with dozens more in clinical development<sup>179</sup>. These kinase inhibitors (KIs) show strong enzymatic inhibition of their target kinases and robust antiproliferative efficacy on cancer cell lines *in vitro* and tumor xenografts *in vivo*. However, resistance to these agent is prevalent, and most cause considerable toxicity, resulting in the relatively low number of FDA-approved kinase inhibitors at this current date<sup>180</sup>.

Resistance can occur through genetic alterations of the drug target<sup>90</sup>, “bypass signaling” by which compensatory pathway circumvent the biological effect of drug target inhibition<sup>123,124,175</sup>, through cell-state transition to a new state where the drug target is not influential on survival<sup>24,67,121</sup>, or by many other mechanisms (see chapter 1.2, 1.3). While KI combinations or schedules may circumvent some of these resistance mechanisms, the

addition of more drugs comes at a high cost of increased side effects and toxicity<sup>181,182</sup>, particularly when using the near-maximum-tolerated doses prescribed by FDA guidelines. For these reason we see many patients having to switch therapy due to lack of efficacy, or due to adverse medical events from kinase inhibitor side effects. New therapeutic strategies are therefore needed to circumvent the resistance mechanisms and treatment-ending toxicities associated with clinical kinase inhibitor use.

Pharmacologic activators of Protein Phosphatase 2A may provide this solution. Kinase activity is highly dependent on the post-translational modifications, including activating phosphorylation marks that promote protein activity. Active kinases then phosphorylate and activate subsequent kinases\*, leading to the continuation of the signaling cascade. Endogenous phosphatases, like PP2A, represent a regulatory mechanism to control these signaling cascades by dephosphorylating kinases, which primarily inactivates or dampens their activity. While there are 538 protein kinases in the genome<sup>183</sup>, there are only ~200 phosphatases, which cover the dephosphorylating functions of both protein and lipid substrates<sup>184</sup>. Because of this, protein phosphatases are promiscuous, often having many substrate targets. PP2A is no exception, and is the major serine-threonine phosphatase in the cell that subsequently regulates many signaling pathways, including the PI3K pathway, MAPK pathway, MYC signaling, apoptosis signaling, SRC signaling and more<sup>126</sup>. It utilizes a repertoire of unique target-specific  $\beta$  subunits to obtain target selectivity, while having a conserved catalytic (C)

---

\* Site-specific phosphorylation can also be repressive, by which phosphatase activity increases enzyme activity.

and structural subunit (A) that travel amongst these  $\beta$  subunits for binding, formation of the heterotrimeric holoenzyme, and phosphatase function<sup>126,185</sup>.

In malignant cells, which have characteristically hyperactive kinase signaling, it not surprising that we find inactivation of endogenous phosphatase function, including PP2A. This can occur through genetic alteration of one of the 17 PP2A complex genes, through post-translational modification of the PP2A catalytic subunit, or through increased expression of endogenous inhibitors of PP2A including the SET (inhibitor 2 of PP2A, I2PP2A) or CIP2A (cancerous inhibitor of PP2A) proteins<sup>131,185</sup>. Indeed reduced levels of PP2A are observed in many tumor types<sup>131,132,186,187</sup>, which often coincides with higher expression of SET<sup>129,131,132,188</sup> and CIP2A<sup>128,189</sup>.

Due to its multi-pathway regulatory activity in the cell, reactivation of PP2A in cancer cells can lead to loss of proliferation and enhanced cytotoxicity. This has been demonstrated through increasing levels of active PP2A in cancer cells by inhibiting SET and CIP2A through both RNA interference and pharmacological inhibition by such agents as the SET inhibitor OP449<sup>128,132,132,188,190</sup>. Further, direct pharmacological activators of PP2A, including forskolin and FTY720, can elicit similar responses and result in increased PP2A activity and cell death in many different malignancies<sup>191-194</sup>. While these preclinical studies have provided a strong proof-of-principle that pharmacologic activation of PP2A represents a promising option for cancer therapy, many of these therapeutics have low potential as clinical

trial candidates due to poor target specificity, required dose, pharmacokinetics, and pharmacodynamics.

A recent discovery that phenothiazines induce potent cytotoxicity in lymphoma through increasing PP2A activity<sup>133</sup> has spurred the development of a new class of small-molecule activators of PP2A (SMAPs)<sup>195</sup>. These agents induce a conformational change in the A subunit and result in increased activity of the heterotrimeric complex<sup>130</sup> and result in potent cancer cell killing *in vitro* and antitumor activity *in vivo*<sup>130,185</sup>. Due to their simultaneous inhibition of multiple oncogenic pathways, SMAPs represent a promising strategy to treat triple negative breast cancer tumors, which possess high cell state heterogeneity and plasticity and show resistance to most single-agent KIs and chemotherapy through cell state transition and bypass of target inhibition<sup>129,184</sup>. In this study, we profile the antiproliferative and cytotoxic potential of SMAPs to treat these heterogeneous and plastic triple negative breast cancers. We show that both indirect activation of PP2A via SET inhibition, and direct PP2A-activation by SMAPS are able to completely kill TN cell lines *in vitro*. Further, phenotypic analysis of cells at sub-lethal doses of SMAPs reveals that the cell-state plasticity associated with adaptive inhibitor resistance is not elicited by these PP2A activators, conversely all phenotypic subpopulations of cells are equally affected. We present the robust antitumorigenic activity of SMAPs in murine models of TN breast cancer, and further show that SMAPs kill all phenotypic subpopulations in tumor-derived cell lines from these murine models. Finally, we use an unbiased drug screening approach to identify

targeted therapies that synergize with PP2A activators, which may be useful for future enhancement of clinical efficacy by combination therapy with SMAPs + KIs. Together, these findings identify a novel method that can potentially better manage tumors with high rates of cell-state heterogeneity and plasticity, like triple negative breast cancer.

## 4.3 Results

### 4.3.1 Activators of PP2A effectively inhibit proliferation and induce cytotoxicity in triple negative cell lines

We first examined the effect of the indirect and direct activators of PP2A on triple negative breast cancer cell viability. OP449 is an inhibitor of SET, and endogenous-inhibitor of PP2A activity, which has elevated expression in most breast cancers<sup>132</sup>. OP449 effectively killed all triple negative breast cancer cell lines examined which included four basal-like lines (MDAMB468, HCC1143, BT20, HCC1937) and four claudin-low lines (BT549, HCC38, MDAMB231, MDAMB436) at IC50 concentrations ranging from 700nM - 2 $\mu$ M (Fig. 4-1a). Consistent with this, the small molecule activator of PP2A, DT061, induced complete cell kill in all TN lines examined, which included 8 basal-like lines (Fig. 4-1b), and 5 claudin-low lines (Fig. 4-1c). We examined the level of cell death throughout treatment with DT1154, an analog of DT061, in three basal-like lines and found that cell death was robustly enhanced by DT1154 and increased with therapeutic dose (Fig. 4-1d).

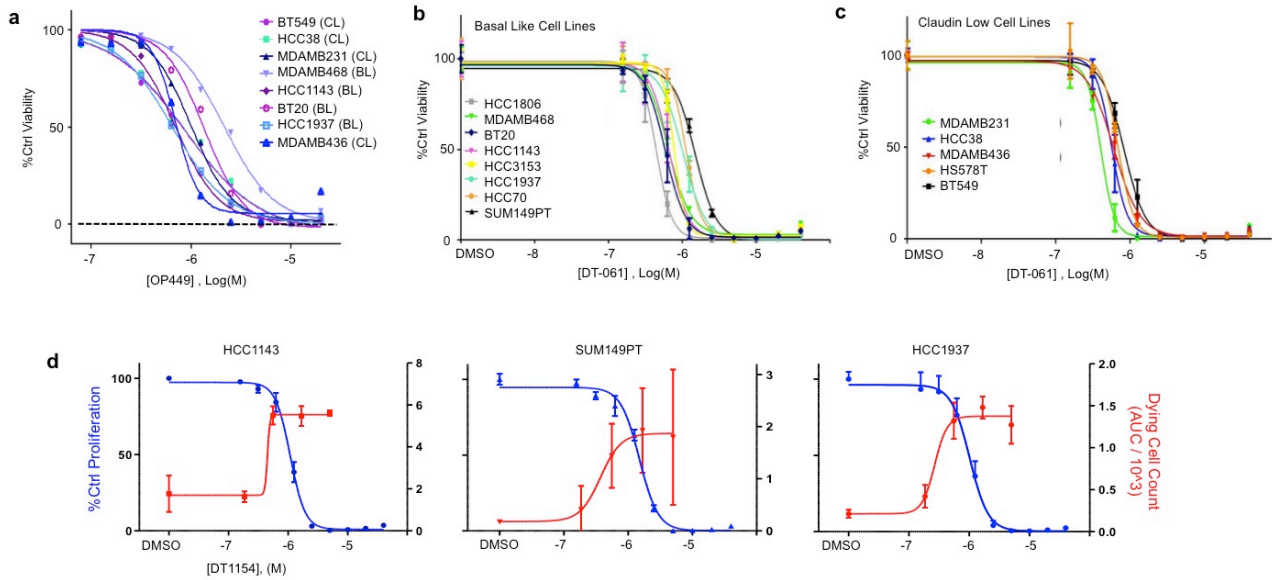


**Figure 4-1: Activators of PP2A induce complete cytotoxicity in triple negative cell lines**

(A) Growth inhibition curves are shown for 8 triple negative breast cancer cell lines following 72hr treatment with OP449 at increasing doses, including four basal-like (BL) and four claudin-low (CL) lines. (B) Growth inhibition curves are shown for 8 basal-like breast cancer cell lines following 72hr treatment with DT061 at increasing doses. (C) Growth inhibition curves are shown for 5 basal-like breast cancer cell lines following 72hr treatment with DT-061 at increasing doses. (D) Graphs show the effect of DT1154 on cell proliferation (blue) and cell death (red, as area under the curve of YOPRO1+ objects over 72hr) in three basal-like cell lines at increasing doses.

### 4.3.2 SMAPs effectively kill all differentiation states in heterogeneous TN cell lines and tumor models

We next investigated the influence of SMAPs on cellular differentiation-states, using high content imaging of control and sub-lethally treated basal-like cell lines with DT1154. Using cell segmentation, quantitation of cellular marker expression, and image cytometry (Fig. 2-2a, b), we calculated the frequencies of differentiation states in four basal-like cell lines before and after treatment. Differentiation states were based on cellular expression of the luminal Cytokeratins 19 and 18 (K19, K18), basal markers Cytokeratin 14 and 5 (K14, K5), and the mesenchymal marker vimentin (VIM). Consistent with previous studies<sup>67,117,118</sup> (Fig. 2-2) we found that basal-like cell lines harbored distinct subpopulations of cells in basal, luminal, mesenchymal, and mixed differentiation states, each line possessing a distinct ratio of these states under normal growth conditions (Fig. 4-2a-d). Unlike the phenotypic influence of kinase-targeted therapies on these lines (see Fig. 3-1), DT1154 treatment resulted in only minor shifts in the frequencies of differentiation states, with no major expansion or loss of an existing pre-treatment state.

We next examined the effects of SMAPs DT061 and DT1154 *in vivo*, in a genetically engineered mouse model of heterogeneous triple negative breast cancer, using different dosing schemes. Lsl-Myc;PTEN<sup>fllox/-</sup>;Blg-Cre mice generate aggressive triple negative tumors (Appendix C1a) that showed intertumoral heterogeneity in histology (Appendix C1b), gene expression patterns (Appendix C1c, d), and intratumoral heterogeneity in differentiation

state marker expression inducing cell-to-cell differences in Cytokeratin 14 (K14) and Cytokeratin 8/18 (K8/18) expression (Fig. 4-2e). DT061 and DT1154 were both effective and inhibiting tumor growth in all tumors, and in all dosing schemes (Fig. 4-2f). To further assess the phenotypic influence of SMAP therapy on these tumors, we used an irradiated-fibroblast co-culture system to establish viable tumor-derived cell lines (Fig. 4-2g). These lines showed similar *in vitro* intratumoral cell-state heterogeneity as the  $lsl-Myc;PTEN^{fllox/-};Blg-Cre$  tumors *in vivo*: cells with distinct K18+, K14+, and K18/K14+ identity coexisted in culture. We treated these lines with DT-1154 and assessed the effects on cell proliferation and surviving cell phenotype at sub-lethal doses. Consistent with the efficacy of DT061 *in vivo*, and the effects of DT1154 on cell line phenotype, these tumor-derived cultures were both sensitive to DT1154 and showed minimal changes in cell-state frequencies at sub-lethal doses of drug (Fig. 4-2h-j).

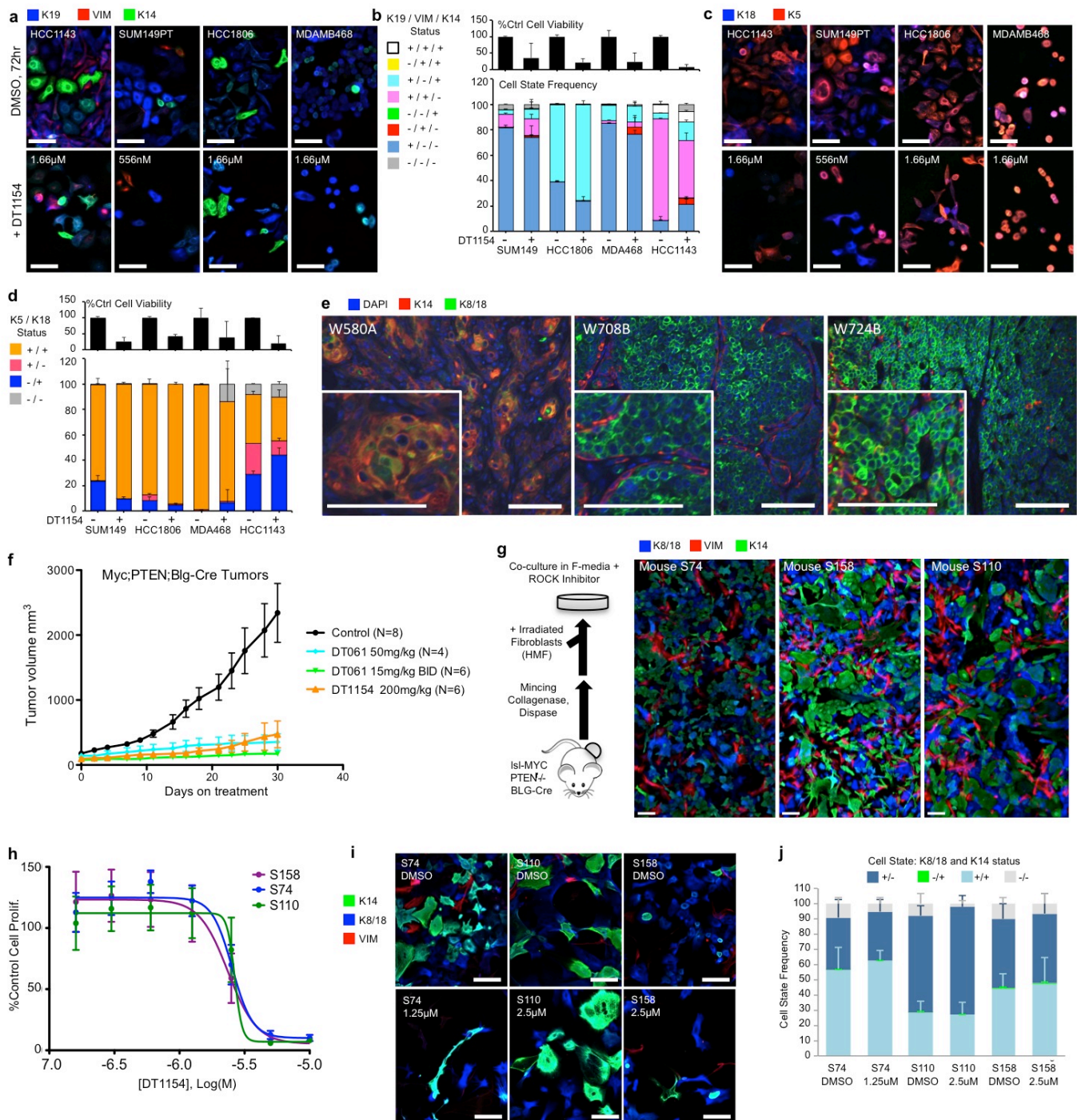


**Figure 4-2: SMAPs effectively kill all differentiation states in heterogeneous TN cell lines and tumor models.**

**(A)** Immunofluorescent images of four basal-like cell lines treated for 72hr with DT1154 at the doses shown (all >IC50) or with DMSO, cells are stained for K19 (blue), VIM (red), and K14 (green), DAPI is not shown, scale bars = 100 $\mu$ M **(B)** Change in cell number and differentiation state frequency is shown in the four cell lines in (A) comparing DMSO to DT1154 treatment with the doses in (A). **(C)** Same as in (A) but stained with K18 and K5. **(D)** Quantitation of cell number and differentiations state as in (B) from images in (C). **(E)** Immunofluorescent images of *Isl-Myc:PTEN<sup>fl/fl</sup>:Blg-Cre* tumors stained with DAPI (blue), K14 (red), and K18 (green), with a higher zoom inset, scale bars = 100 $\mu$ M. **(F)** Graph showing the change in *Myc:PTEN<sup>fllox/-</sup>:Blg-Cre* tumor volume over time following treatment with drug vehicle, DT061 dosed QD at 50mg/kg, DT061 dosed BID at 15mg/kg, or DT1154 dosed weekly at 200mg/kg. **(G)** A schematic showing how *Myc:PTEN<sup>fllox/-</sup>:Blg-Cre* tumor-derived cell lines are established. Tumors are surgically excised, mechanically minced and chemically disaggregated, and grown in co-culture with irradiated human mammary fibroblasts. Immunofluorescent images of three tumor derived cell lines in culture are shown, stained with K8/18, VIM, and K14, DAPI not shown, scale bars = 100 $\mu$ M. **(H)** Graph showing the antiproliferative efficacy of DT1154 in three *Myc:PTEN<sup>fllox/-</sup>:Blg-Cre* tumor-derived cell lines, 72hr treatment. **(I)** Immunofluorescent images of tumor-derived cell lines following 72hr treatment with DMSO or the shown doses of DT1154, cells are stained with K14 (green), K8/18 (blue), and VIM (red), scale bars = 100 $\mu$ M. **(J)** Differentiation-state frequencies based on expression of K8/18 and K14 are shown in tumor-derived cell lines treated 72hr with DMSO or the shown concentration of DT1154.

### 4.3.3 PP2A activators and kinase inhibitors act synergistically to inhibit TN cell proliferation

Both the SMAPs and indirect activators of PP2A (OP449) show promising antitumor efficacy in GEMM models (Appendix C1d). However, tumor regression was not achieved with single agent SMAP therapy and tumors slowly expanded. To improve the efficacy of PP2A activators *in vivo* so that we can achieve tumor regression, we rationalized that activators of PP2A and small-molecule targeted kinase inhibitors may be synergistic when used in combination, as this will reduce the active pool of kinases through increased phosphatase activity, while simultaneously inhibiting the function of the active kinase pool with kinase inhibitors. We used an unbiased drug-screening approach to identify targeted kinase inhibitors that synergize with PP2A activation. Triple negative breast cancer cell lines were either treated with a near-IC50 dose of OP449, or a DMSO control, then grown in multiple 384-well plates containing 7 doses of 119 pathway-targeted therapies. At 72hr we assessed cell viability through the use of a colorimetric assay. After replicate runs in five triple negative cell lines, we found that many targeted agents can enhance the efficacy of PP2A activators including those targeting the PI3K, PKC, AURK, EGFR, JAK/STAT pathways (Fig. 4-3a). In particular we found that targeted antagonists of PI3K pathway signaling, including PI3K, AKT, and mTOR inhibitors were highly effective enhancing antiproliferative efficacy (Fig. 4-3b), and had synergistic relationships ( $<1$ ) with OP449 based on synergy calculations using the Chou and Talalay method<sup>166</sup> (Fig. 4-3c).

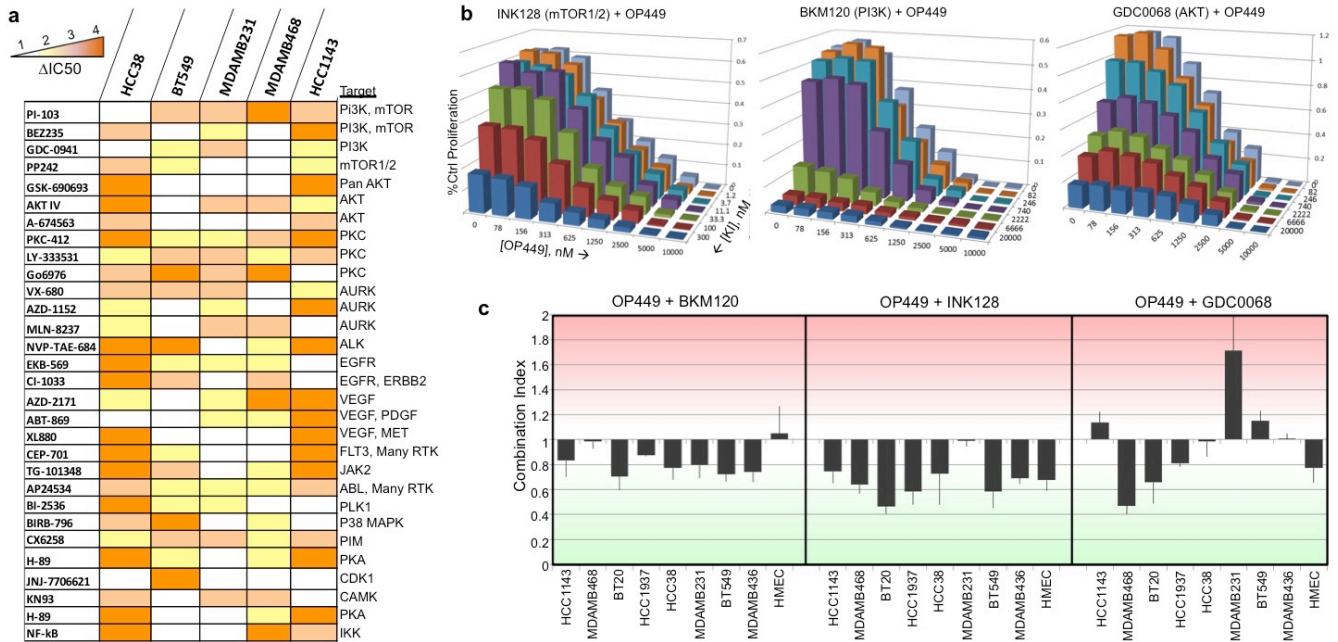


**Figure 4-3: PP2A activators and kinase inhibitors act synergistically to inhibit TN cell proliferation.**

**(A)** A heatmap showing the change in kinase inhibitor efficacy (by fold change in IC<sub>50</sub>) when triple negative cell lines are co-treated with OP449, versus co-treatment with DMSO. Increasing orange color denotes increased combination efficacy. Inhibitor target is shown to the right. N= 3 **(B)** Three dimensional bar plots show the change in cell proliferation when OP449 and the shown PI3K-pathway inhibitors are combined in a drug matrix, representative of three individual runs. **(C)** A bar plot shows the average combination index obtained from triplicate dose-escalation studies using OP449 + BKM120, OP449 + INK128, or OP449 + GDC0068 in 8 triple negative cell lines and one normal line.

## 4.4 Discussion

Triple negative breast cancer is in need of new effective therapies. Currently there are only a few chemotherapeutic drugs that are approved for use in triple negative patients, and while effective at achieving pathological complete responses in approximately a third of TN tumors<sup>49</sup>, most TN tumors are innately resistant to these drugs or acquire resistance during therapy. Many companies are evaluating small-molecule targeted KIs in TN breast cancer, as these tumors commonly have deregulated PI3K, MAPK, and growth factor signaling, however, patient responses to these agents as monotherapy have been poor<sup>14-16,55-57</sup>. Combination therapies add some promise, showing better responses with combination of chemo + KIs, or dual KI therapy, but success is still limited and increased toxicities and adverse medical events often remove patients from these trials<sup>57</sup>. This resilience to targeted and chemotoxic stress is related to the high rates of clonal heterogeneity<sup>21,60</sup> and cell-state heterogeneity in TN tumors (Ch. 2). This can support acquired resistance through Darwinian selection of drug resistant phenotypes. Further, our examination of the antiproliferative and phenotypic influence of a broad set of targeted therapeutics in TN cell lines revealed that most drugs elicited cell-state transitions to drug tolerant persisting states through adaptive chromatin remodeling<sup>67</sup>. These mechanisms of resistance likely drive the poor clinical response of this disease and highlight the need for new therapeutic strategies that are well tolerated and circumvent these mechanisms of resistance.

Pharmacological activators of PP2A may represent a unique solution to this need<sup>128</sup>. PP2A simultaneously regulates the activity of many proliferative and survival pathways including PI3K, ERK, SRC, and MYC signaling, but is commonly down-regulated in cancer cells via mutation, post-translational modification, or increased expression of the endogenous inhibitors of PP2A, SET and CIP2A<sup>126</sup>. Indeed TN tumors show enhanced expression of CIP2A and SET, and low activity of PP2A<sup>128,132</sup>, and we demonstrate here that two distinct therapeutic strategies of PP2A activation are highly efficacious at completely killing TN cell populations *in vitro*. Further, unlike the adaptive cell-state transitions elicited by targeted kinase inhibitors<sup>18,67,175</sup>, we demonstrate that small-molecule PP2A activator DT1154 inhibits TN cell line proliferation, and increases cell death, with no evidence of cell state selectivity or induction of cell-state transitions. Consistent with this, the SMAP DT-061 was highly effective at inhibiting tumor growth in a murine model of heterogeneous triple negative breast cancer. We generated cell line cultures from these mice and again observed that DT1154 could induce 100% cytotoxicity without eliciting differentiation-state change.

These SMAPs were effective *in vivo* and well tolerated by the mice, however, tumor regression was not achieved, and treated tumors still slowly proliferated. To improve the efficacy of these agents we tested the effect of combinations with targeted kinase inhibitors, as this strategy might simultaneously attack the enzymatic function and activation of key kinases in TN tumors. Indeed we found that numerous KIs synergistically enhanced the

efficacy of the PP2A activator OP449, including inhibitors targeting different kinases in the PI3K pathway.

While targeted kinase inhibitors were once believed to hold great promise for the treatment of TN tumors, and initial *in vitro* studies were encouraging, the results coming from recently concluded or ongoing clinical trials are unfortunately showing limited responses in patients. Despite targeting overactive kinases in the tumor cell, numerous intrinsic resistance mechanisms in TN tumors including cell-state heterogeneity and plasticity result in these poor outcomes and highlight the need for new therapeutic strategies. Activators of PP2A offer an orthogonal approach to the suppression of oncogenic signaling pathways in TN tumors by restoring the phosphatase activity of PP2A. These drugs are highly effective *in vitro* and *in vivo* in TN models, and can be further enhanced by simultaneous kinase inhibition. These results have spurred pharmaceutical company interest, and a collaboration between Dual therapeutics and Bristol Meyers Squibb is currently optimizing the pharmacokinetic and pharmacodynamic properties of these SMAPs, which will soon enter clinical trials and hopefully provide a much-needed new tool for TN tumor management.

## 5 Materials and Methods

### 5.1 Cell Lines

All human cell lines were obtained from the American Type Culture Collection (ATCC) other than JIMT1 (DSMZ), SUM149PT (Asterand), and SUM159PT (Asterand). Cell lines were cultured according to supplier protocol with supplemental 10 $\mu$ g/ml penicillin and streptomycin (Thermo) and regularly tested to ensure cultures were negative for mycoplasma. Cell line genotype was confirmed by STR profiling to ensure accurate identity. All lines were maintained at 37°C in a 5% CO<sub>2</sub> atmosphere and cultured at a cellular confluence below 80%.

### 5.2 Reagents

*Primary antibodies:* Cytokeratin 19 (Dako, Clone RCK108), Cytokeratin 14 (Abcam, Clone LL002), Vimentin (Cell Signaling, Clone D21H3), Cytokeratin 5 (Abcam, Clone EP1601Y), Cytokeratin 17 (Thermo, clone E3), Claudin 4 (R&D Systems, clone 382321), Cytokeratin 8 (K8, Abcam, Clone M20), Ku80 (Cell Signaling, clone C48E7), Ki67 (DAKO, clone MIB-1), GATA3 (Cell Signaling, Clone D13C9), Cytokeratin 18 (Cell Signaling, clone DC10). Cytokeratin 8/18 (Fitzgerald)

*Secondary antibodies* (All LifeTech unless noted): goat-anti-mouseIgG1-Alexa647, goat-anti-mouse IgG3-Alexa488, goat-anti-mouseIgG2a-Alexa488, goat-anti-mouseIgG2b-Alexa488, donkey-anti-rabbit-Alexa568, donkey-anti-goat-Alexa647, goat-anti-rabbit-dylight755 (Thermo).

*Small molecule inhibitors*: All drugs, unless otherwise noted, were purchased from Selleckchem including (+)-JQ1 for *in vitro* experiments. BEZ235 was purchased from LC Laboratories and (+)-JQ1 for *in vivo* studies was provided by Jay Bradner at the Dana-Farber Institute of Harvard, Cambridge MA. All *in vitro* inhibitor stocks were solubilized in DMSO and stored as 10mM stock solutions at -80°C. OP449 was provided from Dale Christensen at Oncotide Pharmaceuticals. DT061 and DT1154 were provided by Dr. Goutham Narla at Dual Therapeutics.

## **5.3 Image cytometry and heterogeneity metrics**

### **5.3.1 Image cytometry of primary patient tumors**

All samples were formalin-fixed, paraffin embedded sections of treatment-naïve primary breast tumour samples of hormone-receptor-defined subtypes: luminal (ER<sup>+</sup>/PR<sup>+</sup>/HER2<sup>-</sup>, n=6), HER2+ (ER<sup>-</sup>/PR<sup>-</sup>/HER2<sup>+</sup>, n=3, ER<sup>+</sup>/PR<sup>+</sup>/HER2<sup>+</sup>, n=1), and triple negative (ER<sup>-</sup>/PR<sup>-</sup>/HER2<sup>-</sup>, n=9). Tumor specimens were obtained from three sources: Tumors with multiple analyzed regions (L1-3, H1-3, T1-3) were from surgical blocks obtained from the

OHSU Knight BioLibrary, five samples were core biopsy specimens (L4-6, H4, T4) obtained from the OHSU Knight BioLibrary, and five samples were from a tissue microarray of triple negative breast cancers surgical blocks created under IRB-approved protocols with patient consent from the University of California, San Francisco. With pathologist assistance, areas of high tumour cellularity and low immune infiltrate or stromal density were identified for the focus of immunofluorescent analysis. Cut sections of 5 $\mu$ m were de-parafinized in xylene and passed through a series of graded alcohols. Antigen retrieval was performed in a 0.1M sodium citrate buffer pH 6 (Sigma) under heat and pressure, followed by blocking with a 5% donkey serum (Sigma), 5% goat serum (Vector Laboratories), 1% BSA (Fisher) blocking buffer. Sections were incubated overnight at 4°C with a primary antibody solution against K19 (1:300), K14 (1:300), and VIM (1:200) diluted in 1% BSA, 2.5% donkey serum, 2.5% goat serum. Sections were washed in PBS with 0.1% Tween (Fisher) and secondary antibody staining was performed at room temperature for 1hr with AlexaFluor secondary antibodies against primary host species (1:200, LifeTech) in 1% BSA and 5% animal serum. 1 $\mu$ g/ml 4',6-Diamidino-2-phenylindole nuclear counterstain (DAPI, LifeTech) was added to secondary staining buffers. Surgical specimens were imaged on a Zeiss Axio Microscope capturing 3-by-3 tiled regions (9 images) at 20X magnification. Core biopsies were imaged with single 10x regions, and the TMA was imaged on the Zeiss AxioScan.Z1 platform using 5x5 tiled regions at 10X magnification. All tiled images were stitched in ZenBlue software. TIFFs with original signal were exported for analysis in Cell Profiler<sup>196</sup> software. The Cell

Profiler pipeline included: DAPI smoothing using the Gaussian filter method, primary object identification from smoothed DAPI using the adaptive thresholding Otsu method on default settings, with clumped objects being distinguished and divided using the intensity setting. Primary object area, shape, and DAPI intensity were measured. Primary objects were then expanded a fixed pixel distance, and mean signal intensity for all other channels was measured in this expanded cellular region. Cells touching the image border were excluded from analysis. Spreadsheet outputs were then analyzed in FlowJo software (FlowJo LLC). Single cells were gated by nuclear area and shape, and single cell positivity for K19, K14, and VIM were determined by gating using tumors negative for each marker as controls. Gate shape was optimized to minimize false positivity from nonspecific channel bleed-through. Cell identity was then mapped onto X vs. Y location dot plots called “state maps”, and these digital reconstitutions of cellular phenotypes in the tumor were consistent with visually called phenotypes in tumor images. Regions encompassing normal ductal structures, or DCIS lesions, were identified with pathologist assistance and omitted from analysis.

### **5.3.2 Image cytometry of patient derived xenograft tumors**

Tissue microarray slides with 31 patient derived xenografts and 3 normal breast tissue controls were provided by Mike Lewis at Baylor College of Medicine, Houston TX. Spots were approximately 4mm x 4mm and arranged across three slides. Tumors are described in detail in a separate publication<sup>143</sup> and at [www.bcxenograft.org](http://www.bcxenograft.org), including molecular subtype

and patient ER/PR/HER2 IHC status, mouse passage number for the tumors ranged from 4-8 passages. Slides were prepared and stained as detailed above (Image Cytometry of Primary Tumor Samples) with antibodies against K19 (1:300), K14 (1:300), VIM (1:200), and Ku80 (1:100). Secondary antibodies included the addition of goat-anti-rabbit-dylight755 marking Ku80 nuclei, all 1:200. Slides were imaged on the Zeiss AxioScan.Z1 platform, where circular scan areas were hand-drawn around all TMA spots and regions were imaged as 5x5 tiled regions at 10X magnification, stitched, and exported from ZenBlue software. Images were analyzed in CellProfiler including: DAPI smoothing, primary object identification from smoothed DAPI using the adaptive thresholding Otsu method on default settings, with clumped objects being distinguished using the intensity setting and divided using the propagation setting. Primary object area, shape, mean DAPI intensity and mean Ku80 intensity was measured in this nuclear area. Primary objects were then expanded a fixed pixel distance, and mean signal intensity for all other channels was quantified in this expanded cellular region. Cells touching the image border were excluded from analysis. Spreadsheet outputs were then analyzed in FlowJo software. Single human tumor cells were gated based on positivity for Ku80, and single cell positivity for K19, K14, and VIM were determined by gating, using tumors negative for each marker as controls. TMA regions with compromised tissue fidelity were omitted from the analysis. HCC70 xenografts (Fig. 6) were imaged on the Zeiss Axio platform and analyzed using this method.

### 5.3.3 Image cytometry of cancer cell lines

Cancer cell lines were plated in appropriate media and allowed to adhere overnight, followed by various experimental treatments. At endpoint, cells were fixed by adding equal volume of 4% paraformaldehyde (Electron Microscopy Sciences) solution with 1mM MgCl<sub>2</sub> (Sigma) to the well media. Wells were then washed with PBS and permeabilized in a 0.3% Triton-X100 solution (Thermo). Primary antibodies were diluted in PBS with 2% BSA and incubated overnight at 4°C. Cells were subsequently washed with PBS-Tween and incubated 1hr at room temperature in a secondary labeling solution including 1µg/ml DAPI and combinations of secondary antibodies against primary host species (1:300 in 2%BSA). Wells were then washed with PBS-Tween, filled halfway with PBS, and either imaged immediately or stored at 4°C. Cell imaging for Figure 1-4 was performed on the Olympus ScanR Platform at 10X magnification capturing 4 images per well in 384-well plates, and 9 images-per-well in 96 well plates. Single-cell nuclear and cytoplasmic fluorescent intensities were calculated using the Olympus ScanR Analysis Software: the DAPI-positive region of each cell was used as a boundary to quantitate nuclear signal, and a 10pixel annulus around the nucleus was used to quantitate cytoplasmic signal, omitting nuclear signal. Cells touching the border of the image were removed from analysis. Imaging for Fig. 2d, and Fig. 5 and 6 was performed on the INCELL 6000 platform (GE Biosciences) using the GE INCELL Analyzer analysis software to calculate cytoplasmic and nuclear signal in identical methodology as described above. FlowJo analysis software was used to identify cell phenotype. Marker positivity was defined using

marker-negative controls, which including VIM/K14-negative luminal B cell lines, and K14/K19-negative claudin low lines for cell line phenotyping (Fig. 1i). “High” expression was defined as mean-cell mean-fluorescent-intensities exceeding the in mean-cell MFI in DMSO wells. For image presentation in the figures the same image brightness and contrast settings were applied across all experimental samples and conditions within an experiment.

### 5.3.4 Calculating heterogeneity

The Shannon diversity index is used as a metric of cell-state heterogeneity throughout this work. Cell state frequencies were calculated using flow cytometry software (FLOJo) as described above. For each tumor, patient derived xenograft, or cell line, the proportion of each cell state was calculated by dividing cell state number by the total cell number in the population ( $P_i$ ). The Shannon diversity index ( $H'$ ) was then calculated by multiplying  $P_i$  by the natural log of  $P_i$ , for each cell state, then summing these numbers.

$$H' = - \sum_{i=1}^S p_i \ln p_i$$

## 5.4 Gene expression analyses

### 5.4.1 Cell line expression analysis

In Fig. 2-3, publically available breast cancer cell line gene expression data<sup>144</sup> was queried for the expression of three sets of 20 genes preferentially expressed in luminal and myoepithelial cells, identified by sorting experiments in normal breast tissue<sup>51,103,117,118,141,145,146</sup>, as well as 20 mesenchymal/EMT-transition genes<sup>142,147,148</sup>. Pearson coefficient clustering and heatmap generation was performed using GENE-E software (Broad Institute). Cell line subtype was determined through previously described 4-class (Luminal, Basal-like, Claudin-low, HER2+) intrinsic subtyping<sup>13</sup>.

### 5.4.2 RNA-sequencing

Two RNAseq runs were analyzed in this dissertation and presented in Chapter 3, and will be detailed separately. RNA sequencing data presented in Fig. 3-1 to 3-3 was obtained as follows: Total RNA was isolated with TRIzol (Invitrogen) from HCC1143 cells following treatment with PBS + 0.05% DMSO (Sigma), 1 $\mu$ M Trametinib, 1 $\mu$ M BEZ235, or 1 $\mu$ M of both agents in combination (1:1), following a 6 day incubation with d drug replenished at day 3. cDNA libraries were generated using the Agilent SureSelect Strand Specific RNA kit (Agilent) using 150ng total RNA input and following the manufacturers protocol. cDNA Libraries were sequenced on the Illumina HiSeq 2000 using 50bp single end reads, grouping

8 samples per lane. Base calling was performed using Illumina RTA (v1.13.48) and conversion to FASTQ was performed using CASAVA (v1.8.2, Illumina). Reads were then trimmed to 44 bases, discarding the first 4 bases, the next 44 bases were kept. Trimmed reads were aligned to the hg19 genomes using Bowtie software (v1.0.0) allowing up to 3 mismatches and require best unique matches. Custom R scripts were used to count tags that aligned to the exons of UCSC RefSeq gene models to calculate RPKM values.

For the second RNAseq analysis presented in Figure 3-5, HCC1143 cells were treated in triplicate with 1 $\mu$ M Trametinib, 1 $\mu$ M BEZ235, 1 $\mu$ M JQ1, Trametinib + JQ1, BEZ235 + JQ1, or a DMSO control for 72hr. Total RNA was isolated using the QIAGEN RNeasy mini kit according to manufacturer instructions. RNA was run on the Bioanalyzer (Agilent) to verify integrity. cDNA libraries were constructed with the Illumina Truseq Sample Prep Kit v2 according to manufacturers instructions, using 150ng of total RNA input. cDNA libraries were sequenced on the NextSeq500 using 75bp single-end reads, grouping 9 samples per lane. Base calling was performed using Illumina RTA (v2.4.11) and de-multiplexing and conversion to FASTQ was performed using Bcl2fastq (v2.17.1.14, Illumina). Reads were then trimmed to 44 bases, discarding the first 4 bases, the next 44 bases were kept. Trimmed reads were aligned to the hg19 genomes using Bowtie<sup>197</sup> software (v1.0.0) allowing up to 3 mismatches and require best unique matches. Custom R scripts were used to count tags that aligned to the exons of UCSC RefSeq gene models to calculate RPKM values. All RNAseq

FASTQ and RPKM .txt files can be found on the GEO omnibus under accession number GSE82032.

### 5.4.3 Geneset enrichment analysis

All genesets analyzed in Chapter 3 are available online<sup>67</sup>. Genesets present in the molecular signature database (MSigDB, Broad Institute) were taken as is and are available at [www.broadinstitute.org/gsea/msigdb/collections.jsp](http://www.broadinstitute.org/gsea/msigdb/collections.jsp). A collection of 32 breast phenotype-related genesets was compiled and included genesets from study examining overlap in gene expression from historical mammary gland population-sorting experiments<sup>98</sup>, a study examining intrinsic subtypes of breast cancer<sup>161</sup>, a study profiling the claudin-low subtype of breast cancer<sup>38</sup>, a study examining classical myoepithelial markers<sup>141</sup>, and study examining the epigenetic determinants of the human breast<sup>103</sup>. A second compilation including 25 chromatin modifier enzyme activity-related genesets was compiled from MSigDB as well as a study examining BRD4 binding sites in basal-like breast cancer cell lines<sup>168</sup>, a study examining gene expression changes following ectopic BRD4 expression in a mammary cancer line<sup>167</sup>, and a study examining gene expression changes following ectopic expression or knockdown of EZH2<sup>72</sup>. A final set of 13 transcription factor activity-related genesets was compiled from MSigDB genesets and studies examining ectopic FRA1 expression in breast cancer cell lines, ectopic GATA3 expression in MDAMB231 cells, ZEB1 overexpression and knockdown in lung cancer cell lines, and a study examining change with ectopic expression of SNAI1 in the

transformed breast cell line MCF10A<sup>173</sup>. To reduce geneset size for optimal GSEA results, genesets were compiled of the most statistically significant upregulated or down-regulated genes, limiting size to 500 genes. Genesets generated from Affymetrix DNA microarray experiments used the NetAffx Query tool for Affymetrix gene ID conversion (Affymetrix.com).

## **5.5 Measuring drug efficacy**

### **5.5.1 Therapeutic screening and synergy analysis**

Drug screening plates used in Fig. 3-1 and Fig. 4-3 were designed and created as previously described<sup>198</sup>. Briefly, 96-well master plates with 7-point dilutions of 119 inhibitors at 10x concentration were plated into three, 384-well plates at 5ul drug per well using the EP Motion automated dispensing system (Eppendorf). Control wells with equal volumes of DMSO (Sigma) were also included. 384-well plates are kept at -20°C until use, at which point they were thawed for 1 hour at 37°C and spun down at 800g. Cells were plated directly into warm drug plates using EP Motion (Eppendorf) automated pipettor in 50uL media. Plates were sealed with AeraSeal (Excel Scientific) and incubated for 72hr at 37°C in a 5% CO<sub>2</sub> atmosphere. The CellTiter 96 kit was used at to measure cell viability, calculated as a percent of proliferation comparing experimental values to a negative control (DMSO), after subtracting positive control signal (cell-free media). The FDA-approved cytotoxic

therapy screen (Supplementary Fig. 17b) was constructed as previously described<sup>19</sup>, containing agents purchased from Cayman, Sigma and Selleckchem, and analyzed as described above. Follow up experiments, including all other dose-response curve generating experiments in this work, were performed in 384 or 96-well plates using the CellTiter 96 kit, with each condition run in triplicate wells, placed in distinct areas of the plates to normalize for edge effects. Combination indices (CI) were calculated from replicate, fixed-ratio, dose escalation experiments using the Chou and Talalay method<sup>166</sup> with Compusyn software (Combosyn). CI values were reported at 75% and 90% inhibitory values (CI75, CI90, respectively).

### **5.5.2 Cell death assays**

Cells were plated and allowed to adhere overnight. The next morning cells were treated with inhibitors and incubated with 250nM YOPRO1 dye (Thermo). Time course imaging was performed on the IncuCyte ZOOM Live Cell Imaging System (Essen Bioscience), taking phase images and green channel fluorescence images every 12 hours throughout the a 72hr treatment course. Green objects per image were quantified in the Incucyte software. Total cells per image were measured from phase images using a custom Cell Profiler pipeline. Briefly, this pipeline included: Color to gray image conversion, edge enhancement using the LoG method, image smoothing using a Gaussian filter setting, and primary object (cell)

identification using the automatic threshold strategy and distinguishing and dividing clumped objects by intensity.

### **5.5.3 Cell cycle analysis**

Cells were plated in six identical plates and allowed to adhere overnight. The next morning all plates were treated identically with inhibitors, and one plate was incubated with 5-Ethynyl-2'-deoxyuridine (EdU, Sigma) for 12 hours at a concentration of 10 $\mu$ M. At the 12-hour mark, this plate was fixed, and EdU was added to a second plate. Every 12 hours a subsequent plate was fixed and another was pulsed with EdU to capture the next timepoint. Cell fixation and permeabilized were carried out as described above (Image Cytometry of Cancer Cell Lines). Wells were then treated with a reaction buffer containing 2mM CuSO<sub>4</sub> (Sigma), 8 $\mu$ M AlexaFluor Azide 647 (LifeTech), and 100mM sodium ascorbate (Sigma) in PBS and incubated 1hr. After washing with PBS, cells were stained for K19, K14, and VIM, imaged, and analyzed as outlined above (Image Cytometry of Cancer Cell Lines) using nuclear detection of 647-channel signal to quantify cellular EdU levels.

## **5.6 Computational modeling**

This section will briefly explain the generation of the computational model to assess drug-induced cell state dynamics of HCC1143 cells under two distinct hypothesis, Darwinian

selection, or transition-mediated state enrichment, presented in Figure 3-3. Further explanation of the mathematics and programs used to run the model are available in Appendix A. The data to construct the model was from measurements of total cell number, number of cells in each state, and number of cells dying using a the YO-PRO1 assay described above in 15 replicate wells taken every 12 hours over a 72-hour horizon (Fig. 3-3a, d). These models assumed that each cell at each instant could be either dead or alive, and if alive, expressed either  $K14^{hi}$  or  $K14^{low}$ . Under each hypothesis, the number of  $K14^{hi}$  live cells,  $K14^{low}$  live cells, and dead cells over time under drug treatment were estimated based on state-selective death criteria. For example, for the  $K14^{hi}$  Darwinian selection scenario, the number of  $K14^{hi}$  live cells under Trametinib was set to the measured  $K14^{hi}$  cell count, whereas the number of  $K14^{low}$  live cells under Trametinib was set to the measured  $K14^{low}$  cell count minus the estimated dead cell count (Appendix A). The number of dead cells was estimated by multiplying measurements of cell death proportion and population total (Supplementary Note). Under both hypothesis, the quantities of  $K14^{hi}$  and  $K14^{low}$  live cells over time under DMSO were estimated by distributing death equally between the measured  $K14^{hi}$  and  $K14^{low}$  cell counts (Appendix A). The time course training data for each hypothesis-agent pair (e.g.  $K14^{hi}$  Darwinian selection and Trametinib) were fed into a constrained  $l_2$ -regularized least-squares program with alternating minimization (as some measurements were illegible) to learn locally optimal dynamics (CVX optimization package<sup>199</sup>). Linear time-invariance was assumed because additional complexity was expected to overfit the data (Appendix A). Model parameters are time-averaged rates of division,

death, and transition of K14<sup>hi</sup> and K14<sup>low</sup> live cells; refer to Chapman et al. for details<sup>200</sup>. In the optimization program, these parameters were constrained according to hypothesis-specific assumptions on cell-state transition and death. Under the K14<sup>hi</sup> Darwinian selection scenario, for example, Trametinib-induced rates of cell-state transition and K14<sup>hi</sup> death were set to zero (Appendix A). Evolution of HCC1143 cell populations following drug treatment (or DMSO) was simulated by propagating the hypothesis-specific models forward in time from appropriate initial conditions. The initial condition for each drug treatment simulation was the number of K14<sup>hi</sup> live cells, K14<sup>low</sup> live cells, and dead cells in each drug-treated well estimated at time zero. The initial condition for the baseline simulation was the average of such numbers over all DMSO wells. Change in subpopulation proportion (vs. DMSO) was computed from the simulated evolution of HCC1143 cell populations over time (Fig. 3-3h, 3-3e, Appendix A). MATLAB software (MathWorks) was used for all computational modeling.

## 5.7 VIPER analysis

The gene expression (raw counts) was normalized by the library size (total number of reads mapped to transcripts) and transformed to stabilize the variance by fitting the dispersion using a negative-binomial distribution as implemented in the DESeq package from Bioconductor<sup>201</sup>. To reduce the impact of systematic variability, affecting mainly low expressed genes, we focus our analysis only on mid-to-high expressed genes. The threshold

to identify low expressed genes was defined by the data as follows: we fit a mixture of two Gaussian models to the probability density of expression, and used them to compute the likelihood ratio (LR) of high expression. Low expressed genes ( $LR < 1$ ) were not considered for further analysis. While this procedure trimmed the expression profile to 10,313 genes, it should not affect the quality of VIPER results, as we have previously shown the analysis is strongly robust to partial signature representation<sup>164</sup>. Gene expression signatures were computed by comparing each perturbed sample vs. DMSO vehicle control. The VIPER algorithm, available from Bioconductor (<http://bioconductor.org/packages/release/bioc/html/viper.html>) was then used to estimate the relative activity of 5,087 regulatory proteins, including transcription factors and signaling proteins. This analysis was based on a transcriptional regulatory model assembled by the ARACNe algorithm<sup>202</sup> from 1,047 breast carcinoma tumours profiled by The Cancer Genome Atlas (TCGA). The regulatory model is available from figshare (<https://dx.doi.org/10.6084/m9.figshare.2750698>). Top upregulated and Down-regulated VIPER hits were analyzed with DAVID pathway ontology analysis against the KEGG, BIOCARTA, REACTOME, and PANTHER databases. All VIPER results are present in Supplementary Table 3.

## 5.8 Single cell ATAC-seq library construction and analysis

Single cell combinatorial indexing ATAC-seq libraries were prepared following the exact protocol described in Cusanovich et. al. 2015<sup>170</sup> using flow sorting at each stage of nuclei partitioning as opposed to dilution. All treatments were multiplexed in the same transposase-based indexing plate with the wells of the plate corresponding to each treatment condition. Indexing at this level has the distinct advantage of preventing any potential cell collisions from occurring between cells from two separate conditions as the treatment condition is encoded in the transposase barcode prior to pooling and redistribution. After combinatorial indexing library construction, all PCR wells were pooled and assessed on a Bioanalyzer High Sensitivity DNA chip (Agilent) prior to sequencing on an Illumina NextSeq 500 according to protocols outlined in Amini et. al. 2014<sup>203</sup>. Sequence reads were demultiplexed using SCI-seq software provided in Vitak et. al. 2017<sup>204</sup> prior to alignment using bowtie2<sup>197</sup>. PCR read duplicates were removed on a cell-level basis, again using SCI-seq software. Index combinations were then filtered to exclude background reads and to only retain those containing at least 1000 uniquely aligned sequence reads with a mapping quality of at least 10. The combined alignment file was then used for peak calling using MACS2<sup>205</sup> with default parameters. Reads and peaks were then used to construct a counts matrix as described in Cusanovich et. al. 2015<sup>170</sup> and filtered to retain only cells with at least 1000 on-target reads, and sites that contain reads from at least 50 cells which was then used to perform latent semantic indexing (LSI), retaining dimensions 1 through 15. On the LSI matrix we then

carried out t-distributed Stochastic Neighbor Embedding (t-SNE)<sup>206</sup>. To compute transcription factor deviation scores we used chromVAR<sup>171</sup> using the transcription factor motif collection provided by the tool and plotted deviation z-scores on the respective LSI t-SNE visualizations.

## **5.9 Animal studies**

All mice were handled in accordance with the OHSU Institutional Animal Care and Use Committee (IACUC) guidelines.

### **5.9.1 Assessing JQ1 + BEZ235**

A total of  $2 \times 10^6$  HCC70 cells in 50% Matrigel (Corning) + 50% complete media (RMI1640 + 10% FBS) were bilaterally injected into the left and right fourth mammary glands of 4-6 week old nonobese-diabetic (NOD)/SCID/ $\gamma$ -chain null (NSG) mice. Tumours were allowed to grow until tumours reached  $100\text{mm}^3$ , at which point all mice were randomized into treatment groups. Each group included four mice, with a total of eight tumors per group, based on other xenograft studies this was sufficient to detect mean differences in tumor size between groups greater than 1 standard deviation at 5% significance (using two-tailed student's t-test) with 95% power. Following randomization, treatment commenced with the following agents: 40mg/kg NVP-BEZ235 by oral gavage (OG), 50mg/kg JQ1 by

intraperitoneal injection, a combination of the two agents, or OG control vehicle (10% 1-methyl-2-pyrrolidone/90% PEG300) and IP vehicle (10% DMSO in 2-Hydroxypropyl- $\beta$ -cyclodextrin, 10% w:v in water). Treatments were performed once daily, for 21 days. Single agent cohorts received vehicle by OG (JQ1 cohort) or vehicle by IP (BEZ235 cohort). Caliper measurements and tumour volume calculations were performed every 2-3 days using the  $V = (L \times W^2)/2$  equation. Mice were euthanized following the 21-day treatment period according to IACUC protocol and tumors were harvested, formalin fixed, paraffin embedded, sectioned and immunofluorescently interrogated (see Analysis of primary tumor samples). Investigators were not blinded when assessing tumor volumes and were blinded during immunofluorescent analysis.

### **5.9.2 SMAP studies in *Lsl-Myc:PTEN<sup>fl/fl</sup>:Blg-Cre* mice**

Blg-Cre mice were crossed with ROSA26-Floxed-Stop-Myc mice (RFS-Myc). These Blg-Cre:RFS-Myc mice were then crossed with *PTEN<sup>fllox/-</sup>* mice received from Dr. Akira Suzuki. Blg-Cre:RFS-Myc, *PTEN<sup>fllox/-</sup>*, and Blg-Cre:RFS-Myc:*PTEN<sup>fllox/-</sup>* female mice were then allowed to complete two cycles of pregnancy and lactation at which point they were examined for tumor development twice per week by palpation. Once tumor size reached a diameter of 5mm by caliper measurement, mice were enrolled into study and randomly assigned into one of four treatment groups: 1) Vehicle (1:10 Solutol and 1:10 N,N-Dimethylacetamide in H<sub>2</sub>O ) administered BID by oral gavage. 2) 50mg/kg DT061

administered BID by oral gavage. 3) 15mg/kg DT061 administered BID by oral gavage. 4) 200mg/kg DT1154 administered BID by oral gavage. All treatments were for 30 days, tumors were measured by caliper every other day, tumor volume was calculated as

$$V=1/2(\text{Length} \times \text{Width}^2)$$

### 5.9.3 Tumor-derived cell line establishment

Tumors were surgically resected from Blg-Cre:RFS-Myc:PTEN<sup>flox/-</sup> mice and mechanically chopped into pieces approximately 1-2mm in size. Tumor pieces were then transferred to a Erlenmeyer flask with magnetic stir bar and incubated in an enzymatic disaggregation solution for 20 minutes: 2.5 mg/mL collagenase (Worthington), 0.1 mg/mL DNase I (Sigma), 1.0mg/mL hyaluronidase in EBSS (Worthington); 0.45 uM filter-sterilized.

Tumor slurry was then strained through a 70uM filter into a 50ml collection vial and put on ice. Remaining tissue in the filter was then transferred back to the Erlenmeyer flask and incubated with TrypsinLE at 37deg. C for 10 minutes. Slurry was then strained through a 70uM filter and added to the 50ml collection vial. Cells were spun down at 300xG for 5 minutes. Liquid was aspirated from the pellet and the cell pellet was reconstituted in 4mL “F” media (detailed below). 1ml of cells was added to a P100 dish with 1E6 irradiated human mammary fibroblasts (irradiated fibroblasts were provided by Dr. Ellen Langer at Oregon Health and Science University). Cell cultures were monitored for growth, when epithelial

colonies (marked by cuboidal morphology) gained 80% confluence, cells were passaged. During passaging, cultures are washed with PBS, then incubated in 1mL 0.25% TrypsinLE trypsin for 1min, this mL trypsin of trypsin is then aspirated and primarily contains fibroblasts. Remaining cells are then washed with 1mL PBS, and 1mL fresh trypsin is then added and allowed to incubate for 5min at 37deg. C. Cells are then triturated and split 1:4 into new P100s with the addition of 1E6 irradiated HMFs per p100. For in vitro drug assays, irradiated fibroblasts are again selectively trypsinized and discarded, cells are washed, then trypsinized and plated into 96-well microplates at 5000 cell/well without additional fibroblasts.

## **5.10 Statistical analysis**

All statistical analyses were performed using GraphPad Prism software (V5, GraphPad Software Inc). Data is presented as mean with standard error when showing averages across biological replicates, or mean with standard deviation within representative experiments, all experiments were repeated at least three independent times. The number of replicates was chosen based on prior knowledge of specific experimental variability. For determining significance, replicate data was first tested with the D'Agostino & Pearson omnibus normality test. Normally distributed data was compared with the two-tailed students T-test, or paired student's T-test for paired data. Non-normally distributed data was compared using the Mann-Whitney test, or the Wilcoxon matched-pairs signed rank test for paired data.

## 6 Conclusions and Future Directions

Breast cancer is a heterogeneous disease with pronounced differences between patient tumors. Systems have been established to better classify the intertumoral heterogeneity of the disease, and the creation of breast tumor subtypes based on shared patterns of gene expression and molecular features has aided in the identification of targeted therapies that are effective against particular subtypes. However, some tumor subtypes, like triple negative breast cancer, lack shared features that can be exploited for therapy. Further, TN tumors also possess high levels of intratumoral heterogeneity on a genomic and phenotypic level, and these tumor cell phenotypes are plastic, allowing both Darwinian selection and adaptive resistance to occur during treatment. These properties make TN tumors particularly resistant to single agent therapeutics, and the initial results of clinical trials using single agent small molecule kinase inhibitors indeed show poor responses in TN patients<sup>14–16,55–57</sup>.

### 6.1 Improving clinical assessment of intratumoral heterogeneity

To improve the treatment of heterogeneous and plastic tumors, we must first develop and implement diagnostic systems that can identify heterogeneous tumors. Multiregional sequencing of surgically resected tumors has been proven to be an effective method to characterize the clonal heterogeneity within in a tumor<sup>21,60,207</sup>, however, this method requires

removal of the tumor and cannot predict the genotype of residual disease. Alternatively, circulating tumor DNA represents a useful source of genomic information that can be collected less invasively<sup>208</sup>, and longitudinally, in order to monitor clonal evolution in the tumor<sup>209</sup>.

Techniques to profile cell-state heterogeneity in tumors include immunohistochemical analysis of tissue slides, flow or mass cytometry from tumor cell suspensions, or single cell epigenetic or transcriptomic profiling of tumor cells, all of which require significant tumor mass for evaluation. Immunohistochemical analysis may represent the easiest procedure to implement into current clinical practice, as collection of FFPE tissue sections is already standard practice for histological assessment. In this work I present a system that can use this tissue source to measure intratumoral phenotypic heterogeneity by multi-color immunofluorescence staining and automated image analysis. We demonstrate that phenotypic heterogeneity can be quantified using the Shannon diversity index, which allowed for comparisons of intratumoral phenotypic heterogeneity amongst different molecular subtypes and tumors of different hormone and HER2-receptor expression status. This study demonstrated that the triple negative and basal-like subtypes have the highest levels of cell-state heterogeneity, while luminal tumors have the lowest. And while the number of patient samples examine in the study was low, these results nonetheless demonstrate the potential of immunofluorescent image cytometry systems to quantify differences in tumor heterogeneity between, and within subtypes. Improving this heterogeneity assay by including expanded sets

of cell-state markers and refining cell segmentation strategies will improve the ability to quantify cell-state heterogeneity. Applying this system to large tumor cohorts with known patient treatment data and clinical outcomes may reveal the utility of this heterogeneity metric to diagnose disease, predict outcomes, and guide treatment decisions.

## **6.2 Rethinking current treatment paradigms for heterogeneous tumors: moving towards “management”, not cures**

Intratumoral clonal heterogeneity, intratumoral cell-state heterogeneity, and cell-state plasticity are major challenges in our ability to therapeutically manage triple negative tumors. Tumor clones or phenotypes can sometimes function symbiotically if they have complementary paracrine signaling<sup>210,211</sup>, but there is mounting evidence that clonal heterogeneity produces competition for resources within the tumor, which can be an inhibitory force on tumor growth and metastasis<sup>212</sup> and can even result in tumor collapse<sup>211</sup>. Therefore, the current paradigm of using maximum tolerated doses (MTD) of cytotoxic therapy in order to enact complete cell kill and “cures” can be more detrimental to patient outcomes than using no treatment at all. Breast tumors, and TN tumors in particular, are a heterogeneous mixture of tumor clones and phenotypes with distinct environmental fitness and drug sensitivities, all of which compete for a limited pool of nutrients, oxygen, and territory. Curative strategies often eliminate all chemosensitive cells in the tumor, removing

the competitive landscape that keeps the drug resistant, and often more aggressive and metastatic tumor subpopulations at bay<sup>159,212,213</sup>. This “competitive release”<sup>214</sup> provides the proper environment for aggressive drug-resistant clones to now overtake the tumor, and leaves few strategies to combat the growth of the remaining disease. These selected clones or phenotypes often harbor distinct genetic or phenotypic features that make them broadly resistant to therapy, such as selection of clones with P53 mutations that have enhanced resistance to stress-induced apoptosis<sup>215</sup>, or selection of cell state that have high expression of multi-drug resistance (MDR) transporters, reducing the efficacy of many therapeutic agents through increased drug efflux<sup>216,217</sup>. Triple negative patients have a unique attribute that tumors that become resistant to neoadjuvant chemotherapy have worse overall survival than other subtypes that progressed on treatment<sup>7</sup>. This is consistent with the idea that due to intratumoral heterogeneity in this subtype, strategies attempting curative neoadjuvant chemotherapy with maximum tolerated dosing may actually put the patient at great risk if unsuccessful. Consistent with this, studies using mathematical modeling of tumor evolution under different therapeutic pressures demonstrate that selection of resistant clones through MTD therapy is an ineffective strategy for heterogeneous tumor management, and leads to outgrowth of aggressive phenotypes with increased metastatic potential<sup>212,218,219</sup>

Due to the implications of intratumoral heterogeneity, we must re-strategize our approach to manage these tumors. Instead of using maximal doses of therapy in attempts to achieve a cure, we must appreciate the competitive landscape of clonal and phenotypic

subpopulations vying for resources within the tumors and use lower, more intermittent doses. Supporting this, the implementation of breaks in treatment, or “drug holidays”, have been shown to allow the tumor to regain therapeutic sensitivity, improving response with the next dose, and slowing down the acquisition of drug resistance<sup>24,138,220</sup>. These findings were discovered in melanoma, but a recent study by Gomez-Miragay et al<sup>78</sup> in triple negative breast cancer demonstrates that expanding the period between chemotherapy treatments improves responses in patient-derived breast tumors.

### **6.3 New approaches to treat heterogeneous and plastic breast tumors**

In addition to improving current treatment regimens by altering dosing and dose intervals, the development of new therapeutic approaches can greatly benefit TN tumor management. In this work we highlight the pitfalls of single agent kinase-targeted therapeutics in heterogeneous and plastic breast cancers like TN breast cancer. Small molecule kinase inhibitor monotherapies show some antiproliferative efficacy in TN models, but consistently generate a drug-tolerant persisting cell population. We demonstrate that this is the result of adaptive cell-state transitions, supported by chromatin modifier protein activity and changes in the open chromatin architecture. Consistent with this, inhibiting BET protein activity prevents these drug-induced chromatin changes, and maintains the cells in a kinase-inhibitor-

sensitive state. Accordingly, combination treatment with the mTOR/PI3K inhibitor BEZ235 and the BET inhibitor JQ1 robustly induced cell death *in vitro* and tumor regression *in vivo*<sup>67</sup>. This strategy of combining a plasticity-promoting kinase inhibitor with an inhibitor of adaptive chromatin remodeling has proven to be an effective option to treat phenotypically heterogeneous and plastic tumors, and is supported by numerous recent studies examining different KI/BETi combinations<sup>18,123,124</sup>.

Small molecule activators of PP2A (SMAPs) represent an orthogonal approach to treating heterogeneous and plastic breast tumors. Pharmacological reactivation of PP2A in breast cancer cells results in profound cell death in many cancer types, and we demonstrate that these effects are shared across different cell states in heterogeneous triple negative breast cancer models. This is due to the wide range of kinases and other proteins that are regulated by PP2A, including MYC, AKT, RAF, ERK, SRC, and BAD, amongst many others. Unlike multi-targeted kinase inhibitors, these SMAPs are well tolerated in normal cells, with no adverse side effects being observed in our treated animal models. This class of drugs shows promise for treatment of heterogeneous and plastic breast cancers and may provide an effective strategy to alternate with KI/BETi combinations, or to use in the case of innate or acquired resistance to KI/BETi therapy.

### 6.3.1 Advancing Kinase Inhibitor and BET inhibitor combination therapy

The BET family, and more particularly, BRD4, is an effective target to inhibit adaptive state changes and improve kinase inhibitor efficacy. This is due to BRD4's role in multiple steps of allowing new genes to be expressed in a cell: supporting chromatin architecture changes, *de novo* enhancer formation, and transcriptional elongation. BRD4 can acetylate histones in a Histone 3 globular domain lysine residue, K122, which stimulates nucleosome eviction from DNA, resulting in changes in open chromatin and allowing new gene enhancer or promoter access<sup>125</sup>. Further, BRD4 also has well-studied epigenetic reader functions, where its two bromodomains are used to bind acetylated lysine residues on histones and allow for mediator complex docking, and chromatin looping of this enhancer machinery to the transcriptional start site (TSS) of target genes<sup>221,222</sup>. Once looped to the TSS, BRD4 further functions as a kinase in Positive Transcription Elongation Factor b (P-TEFb) complex, functioning to phosphorylate the C-terminal domain of RNA Polymerase II, stimulating the release from transcriptional pause and elongation of RNA synthesis<sup>105,106</sup>. Due to the many roles that BRD4 plays in *de novo* enhancer formation and gene expression it may be the ideal therapeutic target to inhibit adaptive resistance. However, BRD4's involvement in these many mechanisms may make its pharmacological targeting less tolerable in normal cells of the body. Indeed some side effects of BET inhibitors are observed in animal models and in early clinical trials, including a reduction of secretory cell functions (pancreatic  $\beta$ -cells), adipocyte counts, and differentiated immune cells presence in animal models treated with BET

inhibitors<sup>223</sup>. Related to these cell-level changes, we observe side effects of increased diarrhea, hyperbilirubinemia, and reductions in blast counts in human patients treated with the BET inhibitor OTX015 in Phase Ib trials<sup>224</sup>.

It will be important to understand what mechanisms are antagonized by BET inhibitors during the prevention of adaptive resistance to kinase inhibitors. Our work demonstrates that changes in open chromatin architecture, survival-signaling gene expression, and state-transition are all inhibited when JQ1 is dosed with BEZ235. These effects could result from the repression of open chromatin change, the repression of *de novo* enhancer formation, the repression of P-TEFb function and transcriptional pause-release, or a complex combination of these mechanisms. To better understand the contribution of these mechanisms we can use sciATAC-seq to test whether the newly opened chromatin sites during drug response are at known gene enhancer locations of genes that increase expression during KI treatment. This can be performed by performing sciATA-seq in cell lines that have had their gene enhancer locations mapped\* on the ENCODE database<sup>225</sup>, such as SUM149PT, for which we also have RNA-seq data following drug treatment with BEZ235 and Trametinib. This will allow us to determine if gene expression changes are linked to the opening of enhancers. We could employ chromatin immunoprecipitation (ChIP) using anti-BRD4 antibodies to show that upregulated genes have BRD4-bound enhancers in KI-treated

---

\* Various assays including 5C, ChIA-PET, and Hi-C are used to determine what enhancer regions connect to what promoter regions.

cells, but not in KI/BETi-treated cells, which would support a gene-enhancement role for BRD4, particularly if BRD4 was present at promoters as a factor in P-TEFb in both treatments. Assays that examine nascent gene transcription, such as the global run-on sequencing assay (GRO-seq)<sup>226</sup> or precision nuclear run-on and sequencing assay (PRO-seq)<sup>227</sup>, could also be combined with CHIP at earlier timepoints to demonstrate that BRD4 is localizing to gene enhancers or gene promoters where nascent transcription is occurring. Higher prevalence of BRD4 at enhancers would argue for an enhancer-mediated mechanism of BRD4-supported gene expression, whereas more prevalence of BRD4 at gene promoters would argue for a P-TEFb-mediated mechanism of BRD4-supported gene expression. Further, examining whether pharmacological inhibitors of chromatin modifier proteins, and/or P-TEFb complex member inhibitors in combination with kinase inhibitors phenocopy the effect of KI/BETi combinations will elucidate the mechanisms of BRD4. Testing the effect of combined BEZ235 with inhibitors of histone acetyltransferases<sup>18</sup>, histone deacetylases<sup>24,122,228</sup>, histone methyltransferases<sup>229,230</sup>, or histone demethylases<sup>18,231</sup> via sciATAC-seq and gene expression analyses will test whether repression of open chromatin architecture change is the main mechanism by which JQ1 inhibitors synergizes with BEZ235. Similarly, combinations of BEZ235 with inhibitors of the P-TEFb complex kinases CDK7 or CDK9 may elucidate the impact of the JQ1<sup>18</sup> RNA Polymerase kinase function on adaptive resistance. Most convincingly, however, would be to employ dominant negative versions of BRD4 where different domains are selectively mutated, including the bromodomain regions, histone acetyl-transferase domain, or kinase domain. Testing how these mutant BRD4

proteins affect adaptive response to kinase inhibitors will show which domain functions are critical to adaptive resistance in response to kinase inhibition.

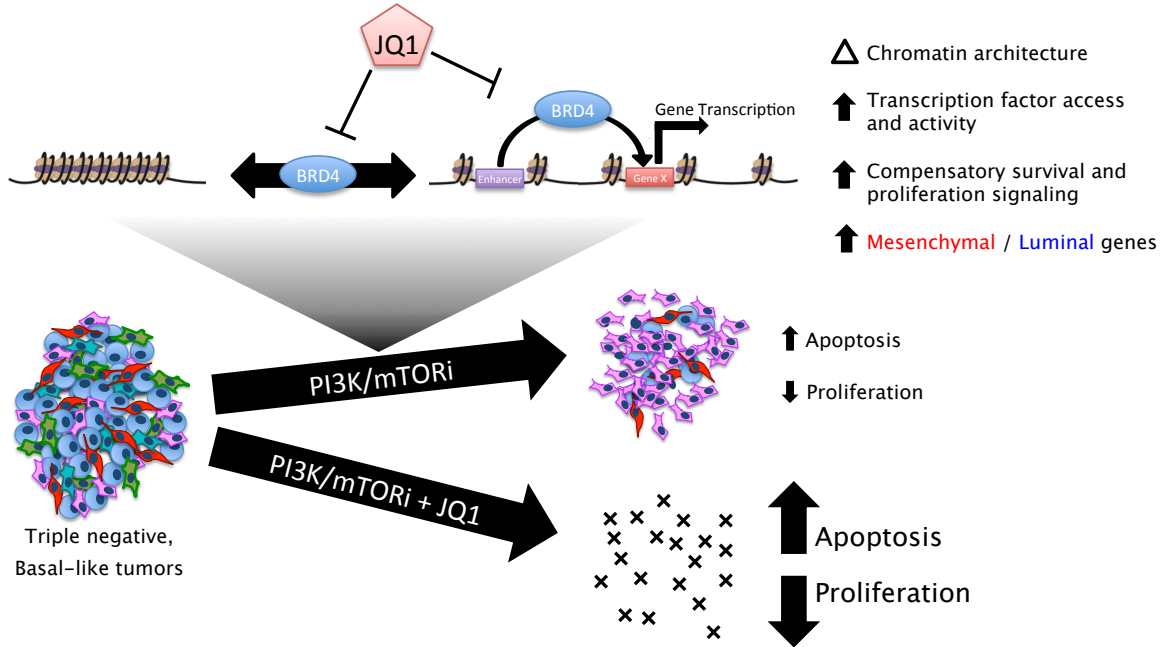


**Figure 6-1: Schematic of PI3K/mTOR inhibitor-induced changes in heterogeneous basal-like cell lines.**

A cartoon depicting the enrichment of drug-tolerant persister identity upon treatment of heterogeneous basal-like breast cancer cell lines with the PI3K/mTOR inhibitor BEZ235. This drug induces robust changes in chromatin architecture, transcription factor access and activity via geneset expression, as well as increased compensatory pathway gene expression, and differentiation gene expression including increases in luminal and mesenchymal markers. JQ1 antagonizes these chromatin changes and *de novo* enhancer formation, resulting in increased apoptosis, reduced proliferation, and repressed phenotype transitions when dosed in combination with BEZ235.

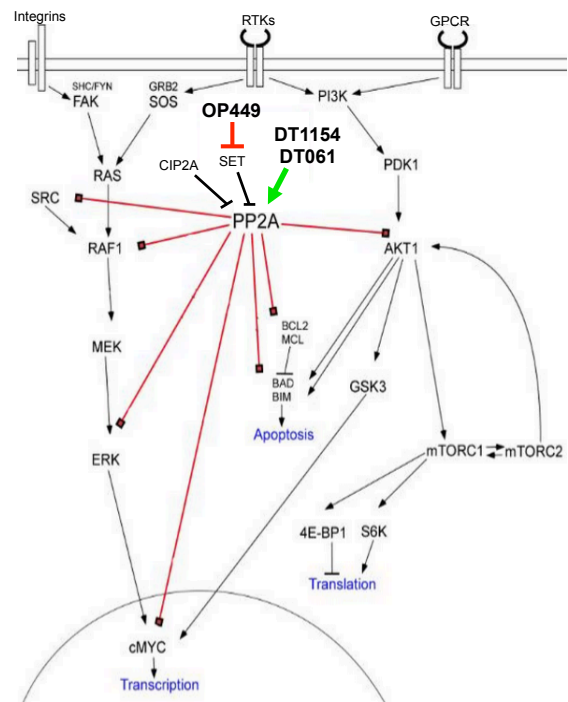
### 6.3.2 Advancing Small molecule activators of PP2A

Novel therapeutic mechanisms that can simultaneously inhibit numerous oncogenic signaling pathways are promising for the treatment of heterogeneous and plastic breast tumors. Such multi-pathway inhibitory agents would leave few options for compensatory pathway signaling to bypass the therapeutic effect. However, the lack of safety with multi-kinase small molecule inhibitors is usually a point of failure for their development, as observed with kinase inhibitors that have large target spectrums like staurosporine derivatives<sup>232</sup>. While effective at killing cancer cells, these drugs simultaneously inhibit many pathways in normal cells and lead to toxicity, making them impractical for cancer therapy. Activators of PP2A offer a solution to this issue by inducing multi-pathway downregulation in cancer cells, but are well tolerated in normal cells. Most tumors have evolved to possess mechanisms of PP2A repression, supporting hyperactivity of cell survival and proliferation pathways in the cancer. We show here that reactivation of PP2A in heterogeneous and plastic breast cancer cells promotes robust tumor cell cytotoxicity, and importantly, equally affects the different phenotypic subpopulations of cells present in culture. Further, these drugs were very effective at inhibiting tumor growth *in vivo* in genetically engineered mouse models, and were well tolerated in the animals, with no observed side effects of therapy. This speaks to the specificity of the inhibitory function of these agents only occurring in cells where PP2A has been endogenously repressed. In normal cells where PP2A is already active and maintaining a regulated phospho-signaling landscape, enhancement of activity with these agents does not

appear to have detrimental effects on cell viability. Due to this broad cell state potency, antitumor efficacy, and lack of toxicity in normal cells, PP2A activators represent a promising tool for the treatment of heterogeneous and plastic breast cancers will hopefully be clinically evaluated in this disease in the near future.

**Figure 6-2: PP2A targets and pharmacological activators.**

A schematic showing a reduced network of the proteins regulated by PP2A (red lines). Also included are the endogenous inhibitors of PP2A: SET and CIP2A. Therapeutic agents that activate PP2A are also shown, including OP449, which competes for SET binding, relieving endogenous PP2A repression, as well as the small-molecule activators of PP2A: DT061 and DT1154.



## 7 References

1. National Institute of Health, SEER Program. Cancer Stat Facts: Female Breast Cancer. (2017).
2. Jemal, A. *et al.* Annual Report to the Nation on the Status of Cancer, 1975–2014, Featuring Survival. *JNCI J. Natl. Cancer Inst.* **109**, (2017).
3. Dent, R. *et al.* Triple-Negative Breast Cancer: Clinical Features and Patterns of Recurrence. *Clin. Cancer Res.* **13**, 4429–4434 (2007).
4. Morris, G. J. *et al.* Differences in breast carcinoma characteristics in newly diagnosed African-American and Caucasian patients: a single-institution compilation compared with the National Cancer Institute’s Surveillance, Epidemiology, and End Results database. *Cancer* **110**, 876–884 (2007).
5. Lehmann, B. D. *et al.* Identification of human triple-negative breast cancer subtypes and preclinical models for selection of targeted therapies. *J. Clin. Invest.* **121**, 2750–2767 (2011).
6. Shah, S. P. *et al.* The clonal and mutational evolution spectrum of primary triple negative breast cancers. *Nature* **486**, (2012).
7. Liedtke, C. *et al.* Response to Neoadjuvant Therapy and Long-Term Survival in Patients With Triple-Negative Breast Cancer. *J. Clin. Oncol.* **26**, 1275–1281 (2008).
8. Carey, L. A. Directed Therapy of Subtypes of Triple-Negative Breast Cancer. *The Oncologist* **16**, 71–78 (2011).

9. Balko, J. M. *et al.* Profiling of residual breast cancers after neoadjuvant chemotherapy identifies DUSP4 deficiency as a mechanism of drug resistance. *Nat. Med.* **18**, 1052–1059 (2012).
10. Pratilas, C. A. *et al.* V600EBRAF is associated with disabled feedback inhibition of RAF–MEK signaling and elevated transcriptional output of the pathway. *Proc. Natl. Acad. Sci.* **106**, 4519–4524 (2009).
11. Hoeflich, K. P. *et al.* In vivo antitumor activity of MEK and phosphatidylinositol 3-kinase inhibitors in basal-like breast cancer models. *Clin. Cancer Res. Off. J. Am. Assoc. Cancer Res.* **15**, 4649–4664 (2009).
12. Saini, K. S. *et al.* Targeting the PI3K/AKT/mTOR and Raf/MEK/ERK pathways in the treatment of breast cancer. *Cancer Treat. Rev.* **39**, 935–946 (2013).
13. Heiser, L. M. *et al.* Subtype and pathway specific responses to anticancer compounds in breast cancer. *Proc. Natl. Acad. Sci.* 201018854 (2011). doi:10.1073/pnas.1018854108
14. Rinehart, J. *et al.* Multicenter Phase II Study of the Oral MEK Inhibitor, CI-1040, in Patients With Advanced Non-Small-Cell Lung, Breast, Colon, and Pancreatic Cancer. *J. Clin. Oncol.* **22**, 4456–4462 (2004).
15. LoRusso, P. M. *et al.* Phase I Pharmacokinetic and Pharmacodynamic Study of the Oral MAPK/ERK Kinase Inhibitor PD-0325901 in Patients with Advanced Cancers. *Clin. Cancer Res.* **16**, 1924–1937 (2010).
16. Adjei, A. A. *et al.* Phase I Pharmacokinetic and Pharmacodynamic Study of the Oral, Small-Molecule Mitogen-Activated Protein Kinase Kinase 1/2 Inhibitor AZD6244

- (ARRY-142886) in Patients With Advanced Cancers. *J. Clin. Oncol. Off. J. Am. Soc. Clin. Oncol.* **26**, 2139–2146 (2008).
17. Ramaswamy, B. *et al.* Abstract LB-216: NCI 9455: Phase II study of trametinib followed by trametinib plus AKT inhibitor, GSK2141795 in patients with advanced triple negative breast cancer. *Cancer Res.* **76**, LB-216-LB-216 (2016).
  18. Zawistowski, J. S. *et al.* Enhancer Remodeling during Adaptive Bypass to MEK Inhibition Is Attenuated by Pharmacologic Targeting of the P-TEFb Complex. *Cancer Discov.* (2017). doi:10.1158/2159-8290.CD-16-0653
  19. Turke, A. B. *et al.* Preexistence and clonal selection of MET amplification in EGFR mutant NSCLC. *Cancer Cell* **17**, 77–88 (2010).
  20. Reim, F. *et al.* Immunoselection of Breast and Ovarian Cancer Cells with Trastuzumab and Natural Killer Cells: Selective Escape of CD44<sup>high</sup>/CD24<sup>low</sup>/HER2<sup>low</sup> Breast Cancer Stem Cells. *Cancer Res.* **69**, 8058–8066 (2009).
  21. Yates, L. R. *et al.* Subclonal diversification of primary breast cancer revealed by multiregion sequencing. *Nat. Med.* **21**, 751–759 (2015).
  22. Creighton, C. J. *et al.* Residual breast cancers after conventional therapy display mesenchymal as well as tumor-initiating features. *Proc. Natl. Acad. Sci. U. S. A.* **106**, 13820–13825 (2009).
  23. Gupta, P. B. *et al.* Identification of Selective Inhibitors of Cancer Stem Cells by High-Throughput Screening. *Cell* **138**, 645–659 (2009).

24. Sharma, S. V. *et al.* A chromatin-mediated reversible drug-tolerant state in cancer cell subpopulations. *Cell* **141**, 69–80 (2010).
25. Goldman, A. *et al.* Temporally sequenced anticancer drugs overcome adaptive resistance by targeting a vulnerable chemotherapy-induced phenotypic transition. *Nat. Commun.* **6**, 6139 (2015).
26. Lakahni, S. R., Ellis, I. O., Schnitt, S. J., Tan, P. H. & Van de Vijver, M. J. *WHO Classification of Tumours, Volume 4*. **4**, (2014).
27. Lagios, M. D., Margolin, F. R., Westdahl, P. R. & Rose, M. R. Mammographically detected duct carcinoma in situ. Frequency of local recurrence following tylectomy and prognostic effect of nuclear grade on local recurrence. *Cancer* **63**, 618–624 (1989).
28. Poller, D. N. *et al.* Ideas in pathology. Ductal carcinoma in situ of the breast: a proposal for a new simplified histological classification association between cellular proliferation and c-erbB-2 protein expression. *Mod. Pathol. Off. J. U. S. Can. Acad. Pathol. Inc* **7**, 257–262 (1994).
29. Harris, L. *et al.* American Society of Clinical Oncology 2007 update of recommendations for the use of tumor markers in breast cancer. *J. Clin. Oncol. Off. J. Am. Soc. Clin. Oncol.* **25**, 5287–5312 (2007).
30. Cortazar, P. *et al.* Pathological complete response and long-term clinical benefit in breast cancer: the CTNeoBC pooled analysis. *The Lancet* **384**, 164–172 (2014).

31. Cheang, M. C. U. *et al.* Basal-Like Breast Cancer Defined by Five Biomarkers Has Superior Prognostic Value than Triple-Negative Phenotype. *Clin. Cancer Res.* **14**, 1368–1376 (2008).
32. Kennecke, H. *et al.* Metastatic Behavior of Breast Cancer Subtypes. *J. Clin. Oncol.* **28**, 3271–3277 (2010).
33. Smid, M. *et al.* Subtypes of breast cancer show preferential site of relapse. *Cancer Res.* **68**, 3108–3114 (2008).
34. Anderson, W. F., Rosenberg, P. S., Prat, A., Perou, C. M. & Sherman, M. E. How Many Etiological Subtypes of Breast Cancer: Two, Three, Four, Or More? *JNCI J. Natl. Cancer Inst.* **106**, (2014).
35. Cheang, M. C. U. *et al.* Ki67 index, HER2 status, and prognosis of patients with luminal B breast cancer. *J. Natl. Cancer Inst.* **101**, 736–750 (2009).
36. Kobayashi, T. *et al.* A simple immunohistochemical panel comprising 2 conventional markers, Ki67 and p53, is a powerful tool for predicting patient outcome in luminal-type breast cancer. *BMC Clin. Pathol.* **13**, 5 (2013).
37. Sørlie, T. *et al.* Repeated observation of breast tumor subtypes in independent gene expression data sets. *Proc. Natl. Acad. Sci.* **100**, 8418–8423 (2003).
38. Prat, A. *et al.* Phenotypic and molecular characterization of the claudin-low intrinsic subtype of breast cancer. *Breast Cancer Res.* **12**, R68 (2010).
39. Yersal, O. & Barutca, S. Biological subtypes of breast cancer: Prognostic and therapeutic implications. *World J. Clin. Oncol.* **5**, 412–424 (2014).

40. Goldhirsch, A. *et al.* Personalizing the treatment of women with early breast cancer: highlights of the St Gallen International Expert Consensus on the Primary Therapy of Early Breast Cancer 2013. *Ann. Oncol. Off. J. Eur. Soc. Med. Oncol.* **24**, 2206–2223 (2013).
41. Cancer Genome Atlas Network. Comprehensive molecular portraits of human breast tumours. *Nature* **490**, 61–70 (2012).
42. Santen, R. J., Brodie, H., Simpson, E. R., Siiteri, P. K. & Brodie, A. History of aromatase: saga of an important biological mediator and therapeutic target. *Endocr. Rev.* **30**, 343–375 (2009).
43. Howell, S. J., Johnston, S. R. D. & Howell, A. The use of selective estrogen receptor modulators and selective estrogen receptor down-regulators in breast cancer. *Best Pract. Res. Clin. Endocrinol. Metab.* **18**, 47–66 (2004).
44. Dombernowsky, P. *et al.* Letrozole, a new oral aromatase inhibitor for advanced breast cancer: double-blind randomized trial showing a dose effect and improved efficacy and tolerability compared with megestrol acetate. *J. Clin. Oncol. Off. J. Am. Soc. Clin. Oncol.* **16**, 453–461 (1998).
45. Perez, E. A. *et al.* Trastuzumab Plus Adjuvant Chemotherapy for Human Epidermal Growth Factor Receptor 2–Positive Breast Cancer: Planned Joint Analysis of Overall Survival From NSABP B-31 and NCCTG N9831. *J. Clin. Oncol.* **32**, 3744–3752 (2014).
46. Finn, R. S. *et al.* Palbociclib and Letrozole in Advanced Breast Cancer. *N. Engl. J. Med.* **375**, 1925–1936 (2016).

47. Royce, M. E. & Osman, D. Everolimus in the Treatment of Metastatic Breast Cancer. *Breast Cancer Basic Clin. Res.* **9**, 73–79 (2015).
48. Adamo, B. *et al.* Phosphatidylinositol 3-kinase pathway activation in breast cancer brain metastases. *Breast Cancer Res. BCR* **13**, R125 (2011).
49. Carey, L. A. *et al.* The triple negative paradox: primary tumor chemosensitivity of breast cancer subtypes. *Clin. Cancer Res. Off. J. Am. Assoc. Cancer Res.* **13**, 2329–2334 (2007).
50. Gonzalez-Angulo, A. M. *et al.* PI3K Pathway Mutations and PTEN Levels in Primary and Metastatic Breast Cancer. *Mol. Cancer Ther.* **10**, 1093–1101 (2011).
51. Lim, E. *et al.* Aberrant luminal progenitors as the candidate target population for basal tumor development in BRCA1 mutation carriers. *Nat. Med.* **15**, 907–913 (2009).
52. Park, H. S. *et al.* High EGFR gene copy number predicts poor outcome in triple-negative breast cancer. *Mod. Pathol. Off. J. U. S. Can. Acad. Pathol. Inc* **27**, 1212–1222 (2014).
53. Herschkowitz, J. I. *et al.* Comparative oncogenomics identifies breast tumors enriched in functional tumor-initiating cells. *Proc. Natl. Acad. Sci.* **109**, 2778–2783 (2012).
54. Giltane, J. M. & Balko, J. M. Rationale for Targeting the Ras/MAPK Pathway in Triple-Negative Breast Cancer. *Discov. Med.* **17**, 275–283 (2014).
55. Crown, J., O’Shaughnessy, J. & Gullo, G. Emerging targeted therapies in triple-negative breast cancer. *Ann. Oncol.* **23**, vi56-vi65 (2012).

56. Sarker, D. *et al.* First-in-human phase I study of pictilisib (GDC-0941), a potent pan-class I phosphatidylinositol-3-kinase (PI3K) inhibitor, in patients with advanced solid tumors. *Clin. Cancer Res. Off. J. Am. Assoc. Cancer Res.* **21**, 77–86 (2015).
57. Ganesan, P. *et al.* Triple Negative Breast Cancer Patients Treated at MD Anderson Cancer Center in Phase I Trials: Improved Outcomes with Combination Chemotherapy and Targeted Agents. *Mol. Cancer Ther.* **13**, 3175–3184 (2014).
58. Lorusso, P. *et al.* A first-in-human phase Ib study to evaluate the MEK inhibitor GDC-0973, combined with the pan-PI3K Inhibitor GDC-0941, in patients with advanced solid tumors. *J Clin Oncol 30Suppl Abstr.* 2566 (2012).
59. Ramanathan, R. *et al.* A Phase 1b trial of PI3K inhibitor copanlisib (BAY 80-6946) combined with the allosteric-MEK Inhibitor refametinib (BAY 86-9766) in patients with advanced cancer. *J Clin Oncol 325sSuppl Abstr.* 2588 (2014).
60. Nik-Zainal, S. *et al.* The life history of 21 breast cancers. *Cell* **149**, 994–1007 (2012).
61. Brocks, D. *et al.* Intratumor DNA methylation heterogeneity reflects clonal evolution in aggressive prostate cancer. *Cell Rep.* **8**, 798–806 (2014).
62. Giesen, C. *et al.* Highly multiplexed imaging of tumor tissues with subcellular resolution by mass cytometry. *Nat. Methods* **11**, 417–422 (2014).
63. Almendro, V. *et al.* Genetic and Phenotypic Diversity in Breast Tumor Metastases. *Cancer Res.* **74**, 1338–1348 (2014).
64. Patel, A. P. *et al.* Single-cell RNA-seq highlights intratumoral heterogeneity in primary glioblastoma. *Science* **344**, 1396–1401 (2014).

65. Dalerba, P. *et al.* Single-cell dissection of transcriptional heterogeneity in human colon tumors. *Nat. Biotechnol.* **29**, 1120–1127 (2011).
66. Corces, M. R. *et al.* Lineage-specific and single-cell chromatin accessibility charts human hematopoiesis and leukemia evolution. *Nat. Genet.* **48**, 1193–1203 (2016).
67. Risom, T., Langer, E., Rantala, J. & Chapman, M. Managing drug-induced differentiation-state plasticity in basal-like breast cancer to improve therapeutic control. *Nat. Commun.* (2017).
68. Pott, S. & Lieb, J. D. Single-cell ATAC-seq: strength in numbers. *Genome Biol.* **16**, 172 (2015).
69. Mathis, R. A., Sokol, E. S. & Gupta, P. B. Cancer cells exhibit clonal diversity in phenotypic plasticity. *Open Biol.* **7**, 160283 (2017).
70. Liao, B. B. *et al.* Adaptive Chromatin Remodeling Drives Glioblastoma Stem Cell Plasticity and Drug Tolerance. *Cell Stem Cell* **20**, 233–246.e7 (2017).
71. Huang, S. Genetic and non-genetic instability in tumor progression: link between the fitness landscape and the epigenetic landscape of cancer cells. *Cancer Metastasis Rev.* **32**, 423–448 (2013).
72. Granit, R. Z. *et al.* EZH2 promotes a bi-lineage identity in basal-like breast cancer cells. *Oncogene* **32**, 3886–3895 (2013).
73. Liu, S. *et al.* Breast cancer stem cells transition between epithelial and mesenchymal states reflective of their normal counterparts. *Stem Cell Rep.* **2**, 78–91 (2014).

74. Wright, M. H. *et al.* Brca1 breast tumors contain distinct CD44+/CD24- and CD133+ cells with cancer stem cell characteristics. *Breast Cancer Res. BCR* **10**, R10 (2008).
75. Bao, L., Cardiff, R. D., Steinbach, P., Messer, K. S. & Ellies, L. G. Multipotent luminal mammary cancer stem cells model tumor heterogeneity. *Breast Cancer Res. BCR* **17**, 137 (2015).
76. Charafe-Jauffret, E. *et al.* Breast Cancer Cell Lines Contain Functional Cancer Stem Cells with Metastatic Capacity and a Distinct Molecular Signature. *Cancer Res.* **69**, 1302–1313 (2009).
77. Al-Hajj, M., Wicha, M. S., Benito-Hernandez, A., Morrison, S. J. & Clarke, M. F. Prospective identification of tumorigenic breast cancer cells. *Proc. Natl. Acad. Sci. U. S. A.* **100**, 3983–3988 (2003).
78. Gómez-Miragaya, J. *et al.* Resistance to Taxanes in Triple-Negative Breast Cancer Associates with the Dynamics of a CD49f+ Tumor-Initiating Population. *Stem Cell Rep.* **8**, 1392–1407 (2017).
79. Condiotti, R., Guo, W. & Ben-Porath, I. Evolving views of breast cancer stem cells and their differentiation States. *Crit. Rev. Oncog.* **19**, 337–348 (2014).
80. Li, Q.-Q. *et al.* Twist1-mediated adriamycin-induced epithelial-mesenchymal transition relates to multidrug resistance and invasive potential in breast cancer cells. *Clin. Cancer Res. Off. J. Am. Assoc. Cancer Res.* **15**, 2657–2665 (2009).

81. Laakso, M. *et al.* Basoluminal carcinoma: a new biologically and prognostically distinct entity between basal and luminal breast cancer. *Clin. Cancer Res. Off. J. Am. Assoc. Cancer Res.* **12**, 4185–4191 (2006).
82. Volkmer, J.-P. *et al.* Three differentiation states risk-stratify bladder cancer into distinct subtypes. *Proc. Natl. Acad. Sci. U. S. A.* **109**, 2078–2083 (2012).
83. Krohn, A. *et al.* Tumor Cell Heterogeneity in Small Cell Lung Cancer (SCLC): Phenotypical and Functional Differences Associated with Epithelial-Mesenchymal Transition (EMT) and DNA Methylation Changes. *PLOS ONE* **9**, e100249 (2014).
84. Terry, S. & Beltran, H. The Many Faces of Neuroendocrine Differentiation in Prostate Cancer Progression. *Front. Oncol.* **4**, (2014).
85. Kamisawa, T. *et al.* Neuroendocrine differentiation in pancreatic duct carcinoma special emphasis on duct-endocrine cell carcinoma of the pancreas. *Pathol. Res. Pract.* **192**, 901–908 (1996).
86. Al-Hajj, M., Wicha, M. S., Benito-Hernandez, A., Morrison, S. J. & Clarke, M. F. Prospective identification of tumorigenic breast cancer cells. *Proc. Natl. Acad. Sci. U. S. A.* **100**, 3983–3988 (2003).
87. Chung, G. G., Zerkowski, M. P., Ghosh, S., Camp, R. L. & Rimm, D. L. Quantitative analysis of estrogen receptor heterogeneity in breast cancer. *Lab. Invest.* **87**, 662–669 (2007).
88. Potts, S. J. *et al.* Evaluating tumor heterogeneity in immunohistochemistry-stained breast cancer tissue. *Lab. Investig. J. Tech. Methods Pathol.* **92**, 1342–1357 (2012).

89. Schmitt, M. W., Loeb, L. A. & Salk, J. J. The influence of subclonal resistance mutations on targeted cancer therapy. *Nat. Rev. Clin. Oncol.* (2015).  
doi:10.1038/nrclinonc.2015.175
90. Jeselsohn, R., Buchwalter, G., De Angelis, C., Brown, M. & Schiff, R. ESR1 mutations as a mechanism for acquired endocrine resistance in breast cancer. *Nat. Rev. Clin. Oncol.* **12**, 573–583 (2015).
91. Patrawala, L. *et al.* Side population is enriched in tumorigenic, stem-like cancer cells, whereas ABCG2+ and ABCG2- cancer cells are similarly tumorigenic. *Cancer Res.* **65**, 6207–6219 (2005).
92. Tao, W. *et al.* Egr-1 enhances drug resistance of breast cancer by modulating MDR1 expression in a GGPPS-independent manner. *Biomed. Pharmacother. Biomedicine Pharmacother.* **67**, 197–202 (2013).
93. Gupta, P. B. *et al.* Stochastic State Transitions Give Rise to Phenotypic Equilibrium in Populations of Cancer Cells. *Cell* **146**, 633–644 (2011).
94. Wabik, A. & Jones, P. H. Switching roles: the functional plasticity of adult tissue stem cells. *EMBO J.* **34**, 1164–1179 (2015).
95. Spike, B. T. *et al.* A Mammary Stem Cell Population Identified and Characterized in Late Embryogenesis Reveals Similarities to Human Breast Cancer. *Cell Stem Cell* **10**, 183–197 (2012).

96. Clayton, H., Titley, I. & Vivanco, M. dM. Growth and differentiation of progenitor/stem cells derived from the human mammary gland. *Exp. Cell Res.* **297**, 444–460 (2004).
97. Visvader, J. E. & Stingl, J. Mammary stem cells and the differentiation hierarchy: current status and perspectives. *Genes Dev.* **28**, 1143–1158 (2014).
98. Pfefferle, A. D., Spike, B. T., Wahl, G. M. & Perou, C. M. Luminal progenitor and fetal mammary stem cell expression features predict breast tumor response to neoadjuvant chemotherapy. *Breast Cancer Res. Treat.* **149**, 425–437 (2015).
99. Hardy, K. M., Booth, B. W., Hendrix, M. J. C., Salomon, D. S. & Strizzi, L. ErbB/EGF Signaling and EMT in Mammary Development and Breast Cancer. *J. Mammary Gland Biol. Neoplasia* **15**, 191–199 (2010).
100. Meissner, A. *et al.* Genome-scale DNA methylation maps of pluripotent and differentiated cells. *Nature* **454**, 766–770 (2008).
101. Hughes, A. E. O., Enright, J. M., Myers, C. A., Shen, S. Q. & Corbo, J. C. Cell Type-Specific Epigenomic Analysis Reveals a Uniquely Closed Chromatin Architecture in Mouse Rod Photoreceptors. *Sci. Rep.* **7**, srep43184 (2017).
102. Lien, W.-H. *et al.* Genome-wide maps of histone modifications unwind in vivo chromatin states of the hair follicle lineage. *Cell Stem Cell* **9**, 219–232 (2011).
103. Gascard, P. *et al.* Epigenetic and transcriptional determinants of the human breast. *Nat. Commun.* **6**, 6351 (2015).

104. Mikkelsen, T. S. *et al.* Comparative epigenomic analysis of murine and human adipogenesis. *Cell* **143**, 156–169 (2010).
105. Liu, W. *et al.* Brd4 and JMJD6-associated Anti-pause Enhancers in Regulation of Transcriptional Pause Release. *Cell* **155**, 1581–1595 (2013).
106. Itzen, F., Greifenberg, A. K., Böskén, C. A. & Geyer, M. Brd4 activates P-TEFb for RNA polymerase II CTD phosphorylation. *Nucleic Acids Res.* **42**, 7577–7590 (2014).
107. Cui, K. *et al.* Chromatin signatures in multipotent human hematopoietic stem cells indicate the fate of bivalent genes during differentiation. *Cell Stem Cell* **4**, 80–93 (2009).
108. Chaffer, C. L. *et al.* Poised chromatin at the ZEB1 promoter enables breast cancer cell plasticity and enhances tumorigenicity. *Cell* **154**, 61–74 (2013).
109. De Gobbi, M. *et al.* Generation of bivalent chromatin domains during cell fate decisions. *Epigenetics Chromatin* **4**, 9 (2011).
110. Asselin-Labat, M.-L. *et al.* Gata-3 is an essential regulator of mammary-gland morphogenesis and luminal-cell differentiation. *Nat. Cell Biol.* **9**, 201–209 (2007).
111. Granit, R. Z., Slyper, M. & Ben-Porath, I. Axes of differentiation in breast cancer: untangling stemness, lineage identity, and the epithelial to mesenchymal transition. *Wiley Interdiscip. Rev. Syst. Biol. Med.* **6**, 93–106 (2014).
112. Peinado, H., Ballestar, E., Esteller, M. & Cano, A. Snail mediates E-cadherin repression by the recruitment of the Sin3A/histone deacetylase 1 (HDAC1)/HDAC2 complex. *Mol. Cell. Biol.* **24**, 306–319 (2004).

113. Ramadoss, S., Chen, X. & Wang, C.-Y. Histone demethylase KDM6B promotes epithelial-mesenchymal transition. *J. Biol. Chem.* **287**, 44508–44517 (2012).
114. Whyte, W. A. *et al.* Master Transcription Factors and Mediator Establish Super-Enhancers at Key Cell Identity Genes. *Cell* **153**, 307–319 (2013).
115. Dravis, C. *et al.* Sox10 Regulates Stem/Progenitor and Mesenchymal Cell States in Mammary Epithelial Cells. *Cell Rep.* **12**, 2035–2048 (2015).
116. Almendro, V. *et al.* Inference of tumor evolution during chemotherapy by computational modeling and in situ analysis of cellular diversity for genetic and phenotypic features. *Cell Rep.* **6**, 514–527 (2014).
117. Keller, P. J. *et al.* Mapping the cellular and molecular heterogeneity of normal and malignant breast tissues and cultured cell lines. *Breast Cancer Res. BCR* **12**, R87 (2010).
118. Prat, A. *et al.* Characterization of cell lines derived from breast cancers and normal mammary tissues for the study of the intrinsic molecular subtypes. *Breast Cancer Res. Treat.* **142**, 237–255 (2013).
119. Andriani, F. *et al.* Conversion to stem-cell state in response to microenvironmental cues is regulated by balance between epithelial and mesenchymal features in lung cancer cells. *Mol. Oncol.* **10**, 253–271 (2016).
120. Widmer, D. S. *et al.* Hypoxia Contributes to Melanoma Heterogeneity by Triggering HIF1 $\alpha$ -Dependent Phenotype Switching. *J. Invest. Dermatol.* **133**, 2436–2443 (2013).

121. Lesniak, D. *et al.* Spontaneous Epithelial-Mesenchymal Transition and Resistance to HER-2-Targeted Therapies in HER-2-Positive Luminal Breast Cancer. *PLoS ONE* **8**, (2013).
122. Banelli, B. *et al.* The histone demethylase KDM5A is a key factor for the resistance to temozolomide in glioblastoma. *Cell Cycle Georget. Tex* **14**, 3418–3429 (2015).
123. Stuhlmiller, T. J. *et al.* Inhibition of Lapatinib-Induced Kinome Reprogramming in ERBB2-Positive Breast Cancer by Targeting BET Family Bromodomains. *Cell Rep.* **11**, 390–404 (2015).
124. Stratikopoulos, E. E. *et al.* Kinase and BET Inhibitors Together Clamp Inhibition of PI3K Signaling and Overcome Resistance to Therapy. *Cancer Cell* **27**, 837–851 (2015).
125. Devaiah, B. N. *et al.* BRD4 is a histone acetyltransferase that evicts nucleosomes from chromatin. *Nat. Struct. Mol. Biol.* **advance online publication**, (2016).
126. Seshacharyulu, P., Pandey, P., Datta, K. & Batra, S. K. Phosphatase: PP2A structural importance, regulation and its aberrant expression in cancer. *Cancer Lett.* **335**, 9–18 (2013).
127. Kuo, Y.-C. *et al.* Regulation of phosphorylation of Thr-308 of Akt, cell proliferation, and survival by the B55alpha regulatory subunit targeting of the protein phosphatase 2A holoenzyme to Akt. *J. Biol. Chem.* **283**, 1882–1892 (2008).
128. Khanna, A., Pimanda, J. E. & Westermarck, J. Cancerous Inhibitor of Protein Phosphatase 2A, an Emerging Human Oncoprotein and a Potential Cancer Therapy Target. *Cancer Res.* **73**, 6548–6553 (2013).

129. Cristóbal, I. *et al.* Overexpression of SET is a recurrent event associated with poor outcome and contributes to protein phosphatase 2A inhibition in acute myeloid leukemia. *Haematologica* **97**, 543–550 (2012).
130. Sangodkar, J. *et al.* Activation of tumor suppressor protein PP2A inhibits KRAS-driven tumor growth. *J. Clin. Invest.* **127**, 2081–2090 (2017).
131. Farrell, A. S. *et al.* Targeting Inhibitors of the Tumor Suppressor PP2A for the Treatment of Pancreatic Cancer. *Mol. Cancer Res.* **12**, 924–939 (2014).
132. Janghorban, M. *et al.* Targeting c-MYC by antagonizing PP2A inhibitors in breast cancer. *Proc. Natl. Acad. Sci. U. S. A.* **111**, 9157–9162 (2014).
133. Gutierrez, A. *et al.* Phenothiazines induce PP2A-mediated apoptosis in T cell acute lymphoblastic leukemia. *J. Clin. Invest.* **124**, 644–655 (2014).
134. Hennessy, B. T. *et al.* Characterization of a naturally occurring breast cancer subset enriched in epithelial-to-mesenchymal transition and stem cell characteristics. *Cancer Res.* **69**, 4116–4124 (2009).
135. Bao, S. *et al.* Glioma stem cells promote radioresistance by preferential activation of the DNA damage response. *Nature* **444**, 756–760 (2006).
136. Baker, E. K., Johnstone, R. W., Zalcberg, J. R. & El-Osta, A. Epigenetic changes to the MDR1 locus in response to chemotherapeutic drugs. *Oncogene* **24**, 8061–8075 (2005).

137. Chakrabarti, L., Abou-Antoun, T., Vukmanovic, S. & Sandler, A. D. Reversible adaptive plasticity: a mechanism for neuroblastoma cell heterogeneity and chemoresistance. *Pediatr. Oncol.* **2**, 82 (2012).
138. Sun, C. *et al.* Reversible and adaptive resistance to BRAF(V600E) inhibition in melanoma. *Nature* **508**, 118–122 (2014).
139. Shannon, C. E. & Weaver, W. *The mathematical theory of communication*. (University of Illinois Press, 1963).
140. Taylor-Papadimitriou, J. *et al.* Keratin expression in human mammary epithelial cells cultured from normal and malignant tissue: relation to in vivo phenotypes and influence of medium. *J. Cell Sci.* **94**, 403–413 (1989).
141. Pandey, P. R., Saidou, J. & Watabe, K. Role of myoepithelial cells in breast tumor progression. *Front. Biosci. J. Virtual Libr.* **15**, 226–236 (2010).
142. Ivaska, J. Vimentin: Central hub in EMT induction? *Small GTPases* **2**, 51–53 (2011).
143. Zhang, X. *et al.* A Renewable Tissue Resource of Phenotypically Stable, Biologically and Ethnically Diverse, Patient-derived Human Breast Cancer Xenograft (PDX) Models. *Cancer Res.* **73**, 4885–4897 (2013).
144. Daemen, A. *et al.* Modeling precision treatment of breast cancer. *Genome Biol.* **14**, R110 (2013).
145. Jones, C. *et al.* Expression profiling of purified normal human luminal and myoepithelial breast cells: identification of novel prognostic markers for breast cancer. *Cancer Res.* **64**, 3037–3045 (2004).

146. Shehata, M. *et al.* Phenotypic and functional characterisation of the luminal cell hierarchy of the mammary gland. *Breast Cancer Res.* **14**, R134 (2012).
147. Zeisberg, M. & Neilson, E. G. Biomarkers for epithelial-mesenchymal transitions. *J. Clin. Invest.* **119**, 1429–1437 (2009).
148. Micalizzi, D. S., Farabaugh, S. M. & Ford, H. L. Epithelial-Mesenchymal Transition in Cancer: Parallels Between Normal Development and Tumor Progression. *J. Mammary Gland Biol. Neoplasia* **15**, 117–134 (2010).
149. Watson, S. & Gray, J. Basal and Luminal HEr2 Lines Different Microenvironmental Response. *Cell Syst.*
150. Santagata, S. *et al.* Taxonomy of breast cancer based on normal cell phenotype predicts outcome. *J. Clin. Invest.* **124**, 859–870 (2014).
151. Li, K., Bihan, M., Yooseph, S. & Methé, B. A. Analyses of the Microbial Diversity across the Human Microbiome. *PLOS ONE* **7**, e32118 (2012).
152. Tramer, E. J. Bird Species Diversity: Components of Shannon's Formula. *Ecology* **50**, 927–929 (1969).
153. Pellacani, D. *et al.* Analysis of Normal Human Mammary Epigenomes Reveals Cell-Specific Active Enhancer States and Associated Transcription Factor Networks. *Cell Rep.* **17**, 2060–2074 (2016).
154. Lara-Astiaso, D. *et al.* Chromatin state dynamics during blood formation. *Science* **345**, 943–949 (2014).

155. Stergachis, A. B. *et al.* Developmental fate and cellular maturity encoded in human regulatory DNA landscapes. *Cell* **154**, 888–903 (2013).
156. Klevebring, D. *et al.* Sequencing of breast cancer stem cell populations indicates a dynamic conversion between differentiation states in vivo. *Breast Cancer Res. BCR* **16**, R72 (2014).
157. Chaffer, C. L. *et al.* Normal and neoplastic nonstem cells can spontaneously convert to a stem-like state. *Proc. Natl. Acad. Sci.* **108**, 7950–7955 (2011).
158. Knoechel, B. *et al.* An epigenetic mechanism of resistance to targeted therapy in T cell acute lymphoblastic leukemia. *Nat. Genet.* **46**, 364–370 (2014).
159. Bhang, H. C. *et al.* Studying clonal dynamics in response to cancer therapy using high-complexity barcoding. *Nat. Med.* **21**, 440–448 (2015).
160. Subramanian, A. *et al.* Gene set enrichment analysis: a knowledge-based approach for interpreting genome-wide expression profiles. *Proc. Natl. Acad. Sci. U. S. A.* **102**, 15545–15550 (2005).
161. Neve, R. M. *et al.* A collection of breast cancer cell lines for the study of functionally distinct cancer subtypes. *Cancer Cell* **10**, 515–527 (2006).
162. Charafe-Jauffret, E. *et al.* Gene expression profiling of breast cell lines identifies potential new basal markers. *Oncogene* **25**, 2273–2284 (2005).
163. Ben-Porath, I. *et al.* An embryonic stem cell-like gene expression signature in poorly differentiated aggressive human tumors. *Nat. Genet.* **40**, 499–507 (2008).

164. Mariano J Alvarez *et al.* Functional characterization of somatic mutations in cancer using network-based inference of protein activity. *Nat. Genet.* (2016).
165. Huang, D. W., Sherman, B. T. & Lempicki, R. A. Systematic and integrative analysis of large gene lists using DAVID bioinformatics resources. *Nat. Protoc.* **4**, 44–57 (2009).
166. Chou, T.-C. Drug Combination Studies and Their Synergy Quantification Using the Chou-Talalay Method. *Cancer Res.* **70**, 440–446 (2010).
167. Crawford, N. P. S. *et al.* Bromodomain 4 activation predicts breast cancer survival. *Proc. Natl. Acad. Sci.* **105**, 6380–6385 (2008).
168. Shu, S. *et al.* Response and resistance to BET bromodomain inhibitors in triple-negative breast cancer. *Nature* **529**, 413–417 (2016).
169. Scibetta, A. G. *et al.* Functional analysis of the transcription repressor PLU-1/JARID1B. *Mol. Cell. Biol.* **27**, 7220–7235 (2007).
170. Cusanovich, D. A. *et al.* Multiplex single cell profiling of chromatin accessibility by combinatorial cellular indexing. *Science* **348**, 910–914 (2015).
171. Schep, A. N., Wu, B., Buenrostro, J. D. & Greenleaf, W. J. chromVAR: Inferring transcription factor variation from single-cell epigenomic data. *bioRxiv* 110346 (2017).  
doi:10.1101/110346
172. Bakiri, L. *et al.* Fra-1/AP-1 induces EMT in mammary epithelial cells by modulating Zeb1/2 and TGF $\beta$  expression. *Cell Death Differ.* **22**, 336–350 (2015).
173. Zhan, Y. *et al.* MicroRNA-182 drives colonization and macroscopic metastasis via targeting its suppressor SNAIL in breast cancer. *Oncotarget* **8**, 4629–4641 (2017).

174. Chu, I. M. *et al.* Expression of GATA3 in MDA-MB-231 triple-negative breast cancer cells induces a growth inhibitory response to TGF $\beta$ . *PLoS One* **8**, e61125 (2013).
175. Duncan, J. S. *et al.* Dynamic Reprogramming of the Kinome In Response to Targeted MEK Inhibition In Triple Negative Breast Cancer. *Cell* **149**, 307–321 (2012).
176. Turke, A. B. *et al.* MEK inhibition leads to PI3K/AKT activation by relieving a negative feedback on ERBB receptors. *Cancer Res.* **72**, 3228–3237 (2012).
177. Cooper, G. M. *The Development and Causes of Cancer.* (2000).
178. Gross, S., Rahal, R., Stransky, N., Lengauer, C. & Hoeflich, K. P. Targeting cancer with kinase inhibitors. *J. Clin. Invest.* **125**, 1780–1789 (2015).
179. Wu, P., Nielsen, T. E. & Clausen, M. H. Small-molecule kinase inhibitors: an analysis of FDA-approved drugs. *Drug Discov. Today* **21**, 5–10 (2016).
180. Lovly, C. M. & Shaw, A. T. Molecular Pathways: Resistance to Kinase Inhibitors and Implications for Therapeutic Strategies. *Clin. Cancer Res.* **20**, 2249–2256 (2014).
181. Dy, G. K. & Adjei, A. A. Understanding, recognizing, and managing toxicities of targeted anticancer therapies. *CA. Cancer J. Clin.* **63**, 249–279 (2013).
182. Eckstein, N. *et al.* Clinical pharmacology of tyrosine kinase inhibitors becoming generic drugs: the regulatory perspective. *J. Exp. Clin. Cancer Res.* **33**, 15 (2014).
183. Cheng, F., Jia, P., Wang, Q. & Zhao, Z. Quantitative network mapping of the human kinome interactome reveals new clues for rational kinase inhibitor discovery and individualized cancer therapy. *Oncotarget* **5**, 3697–3710 (2014).

184. Sacco, F., Perfetto, L., Castagnoli, L. & Cesareni, G. The human phosphatase interactome: An intricate family portrait. *Febs Lett.* **586**, 2732–2739 (2012).
185. Sangodkar, J. *et al.* All roads lead to PP2A: exploiting the therapeutic potential of this phosphatase. *FEBS J.* **283**, 1004–1024 (2016).
186. Ruvolo, P. P. *et al.* Low Expression Of PP2A Regulatory Subunit B55 $\alpha$  Is Associated With T308 Phosphorylation Of AKT And Shorter Complete Remission Duration In Acute Myeloid Leukemia Patients. *Leukemia* **25**, 1711–1717 (2011).
187. Roberts, K. G. *et al.* Essential requirement for PP2A inhibition by the oncogenic receptor c-KIT suggests PP2A reactivation as a strategy to treat c-KIT<sup>+</sup> cancers. *Cancer Res.* **70**, 5438–5447 (2010).
188. Christensen, D. J. *et al.* SET oncoprotein overexpression in B-cell chronic lymphocytic leukemia and non-Hodgkin lymphoma: a predictor of aggressive disease and a new treatment target. *Blood* **118**, 4150–4158 (2011).
189. Böckelman, C. *et al.* Prognostic role of CIP2A expression in serous ovarian cancer. *Br. J. Cancer* **105**, 989–995 (2011).
190. Agarwal, A. *et al.* Antagonism of SET Using OP449 Enhances the Efficacy of Tyrosine Kinase Inhibitors and Overcomes Drug Resistance in Myeloid Leukemia. *Clin. Cancer Res.* **20**, 2092–2103 (2014).
191. Cristóbal, I. *et al.* PP2A impaired activity is a common event in acute myeloid leukemia and its activation by forskolin has a potent anti-leukemic effect. *Leukemia* **25**, 606–614 (2011).

192. Lim, K. G. *et al.* FTY720 analogues as sphingosine kinase 1 inhibitors: enzyme inhibition kinetics, allosterism, proteasomal degradation, and actin rearrangement in MCF-7 breast cancer cells. *J. Biol. Chem.* **286**, 18633–18640 (2011).
193. Omar, H. A. *et al.* Antitumor Effects of OSU-2S, a Non-immunosuppressive Analogue of FTY720, in Hepatocellular Carcinoma. *Hepatol. Baltim. Md* **53**, 1943–1958 (2011).
194. Neviani, P. *et al.* FTY720, a new alternative for treating blast crisis chronic myelogenous leukemia and Philadelphia chromosome-positive acute lymphocytic leukemia. *J. Clin. Invest.* **117**, 2408–2421 (2007).
195. Shenolikar, S. A SMAP in the face for cancer. *J. Clin. Invest.* **127**, 2048–2050 (2017).
196. Carpenter, A. E. *et al.* CellProfiler: image analysis software for identifying and quantifying cell phenotypes. *Genome Biol.* **7**, R100 (2006).
197. Langmead, B. & Salzberg, S. L. Fast gapped-read alignment with Bowtie 2. *Nat. Methods* **9**, 357–359 (2012).
198. Tyner, J. W. *et al.* Kinase pathway dependence in primary human leukemias determined by rapid inhibitor screening. *Cancer Res.* **73**, 285–296 (2013).
199. Grant, M. & Boyd, S. CVX: Matlab software for disciplined convex programming, version 2.1. <http://cvxr.com/cvx> (2015).
200. Chapman, M. P. *et al.* A model of phenotypic state dynamics initiates a promising approach to control heterogeneous malignant cell populations. in *2016 IEEE 55th Conference on Decision and Control (CDC)* 2481–2487 (2016).  
  
doi:10.1109/CDC.2016.7798634

201. Anders, S. & Huber, W. Differential expression analysis for sequence count data. *Genome Biol.* **11**, R106 (2010).
202. Margolin, A. A. *et al.* ARACNE: an algorithm for the reconstruction of gene regulatory networks in a mammalian cellular context. *BMC Bioinformatics* **7 Suppl 1**, S7 (2006).
203. Amini, S. *et al.* Haplotype-resolved whole-genome sequencing by contiguity-preserving transposition and combinatorial indexing. *Nat. Genet.* **46**, 1343–1349 (2014).
204. Vitak, S. A. *et al.* Sequencing thousands of single-cell genomes with combinatorial indexing. *Nat. Methods* **14**, 302–308 (2017).
205. Zhang, Y. *et al.* Model-based Analysis of ChIP-Seq (MACS). *Genome Biol.* **9**, R137 (2008).
206. Maaten, L. van der & Hinton, G. Visualizing Data using t-SNE. *J. Mach. Learn. Res.* **9**, 2579–2605 (2008).
207. Gerlinger, M. *et al.* Genomic architecture and evolution of clear cell renal cell carcinomas defined by multiregion sequencing. *Nat. Genet.* **46**, 225–233 (2014).
208. Shu, Y. *et al.* Circulating Tumor DNA Mutation Profiling by Targeted Next Generation Sequencing Provides Guidance for Personalized Treatments in Multiple Cancer Types. *Sci. Rep.* **7**, 583 (2017).
209. Butler, T. M. *et al.* Exome Sequencing of Cell-Free DNA from Metastatic Cancer Patients Identifies Clinically Actionable Mutations Distinct from Primary Disease. *PLoS ONE* **10**, (2015).

210. Kwon, M. *et al.* Paracrine signaling between tumor subclones of mouse SCLC: a critical role of ETS transcription factor Pea3 in facilitating metastasis. *Genes Dev.* **29**, 1587–1592 (2015).
211. Marusyk, A. *et al.* Non-cell-autonomous driving of tumour growth supports sub-clonal heterogeneity. *Nature* **514**, 54–58 (2014).
212. Gatenby, R. A., Silva, A. S., Gillies, R. J. & Frieden, B. R. Adaptive therapy. *Cancer Res.* **69**, 4894–4903 (2009).
213. Kreso, A. *et al.* Variable clonal repopulation dynamics influence chemotherapy response in colorectal cancer. *Science* **339**, 543–548 (2013).
214. Wargo, A. R., Huijben, S., de Roode, J. C., Shepherd, J. & Read, A. F. Competitive release and facilitation of drug-resistant parasites after therapeutic chemotherapy in a rodent malaria model. *Proc. Natl. Acad. Sci. U. S. A.* **104**, 19914–19919 (2007).
215. Keshelava, N. *et al.* Loss of p53 function confers high-level multidrug resistance in neuroblastoma cell lines. *Cancer Res.* **61**, 6185–6193 (2001).
216. Chaudhary, P. M. & Roninson, I. B. Induction of multidrug resistance in human cells by transient exposure to different chemotherapeutic drugs. *J. Natl. Cancer Inst.* **85**, 632–639 (1993).
217. Kim, M. *et al.* The Multidrug Resistance Transporter ABCG2 (Breast Cancer Resistance Protein 1) Effluxes Hoechst 33342 and Is Overexpressed in Hematopoietic Stem Cells. *Clin. Cancer Res.* **8**, 22–28 (2002).

218. Bozic, I. *et al.* Evolutionary dynamics of cancer in response to targeted combination therapy. *eLife* **2**, e00747 (2013).
219. Silva, A. S. & Gatenby, R. A. A theoretical quantitative model for evolution of cancer chemotherapy resistance. *Biol. Direct* **5**, 25 (2010).
220. Thakur, M. D. *et al.* Modelling vemurafenib resistance in melanoma reveals a strategy to forestall drug resistance. *Nature* **494**, 251–255 (2013).
221. Jung, M. *et al.* Affinity Map of Bromodomain Protein 4 (BRD4) Interactions with the Histone H4 Tail and the Small Molecule Inhibitor JQ1. *J. Biol. Chem.* **289**, 9304–9319 (2014).
222. Filippakopoulos, P. *et al.* Selective inhibition of BET bromodomains. *Nature* **468**, 1067–1073 (2010).
223. Andrieu, G., Belkina, A. C. & Denis, G. V. Clinical trials for BET inhibitors run ahead of the science. *Drug Discov. Today Technol.* **19**, 45–50 (2016).
224. Abedin, S. M., Boddy, C. S. & Munshi, H. G. BET inhibitors in the treatment of hematologic malignancies: current insights and future prospects. *Oncotargets and Therapy* (2016). doi:10.2147/OTT.S100515
225. ENCODE: Encyclopedia of DNA Elements – ENCODE. Available at: <https://www.encodeproject.org/>. (Accessed: 16th August 2017)
226. Core, L. J., Waterfall, J. J. & Lis, J. T. Nascent RNA Sequencing Reveals Widespread Pausing and Divergent Initiation at Human Promoters. *Science* **322**, 1845–1848 (2008).

227. Kwak, H., Fuda, N. J., Core, L. J. & Lis, J. T. Precise Maps of RNA Polymerase Reveal How Promoters Direct Initiation and Pausing. *Science* **339**, 950–953 (2013).
228. Conte, P. *et al.* Phase I trial of panobinostat (LBH589) in combination with trastuzumab in pretreated HER2-positive metastatic breast cancer (mBC): Preliminary safety and tolerability results. *J. Clin. Oncol.* **27**, 1081–1081 (2009).
229. Kim, K. H. & Roberts, C. W. M. Targeting EZH2 in cancer. *Nat. Med.* **22**, 128–134 (2016).
230. Knutson, S. K. *et al.* Synergistic Anti-Tumor Activity of EZH2 Inhibitors and Glucocorticoid Receptor Agonists in Models of Germinal Center Non-Hodgkin Lymphomas. *PLoS ONE* **9**, (2014).
231. Vinogradova, M. *et al.* An inhibitor of KDM5 demethylases reduces survival of drug-tolerant cancer cells. *Nat. Chem. Biol.* **12**, 531–538 (2016).
232. Mukthavaram, R. *et al.* High-efficiency liposomal encapsulation of a tyrosine kinase inhibitor leads to improved in vivo toxicity and tumor response profile. *Int. J. Nanomedicine* **8**, 3991–4006 (2013).

## 8 Appendix - Extended description of computational modeling

The purpose of this supplement is to explain in greater detail how fold change was simulated using timecourse data and mathematical modeling (Fig. 3-3). Notation is presented, and a description of the dynamical system follows. Then, we summarize model identification details and show how to compute model-derived fold change.

All mathematical modeling and supplemental methods were designed and written by Margaret Chapman with additional instruction from Claire Tomlin.

### I. Notation

Symbols and definitions are below. All terms are agent-specific (e.g., DMSO, Trametinib).

*Gain* is the discrete-time analog of *rate*. Terms labeled  $\rho$  are parameters of the system dynamics<sup>200</sup>.

Symbol	Definition
$\#K14_{\text{obs}}^{\text{lo}}$	observed number of $K14^{\text{low}}$ cells via image cytometry
$\#K14_{\text{obs}}^{\text{hi}}$	observed number of $K14^{\text{high}}$ cells via image cytometry
$f_{\text{obs}}^{\text{dead}}$	observed fraction of dead cells via YO-PRO-1
$\#K14_{\text{live, tr}}^{\text{lo}}$	number of $K14^{\text{low}}$ live cells for model training
$\#K14_{\text{live, tr}}^{\text{hi}}$	number of $K14^{\text{high}}$ live cells for model training
$\#\text{dead}_{\text{tr}}$	number of dead cells for model training

$\rho_{hD}$	death gain, $K14^{high}$
$\rho_{lD}$	death gain, $K14^{low}$
$\rho_{h \rightarrow l}$	transition gain from $K14^{high}$ to $K14^{low}$
$\rho_{l \rightarrow h}$	transition gain from $K14^{low}$ to $K14^{high}$
$\rho_h$	cell division gain, $K14^{high}$
$\rho_l$	cell division gain, $K14^{low}$
$\#K14_{live, sim}^{lo}$	number of $K14^{low}$ live cells generated via dynamics simulation
$\#K14_{live, sim}^{hi}$	number of $K14^{high}$ live cells generated via dynamics simulation
$\#dead_{sim}$	number of dead cells generated via dynamics simulation

## II. Dynamical system

A linear time-invariant dynamical system was chosen to model cell-state interactions,  $x[k+1] = A \cdot x[k]$ , where state vector  $x = (\text{number of } K14^{high} \text{ live cells, number of } K14^{low} \text{ live cells, number of dead cells})^T \in \mathbb{R}^3$ ,  $[k, k+1)$  is a 12-hour interval, and dynamics matrix  $A \in \mathbb{R}^{3 \times 3}$  is parameterized as follows:\*

$$A = \begin{bmatrix} \rho_h - \rho_{h \rightarrow l} - \rho_{hD} & \rho_{l \rightarrow h} & 0 \\ \rho_{h \rightarrow l} & \rho_l - \rho_{l \rightarrow h} - \rho_{lD} & 0 \\ \rho_{hD} & \rho_{lD} & 1 \end{bmatrix}.$$

Values of the dynamics parameters were identified using training data computed from timecourse data in a manner specified by hypothesis (e.g.,  $K14^{high}$  Darwinian selection) and agent (Sec. III). Thus, there is a *unique* dynamics matrix for each (hypothesis, agent) pair. Propagating a given matrix  $N$  time steps forward from initial condition,  $x_0 \in \mathbb{R}^3$ , yields state

vector at time  $N$ ,  $\mathbf{x}[N] = \mathbf{A}^N \cdot \mathbf{x}_0$ . For each (hypothesis, agent) pair, quantities of  $K14^{\text{high}}$  live cells,  $K14^{\text{low}}$  live cells, and dead cells were generated over time in this way via the appropriate dynamics matrix.

### III. On training data and parameter constraints for model identification

Recall that dynamical models were generated from timecourse data to test if  $K14^{\text{high}}$  Darwinian selection or cell-state transition were the likely driver of Trametinib-induced differentiation-state enrichment. The tables below summarize training data computations and parameter constraints for such models under each hypothesis. The “mixture” hypothesis was included for completeness—to predict the effect of the conservative death distribution with switching permitted (Fig. 3-3, 3-4). Additional practical constraints (omitted below) were enforced, e.g., nonnegative gains<sup>200</sup>.

#### $K14^{\text{hi}}$ Darwinian selection hypothesis

Agent	Assumptions on cell-state death & transition	How to compute training data for model identification from timecourse observations	Parameter constraints
Trametinib	All death in $K14^{\text{low}}$ No switching	$\# \text{dead}_{\text{tr}} = f_{\text{obs}}^{\text{dead}} \cdot (\#K14_{\text{obs}}^{\text{lo}} + \#K14_{\text{obs}}^{\text{hi}})$ $\#K14_{\text{live, tr}}^{\text{lo}} = \#K14_{\text{obs}}^{\text{lo}} - \# \text{dead}$ $\#K14_{\text{live, tr}}^{\text{hi}} = \#K14_{\text{obs}}^{\text{hi}}$	$\rho_{\text{hD}} = 0$ $\rho_{\text{h} \rightarrow \text{l}} = \rho_{\text{l} \rightarrow \text{h}} = 0$ $\rho_{\text{h}} = \rho_{\text{l}}$
DMSO	Equal death $K14^{\text{high}}$ & $K14^{\text{low}}$ No switching	$\# \text{dead}_{\text{tr}} = f_{\text{obs}}^{\text{dead}} \cdot (\#K14_{\text{obs}}^{\text{lo}} + \#K14_{\text{obs}}^{\text{hi}})$ $\#K14_{\text{live, tr}}^{\text{lo}} = (1 - f_{\text{obs}}^{\text{dead}}) \cdot \#K14_{\text{obs}}^{\text{lo}}$ $\#K14_{\text{live, tr}}^{\text{hi}} = (1 - f_{\text{obs}}^{\text{dead}}) \cdot \#K14_{\text{obs}}^{\text{hi}}$	$\rho_{\text{hD}} = \rho_{\text{LD}}$ ; $\rho_{\text{h} \rightarrow \text{l}} = \rho_{\text{l} \rightarrow \text{h}} = 0$ $\rho_{\text{h}} = \rho_{\text{l}}$

#### Cell-state transition hypothesis

Agent	Assumptions on cell-state death & transition	How to compute training data for model identification from timecourse observations	Parameter constraints
Trametinib	Equal death K14 <sup>high</sup> & K14 <sup>low</sup> Yes switching	$\#dead_{tr} = I_{obs}^{dead} \cdot (\#K14_{obs}^{lo} + \#K14_{obs}^{hi})$ $\#K14_{live, tr}^{lo} = (1 - I_{obs}^{dead}) \cdot \#K14_{obs}^{lo}$ $\#K14_{live, tr}^{hi} = (1 - I_{obs}^{dead}) \cdot \#K14_{obs}^{hi}$	$\rho_h = \rho_l$
DMSO	Same as above	Same as above	Same as above

#### IV. How to compute simulated fold change

Our computational models provided *simulated* quantities of K14<sup>high</sup> live cells, K14<sup>low</sup> live cells, and dead cells. Image cytometry provided *measured* quantities of K14<sup>high</sup> cells (live & dead) and K14<sup>low</sup> cells (live & dead); phenotypes of dead cells were unobservable. Thus, the simulated values were processed further to quantify K14<sup>high</sup> cells (live & dead) and K14<sup>low</sup> cells (live & dead) for direct comparison with biology (Fig. 3-3h). These steps are detailed below.

Let agent  $i \in \{\text{Trametinib, DMSO}\}$  and phenotype  $p \in \{K14^{hi}, K14^{lo}\}$ . For each time  $k \in \{0, 12, \dots, 72\}$  hr, simulated fold change of phenotype  $p$  at time  $k$  is the ratio,

$\frac{[\text{fraction}_{sim}^p]_{\text{time } k, \text{ Trametinib}}}{[\text{fraction}_{sim}^p]_{\text{time } k, \text{ DMSO}}}$ , in which simulated phenotype  $p$  fraction is defined as:

$$[\text{fraction}_{sim}^{K14^{lo}}]_{\text{time } k, \text{ agent } i} = \left[ \frac{\#K14_{sim}^{lo}}{\#K14_{live, sim}^{hi} + \#K14_{live, sim}^{lo} + \#dead_{sim}} \right]_{\text{time } k, \text{ agent } i} \quad (1a)$$

$$[\text{fraction}_{sim}^{K14^{hi}}]_{\text{time } k, \text{ agent } i} = \left[ \frac{\#K14_{sim}^{hi}}{\#K14_{live, sim}^{hi} + \#K14_{live, sim}^{lo} + \#dead_{sim}} \right]_{\text{time } k, \text{ agent } i} \quad (1b)$$

The denominator of (1), cell population total, is obtained directly via dynamics simulation.

The numerator of (1) is the *in silico* quantity of phenotype  $p$  cells (live & dead) at time  $k$  after

initial treatment with agent  $i$ , which requires additional computation based on (hypothesis, agent) pair.

Under  $K14^{\text{high}}$  Darwinian selection hypothesis, death is allocated to the weaker cell state,  $K14^{\text{low}}$ , in entirety under Trametinib:

$$[ \#K14_{\text{sim}}^{\text{lo}} ]_{\text{time } k, \text{ Trametinib}} = [ \#K14_{\text{live, sim}}^{\text{lo}} + \#\text{dead}_{\text{sim}} ]_{\text{time } k, \text{ Trametinib}} \quad (2)$$

$$[ \#K14_{\text{sim}}^{\text{hi}} ]_{\text{time } k, \text{ Trametinib}} = [ \#K14_{\text{live, sim}}^{\text{hi}} ]_{\text{time } k, \text{ Trametinib}} \quad (3)$$

However, under the cell-state transition hypothesis, Trametinib-induced death is evenly distributed between cell states:

$$[ \#K14_{\text{sim}}^{\text{lo}} ]_{\text{time } k, \text{ Trametinib}} = \left[ \frac{\#K14_{\text{live, sim}}^{\text{lo}}}{1 - \text{fraction}_{\text{sim}}^{\text{dead}}} \right]_{\text{time } k, \text{ Trametinib}} \quad (4)$$

$$[ \#K14_{\text{sim}}^{\text{hi}} ]_{\text{time } k, \text{ Trametinib}} = \left[ \frac{\#K14_{\text{live, sim}}^{\text{hi}}}{1 - \text{fraction}_{\text{sim}}^{\text{dead}}} \right]_{\text{time } k, \text{ Trametinib}}, \quad (5)$$

such that simulated dead fraction at time  $k$  under agent  $i$  is:

$$[ \text{fraction}_{\text{sim}}^{\text{dead}} ]_{\text{time } k, \text{ agent } i} = \left[ \frac{\#\text{dead}_{\text{sim}}}{\#K14_{\text{live, sim}}^{\text{hi}} + \#K14_{\text{live, sim}}^{\text{lo}} + \#\text{dead}_{\text{sim}}} \right]_{\text{time } k, \text{ agent } i}. \quad (6)$$

For both hypotheses, because  $K14^{\text{high}}$  and  $K14^{\text{low}}$  should be similarly fit in absence of therapy, death is evenly distributed between cell states under DMSO. Replace Trametinib in (4) and (5) with DMSO, and the computation follows.